POLITECNICO
MILANO 1863

SCUOLA DI INGEGNERIA INDUSTRIALE
E DELL'INFORMAZIONE

Production of Novel Nanostructured Targets for High-Intensity Laser-Plasma Interaction Experiments

Tesi di Laurea Magistrale in
Nuclear Engineering - Ingegneria Nucleare

Author: **Maria Sole Galli De Magistris**

Student ID: 975077
Advisor: Prof. Matteo Passoni
Co-advisors: Alessandro Maffini, Davide Vavassori, Francesco Gatti
Academic Year: 2022-2023

Abstract

The study of high-intensity laser-plasma interaction is of great interest from an application-oriented point of view. Laser-driven ion sources and Inertial Confinement Fusion (ICF), are two examples of envisioned applications. In the former, thin solid targets can be irradiated by ultra-high intensity TW laser systems delivering mJ energies in fs pulses, which are interesting to realize compact accelerators. In the context of ICF, high-intensity lasers delivering tens of J energies in ns pulses are exploited to compress a capsule containing the fuel. Precise control and reproducibility of the interaction are necessary to guarantee their feasibility. To achieve these goals, great effort is dedicated to the optimization of the targets with which the laser interacts. The general aim of this thesis work was the production of nanostructured targets with tunable properties according to the laser parameters typical of laser-driven ion sources and ICF. Magnetron Sputtering (MS) and Pulsed Laser Deposition (PLD), have been exploited for this purpose. In the context of laser-driven ion sources, both Single Layer metallic foils and Double Layer Targets (DLTs) were considered. The second design consists of an additional porous thin layer ($< 8\ \mu m$), a PLD deposited carbon nanofoam, which, thanks to its internal structure enhances laser absorption. A procedure to realize free-standing metallic foils exploiting MS was developed. Thickness tunability down to the nm scale was achieved. The obtained films can either be exploited in a Single Layer or in a DLT concept. Thanks to their enhanced laser absorption efficiency, carbon foams may be also of interest in the context of ICF, as external layer of the capsule. Nevertheless, this is a widely unexplored topic. According to the few simulations available, the thickness of the carbon foam in ICF relevant conditions should be in the order of hundreds of μm. Pioneering PLD depositions of such a high thickness carbon foam were successfully conducted on different types of substrates, ranging from thin free-standing films up to bulk material, assessing the feasibility of realizing carbon foam targets for experiments in ICF conditions.

Keywords: Laser-plasma interaction, laser-driven ion sources, inertial confinement fusion, magnetron sputtering, pulsed laser deposition, nanostructured films

Abstract in lingua italiana

Lo studio dell'interazione tra laser ad alta intensità e un plasma è interessante per le sue possibili applicazioni. Due possibili esempi sono sorgenti di ioni da laser e fusione a confinamento inerziale (ICF). Nella prima, un sottile target solido può essere irraggiato con laser ultra intensi, caratterizzati da energie nell'ordine dei mJ e impulsi di fs, di interesse per realizzare acceleratori compatti. Nel secondo caso, laser ad alta intesità caratterizzati da energia dell'ordine dei J e impulsi di ns vengono usati per comprimere una capsula contente il combustibile. Affinchè tali applicazioni siano effettivamente realizzabili, è necessario poter controllare precisamente l'interazione. A questo fine sono stati studiati modi per ottimizzare i target. Lo scopo generale della tesi è stato quello di produrre materiali nanostrutturati con proprietà controllabili a seconda dei parametri laser per applicazioni nell'accelerazione di particelle e in ICF, sfruttando tecniche di Magnetron Sputtering (MS) e Pulsed Laser Deposition (PLD). Riguardo all'accelerazione, sono stati considerate due configurazioni di target, fogli metallici Single Layer e Double Layer Targets (DLTs) dove viene aggiunto un sottile ($< 8\ \mu m$) strato di materiale poroso nanostrutturato, foam di carbonio realizzata tramite PLD, capace di aumentare l'assorbimento dell'energia laser. E' stata sviluppata una procedura per realizzare film free-standing tramite MS che potessero essere usati sia come Single layer che come DLT, con spessore controllabile nell'ordine dei nm. Grazie alla loro efficienza di assorbimento dell'energia del laser, le foam di carbonio sono interessanti anche come strato esterno della capsula di combustibile in ICF. Questo è un argomento inesplorato sia sperimentalmente sia teoricamente. Le poche simulazioni disponibili hanno previsto spessori della foam dell'ordine di centinaia di um. In questa tesi foam di tali spessori sono state ottenute con successo tramite PLD, su vari substrati, dimostrando la possibilità di realizzare target di foam di carbonio per esperimenti in condizioni rilevanti per ICF.

Parole chiave: Laser-plasma, accelerazione da laser, fusione a confinamento inerziale, magnetron sputtering, pulsed laser deposition, film nanostrutturati

Contents

Introduction

Laser-plasma interaction is a field of study that has raised great interest in the scientific community. When a high-intensity laser interacts with a target material, this is rapidly ionized, generating a plasma. The continuous development of laser technology has allowed the exploration of various interaction regimes and phenomena that are relevant for fundamental research and possible applications. Laser beams delivering intensities of 10^{15} W/cm^2 in ns pulses are exploited in Inertial Confinement Fusion, one of the two approaches toward nuclear fusion energy production. At ultra-high intensities (i.e., $> 10^{18}$ W/cm^2), particle acceleration can be achieved. In particular, TW laser-driven ion sources may provide a more compact and cost-effective alternative to conventional accelerators in various fields, ranging from materials science to medicine. To guarantee the feasibility of these appealing applications of laser-plasma systems, precise and reliable control of the interaction, together with an increase in the process efficiency, is of fundamental importance. To achieve these goals, along with advances in laser technology, proper target design and engineering is necessary. Indeed, the target material's properties influence plasma characteristics and strongly impact the laser energy absorption efficiency. Therefore, a lot of effort has been devoted to the development of advanced targets.

Concerning laser-driven ion sources, one of the major challenges is to achieve highe energies, suitable for the envisioned applications, exploiting currently available laser technology while tailoring target properties. Among the various proposed solutions, two main strategies can be mentioned. One is based on the reduction of the thickness of Single Layer Targets thin typically employed in experiments, such as thin foils and films. The other relies on the development of Double Layer Targets (DLTs). In DLTs, the irradiated side of the thin film is covered with a low-density nanostructured material. This layer is capable of enhancing laser absorption, leading to higher energies of the accelerated ions. In this respect, Carbon nanofoams deposited via Pulsed Laser Deposition (PLD) have been successfully exploited.

In Inertial Confinement Fusion, the efficiency of the implosion process depends on several factors. It is strongly influenced by the energy absorption efficiency of the outer surface of the capsule, called the ablation layer. It is also known that the occurrence of hydrody-

namic and plasma instabilities has a detrimental effect. An active branch of research is devoted to the development of a suitable ablation layer. It has been demonstrated that plasma instabilities can be mitigated by employing mid-Z materials, while plastic foams (CH) increase laser energy absorption. Carbon nanofoams can potentially merge both positive aspects, being porous mid-Z materials.

The thesis work is devoted to the production of nanostructured targets with controlled and tunable properties for laser-driven ion sources and ICF. This is achieved through an interdisciplinary and synergistic approach, exploiting advanced deposition techniques, typical of materials science. In particular, Magnetron Sputtering is employed to realize thin metallic foils, while PLD is exploited for the production of carbon foams. The work is structured as briefly outlined below.

Chapter 1 provides a brief overview of aspects of laser-plasma interaction relevant to the understanding of the following work. The main laser technologies available nowadays are outlined. Then, the different laser absorption mechanisms in plasmas are presented, followed by an introductory discussion on laser-driven ion sources and ICF.

Chapter 2 is focused on the state of the art of targets for laser-plasma interaction experiments in the fields of laser-driven ion sources and ICF ablators, highlighting current open issues and challenges. This discussion naturally leads to the presentation of the objectives of the thesis work.

Chapter 3 is devoted to a description of the working principle of the deposition and characterization techniques exploited during the thesis work. Magnetron sputtering for thin film production, PLD for Carbon foam deposition, Scanning Electron Microscopy (SEM) for morphological characterization, and surface curvature methods for stress measurements.

Chapter 4 presents the deposition conditions of both metallic thin films and Carbon nanofoams, together with their morphological and mechanical characterization.

Chapter 5 is devoted to the development of a reliable strategy to obtain metallic free-standing film from sputtered-deposited samples, aiming at obtaining SL and DLTs. Therefore, preliminary foam depositions are also presented.

Chapter 6 addresses pioneering Carbon nanofoams target for experiments in ICF relevant conditions. Preliminary results of an experimental campaign are also reported.

Chapter 7 reports the conclusions of the thesis and, additionally, future perspectives and guidelines to further proceed with the work.

1 | High Intensity Laser-Plasma Interaction

In this Chapter, a brief theoretical background on laser-plasma interaction is provided. In Section 1.1 a very introductory overview on laser technology and its evolution is given. Section 1.2 is focused on the physics of laser-plasma interaction, starting from a general description of electromagnetic waves propagation in plasmas, moving then to consider the propagation of a high-intensity laser beam. The last two Sections are devoted to an overview on two relevant applications of laser-plasma interaction. Section 1.3 deals with laser-driven radiation sources, with a specific focus on ion acceleration via Target Normal Sheath Acceleration. Section 1.4 is focused on Inertial Confinement Fusion. These applications are the two general frameworks in which this thesis work is collocated.

1.1. Laser Technology

1.1.1. Working principle and properties of lasers

LASER is an acronym that stands for "Light Amplification by Stimulated Emission of Radiation". In the process of stimulated emission, an incident photon with energy $h\nu = E_2 - E_1$ promotes the de-excitation of an electron from the energy level E_2 to the level E_1 (being $E_2 > E_1$). As a consequence, another photon of energy $h\nu = E_2 - E_1$ is emitted. This photon adds in phase with the incoming one and propagates along the same direction [1], as represented in Figure 1.1a.

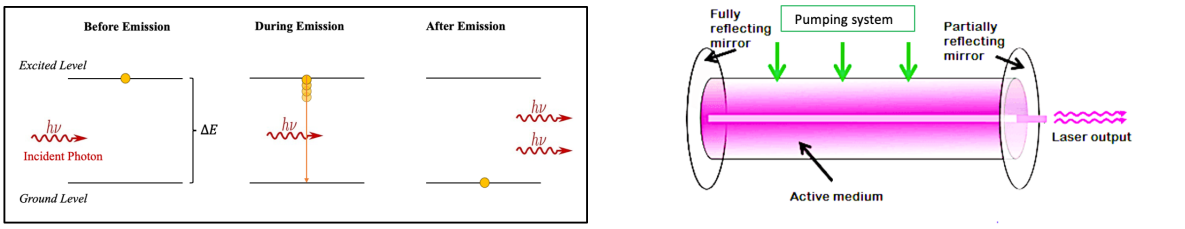

(a) (b)

Figure 1.1: Schematic representation of (a) the stimulated emission process and (b) of the laser working principle. Adapted from [2] and [3].

In order for stimulated emission to be more probable than absorption (in which the incoming photon is absorbed promoting the transition $E_1 \rightarrow E_2$), the level E_2 must be more populated than level E_1. According to Boltzmann statistics, this is not the case at thermal equilibrium, thus a population inversion must be produced in the material [1]. A schematic representation of a laser working principle is shown in Figure 1.1b. A pumping system provides energy to the active medium, which can be gaseous (He-Ne or CO_2), liquid (organic dyes) or solid (Nd:YAG, Ti:Sapphire or semiconductor diodes), producing the population inversion to enable stimulated emission to occur. The active medium is put between two highly reflective mirrors. In this way, bouncing back and forth, electromagnetic waves are amplified at each passage in the active medium. Specifically, one of the two mirrors is partially transparent to obtain a useful output beam.

Lasers have several interesting properties: directionality, spatial and temporal coherence, monochromaticity, short pulse duration and brightness [1]. Spatial coherence enables tight focusing, making lasers interesting for high-precision applications. Temporal coherence allows to obtain highly monochromatic waves or, alternatively, really short pulses. It is worth remembering that, indeed, the spectral range ($\Delta\nu$) and the time duration (τ) of a laser pulse are inversely proportional to one another $\Delta\nu \sim 1/\tau$. Brightness can be defined as the power emitted by a source (i.e., the laser) per unit surface per unit solid angle. Thanks to their directionality, lasers are characterized by large values of brightness which enable to reach really high focused intensities [1]. The instantaneous intensity can be defined as the energy that flows in the unit time through the unitary surface orthogonal to the propagation direction. Usually, the intensity mean value is considered, defined as the mean value of the instantaneous intensity over a period [4].

1.1.2. Short pulses and high intensities

Increasing the laser intensity, new regimes of interaction with matter, relativistic and non-linear effects can be explored (see Figure 1.2). This is of interest not only from the purely physical point of view but it might be relevant also for practical applications. Laser pulses can be modeled with a Gaussian-like profile both in time and space, thus the peak intensity I can be expressed as:

$$I = \frac{E_l}{\tau_l A_s} \tag{1.1}$$

where E_l is the laser energy, τ_l is the pulse duration, usually expressed as full width at half maximum (FWHM), and A_s is the area of the laser spot. It is evident that to reach higher intensities, one can increase the energy, reduce the spot size or reduce the pulse duration [2].

Two techniques have been developed to produce short pulses: Q-switch and mode-locking. Q-switch consists in temporarily switching the quality factor Q (a parameter representing the ratio between the energy stored and the energy lost in a resonant cavity) from low to high values and vice versa. In this way, all the energy accumulated in the high-Q phase is released in the low-Q phase as a high energy pulse (several J) with a short duration (in the order of ns)In mode-locking, the different modes present in the cavity are somehow constrained to oscillate with a definite relation between their phases, so that they constructively interfere producing a high energy short pulse (in the order of few ns or even tens of fs). To have the shortest possible pulses, materials with the largest bandwidth must be employed: with gaseous active media it is possible to go down to $0.1 - 1$ ns, while with liquids and solids, down to fs [1]. Thanks to Q-switch and mode-locking, intensities up to 10^{14} W/cm^2 have been reached. Further raising the intensity of short pulses would risk to damage both the optics and the active medium [4]. As a solution to this problem, the Chirped Pulsed Amplification has been developed [5]. The laser pulse is stretched in time so to decrease its intensity, but not its energy. Then it enters in the amplifier which is a gain medium in population inversion condition. There the laser energy is increased, still having a sufficiently low intensity to not cause any damage. Lastly, the pulse is compressed in time, back to its original duration [4]. This allows to reach powers in the order of hundreds of TWs or even PWs and intensities between 10^{14} $W/cm^2 - 10^{21}$ W/cm^2, depending on the amplification strategy.

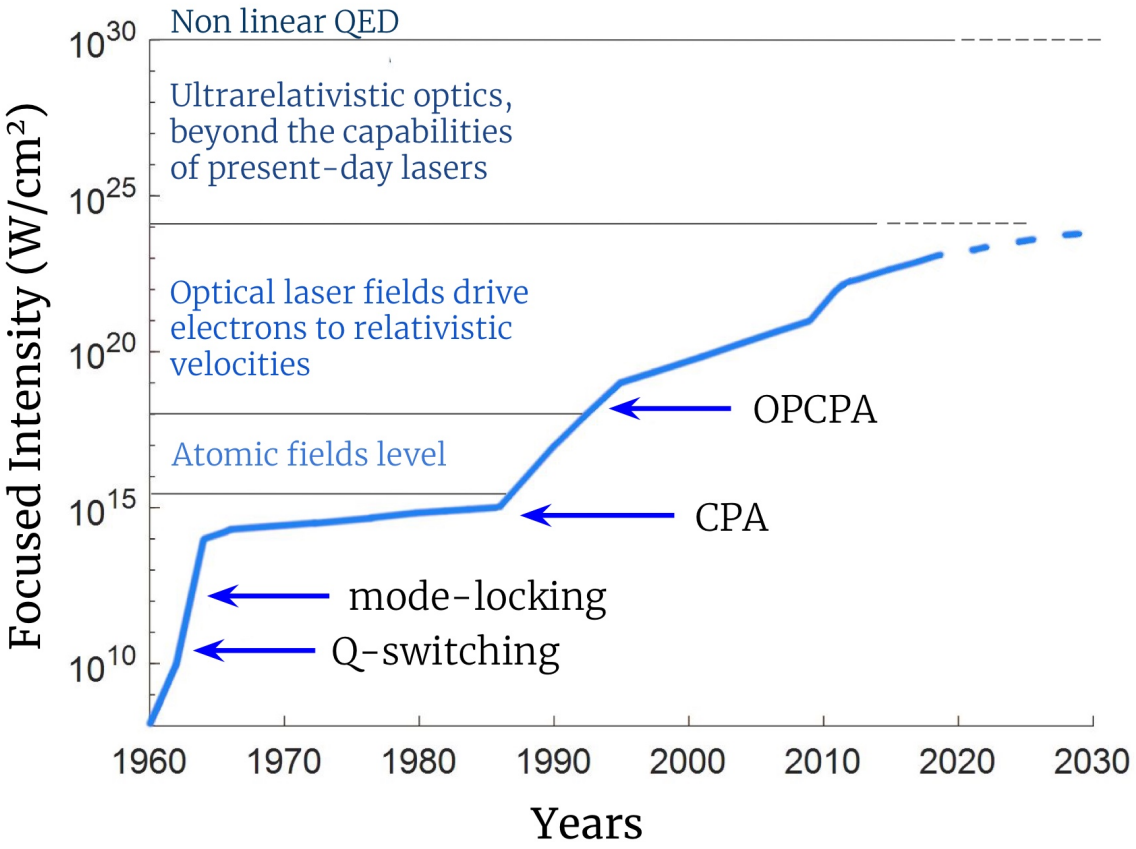

Figure 1.2: Increase of maximum laser intensity over the years according to advances in laser technology [6]

1.1.3. Different types of high-intensity lasers

It is possible to identify two different classes of high-intensity lasers: PW and TW class lasers. PW lasers can provide energies from tens of J up to a few hundreds of J in pulses of duration ranging from tens of fs and 1 ps. The repetition rate is generally in the order of 1 Hz or it can be limited to few shots per day. The operation of PW lasers requires extensive facilities. There are several of them spread worldwide. Some examples related to Europe are reported. Vega-3, located at the Center for Pulsed Lasers, University of Salamanca delivers 30 J, 1 PW at 1 Hz. Apollon at Orme de Merisiers, Saclay is planned to deliver 150 J, 10 PW at a rate of 1 shot per minute. ELI-Beamlines, Dolni Brezany, Czech Republic is provided with different beam lines, two of which are planned to operate at 1 PW, 20/30 J, 10 Hz, another one at 10 PW, 1.5 kJ, one shot per minute. Concerning TW lasers, they can deliver lower energies, from few mJ up to few J over pulses up to few hundreds of fs, at frequencies in the range 0.1 Hz–few kHz. Commercially available 200 TW lasers are sufficiently compact to fit in a room. Even

smaller sizes characterize table-top lasers, that can deliver powers up to few tens of TW. A further reduction in dimensions is foreseen to realize portable high-intensity lasers. Lasers can be classified according also according to other parameters, such as the pulse duration, which determines the energy delivered per pulse. Indeed, for example, there are TW lasers working with pulses in the order of ns, capable of delivering energies in the order of tens of J, and TW lasers working with fs pulses, capable of delivering energies in the order of J.

1.2. The physics of laser-plasma interaction

Since the ionization threshold of matter is around $10^{14} W/cm^2$, when a high-intensity laser impinges on it, a plasma is readily generated, drastically affecting further propagation of the pulse [4]. In the following, a brief theoretical overview of electromagnetic waves propagation in a plasma is given, based on some [4, 7–11] of the many available bibliographic references, moving then to a description of laser-plasma interaction.

1.2.1. Plasma fundamental parameters

A plasma is a macroscopic, overall neutral system made of different charged and neutral particle species, which are free to move over relatively large distances, thus generating electromagnetic fields through their charge and current densities. As a consequence, the behavior of a plasma is dominated by collective effects via the self-consistent electromagnetic forces rather than short-range Coulomb interactions. Due to this strong coupling between plasma and electromagnetic fields, it is evident that the interaction of the laser pulse with the plasma must be considered in a self-consistent way.

Before proceeding further with the description of electromagnetic wave propagation in plasmas, it might be useful to introduce two important parameters, related to the collective behavior of plasma particles: even though the system is overall neutral, local fluctuations of charge are allowed by the continuous balance between thermal motion and electromagnetic forces. The characteristic lengths and frequencies of such oscillations are described respectively by the *Debye length* and the *plasma frequency*, which can be defined for each population. In the simplest case, ions dynamics can be neglected due to their higher inertia and only electron Debye length (λ_p) and electron plasma frequency (ω_p) can be considered:

$$\omega_p = \sqrt{\frac{4\pi n_e e^2}{m_e}} \qquad \lambda_p = \sqrt{\frac{T_e}{4\pi n_e e^2}} \tag{1.2}$$

Where ne, me and T_e are, respectively, the electron number density, the electron mass and the electron temperature. The Debye length defines a sphere inside which short-range Coulomb interactions are dominant, while on length scales larger than λ_p only long-range electromagnetic interactions have to be considered.

1.2.2. Basic concepts of electromagnetic waves propagation in plasmas

An electromagnetic field is represented in a complete, exact, and relativistically correct manner by Maxwell's equations. On the contrary, the plasma, being a many-body system, has too many degrees of freedom to allow for an exact description so that, simplified models are employed. For example, one can adopt a non-relativistic, linear, collisionless cold fluid approximation to describe the dynamics of a neutral plasma, composed by only two populations: electrons and ions. By coupling Maxwell's equation with those of the aforementioned fluid model, one obtains the following dispersion relation for a transverse monochromatic EM wave (of wave vector $\mathbf{k}$ and frequency ω) in a homogeneous plasma:

$$\omega^2 = k^2c^2 + \omega_p^2 \tag{1.3}$$

ω_p represents a cut-off frequency for the propagation of the electromagnetic wave. Indeed, for $\omega < \omega_p$, $\mathbf{k}$ is imaginary and the wave, having a spatial dependence of the type $e^{i\boldsymbol{k}\cdot\boldsymbol{r}}$, is exponentially dumped. It is useful to introduce the *critical density* (n_c) as the electron density for which $\omega = \omega_p$:

$$n_c = \frac{m_e\omega_p^2}{4\pi e^2} \tag{1.4}$$

This simplified description allows to identify three different regimes (see Figure 1.3) :

- Under-dense $n_e < n_c$ ($\omega > \omega_p$): $\mathbf{k}$ is real and the electromagnetic wave can propagate;
- Over-dense $n_e > n_c$ ($\omega < \omega_p$): $\mathbf{k}$ is imaginary and the electromagnetic wave is exponentially dumped with a characteristic length called skin depth $L = \frac{c}{\sqrt{\omega_p^2-\omega^2}}$;
- Near-critical $n_e = n_c$ ($\omega = \omega_p$): this intermediate regime is characterized by a more complex behavior, which leads to an efficient coupling between EM wave and plasma.

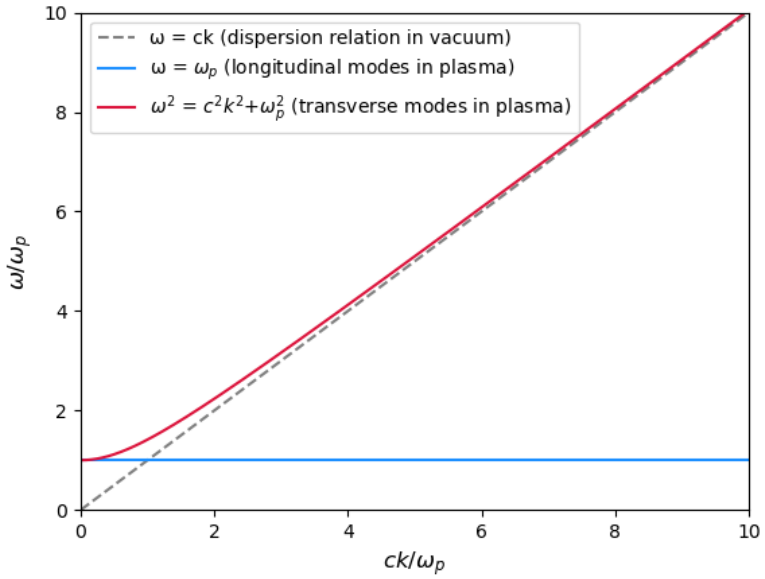

Figure 1.3: The dispersion relations of transverse and longitudinal EM waves in a plasma are represented, together with the reference one in vacuum.

When dealing with high-intensity lasers, some of the previous hypotheses should be removed.

If $I > 10^{18} W/cm^2$ relativistic effects become relevant in the dynamics of electrons and their mass must be corrected by the Lorentz factor ($\gamma = (1 - v_e^2/c^2)^{-1/2}$, being v_e the electron velocity and c the velocity of light). The so-called Akhiezer-Polovin [12] equations result from the combination of Maxwell's equation and the cold, collision-less, relativistic fluid model for the plasma. After appropriate assumptions and mathematical manipulations, it is possible to highlight that the effect of the relativistic change in the electron mass is to modify the plasma frequency as

$$\omega_{pr} = \frac{\omega_p}{\gamma^{1/2}} \tag{1.5}$$

This has two important consequences: since the Lorentz factor is always >1, the plasma frequency is decreased with respect to the non-relativistic case, allowing the propagation of the wave at higher values of density; this effect is called *relativistic self-induced transparency*. Additionally, the refractive index of the medium is modified, leading to a *self-focusing* of the laser pulse.

Moreover, the amplitude of a laser pulse is large and space dependent, thus non-linear effects must be considered, such as the ponderomotive force. It is an effective force that

describes the interaction of the laser pulse with the plasma charged particles when non-uniformities in the spatial profile of the electromagnetic field are taken into account:

$$\boldsymbol{F}_p = -\frac{n_e e^2}{4 m_e \omega^2} \nabla \boldsymbol{E}^2 = -\frac{n_e m_e c^2}{4} \nabla \boldsymbol{a}^2 \tag{1.6}$$

where $\boldsymbol{a}$ is the a-dimensional vector potential $\boldsymbol{a} = \frac{q\boldsymbol{A}}{m_e c^2}$, defined in terms of the vector potential $\mathbf{A}$ (being $\boldsymbol{E} = \frac{1}{c} \cdot \frac{\partial \boldsymbol{A}}{\partial t}$). If $\boldsymbol{a}^2 > 1$, relativistic effects must be considered, and the ponderomotive force can be re-written as $\boldsymbol{F}_p = -n_e c^2 \nabla \gamma$, being $\gamma = (1 + \boldsymbol{a}^2)^{1/2}$.

Two main features of this force must be highlighted: it always pushes particles towards regions of low intensity field ($\boldsymbol{F}_p \sim -\nabla \boldsymbol{E}^2$), independently of their sign ($\boldsymbol{F}_p \sim e^2$) and it is inversely proportional to the mass, so it is more effective on lighter particles, thus electrons. Indeed, the ponderomotive force is at the basis of laser-driven electron acceleration.

In the following, the main mechanism of high-intensity laser absorption in the under-dense, over-dense and near-critical regimes is briefly addressed. In all cases, electrons with relativistic energies, also called hot electrons, can be produced, though through different processes. These hot electrons are of fundamental importance for laser-driven radiation sources, as will be discussed in Chapter 1.3

1.2.3. High-intensity laser absorption mechanisms in plasmas

Laser interaction with an under-dense plasma.

The main mechanism of laser absorption in an under-dense plasma is the excitation of longitudinal plasma waves. Thanks to the action of the ponderomotive force, the propagating transverse electromagnetic wave of the laser pulse excites longitudinal plasma modes oscillating at a frequency ω_p. Essentially, the leading edge of the pulse pushes electrons forward, where the $\boldsymbol{E}^2$ is lower, leaving uncompensated positive charges behind. In this way, an electric field is generated and thus a restoring Coulomb force excites collective electron oscillation. Subsequently, when the laser pulse overtakes these electrons, they are pushed backward, enhancing the resorting force. Other mechanisms of laser absorption in an under-dense plasma are known as parametric instabilities. They arise as a consequence of the interaction of the laser pulse with electrostatic plasma waves and can be described by non-linear three-wave coupling [13]. Parametric instabilities are mainly affected by the laser intensity I, the density scale length $L_n = [(1/n)(dn/dx)]^{-1}$, and the electron temperature T_e. Additionally, they generally occur beyond a threshold value in the order of $I\lambda \sim 10^{15} \mu m^2$ (where λ is the laser wavelength). The main instabilities are

briefly described in the following.

- *Two plasmon decay* (TPD) is a process that happens for plasma density close to $n_c/4$ and consists in the decaying of the incident photon into two plasmons. The TPD linear growth rate can be expressed as [14]:

$$\hat{\gamma} = \frac{L_n I_{14}}{230 T_e} - 1 - \left(\frac{0.3 Z_{eff} L_n \sqrt{I_{14}}}{230 T_e^{5/2}}\right) \tag{1.7}$$

  where I_{14} is the laser intensity in units of $10^{14}\ W/cm^2$ and Z_{eff} is the effective atomic number expressed as $< Z^2 > / < Z >$. The first term represents the threshold for triggering TPD instability. The last term takes into account the collisional dumping of Langmuir Waves (i.e., plasmons).

- *Stimulated Raman Scattering* (SRS) occurs in plasma with a density lower than $n_c/4$ and consists in the inelastic scattering of the incident photon by an electron plasma wave. The threshold for SRS can be approximated by [14]:

$$I_{16} \approx 10(T_e/L_n^{4/3}) \tag{1.8}$$

  being I_{16} the laser intensity in units of $10^{16}\ W/cm^2$, evaluated at the quarter critical density.

- *Stimulated Brillouin Scattering* (SBS) can occur in the whole volume of an under-dense plasma and consists in the elastic backscattering of the incident photon by a phonon.

Parametric instabilities are relevant, for example, in the frame of inertial confinement fusion, due to their detrimental effects, as will be clarified in Section 1.4.

Laser interaction with an over-dense plasma.

In the over-dense regime, the laser pulse can't propagate and an evanescent wave is generated. Depending on the laser characteristics, different phenomena can occur, resulting in the production of high-energy electrons [15]. In the case of non-relativistic intensities ($10^{12} W/cm^2 < I < 10^{18} W/cm^2$), which are of interest for example in inertial confinement fusion (ICF), two mechanisms are allowed:

- *Inverse Bremsstrahlung* is a type of collisional absorption in which electrons gain energy absorbing radiation while interacting with the ions' electric field; this process is less effective with increasing energy [7, 8]. The Inverse Bremsstrahlung absorption coefficient (A_b) for a laser pulse of frequency ω propagating in an over-dense plasma

(characterized by a plasma frequency ω_p) is expressed as:

$$A_b = \nu_{ei} \frac{\omega^2}{\omega_p^3} \tag{1.9}$$

where ν_{ei} is the collision frequency between electrons and ions, and it is directly proportional to the atomic number Z [13].

- *Resonant absorption* is allowed when the Lorentz force, which drives electrons at the surface of the over-dense plasma, has an oscillating component directed along the density gradient (for example P polarized waves and oblique incidence are required in plane geometry); this component produces density perturbation leading to the excitation of resonant plasma electrostatic modes and consequent efficient energy absorption, accelerating electrons [8].

. In the relativistic regime ($I > 10^{18} W/cm^2$), which is typical of laser-driven ion acceleration experiments, two other effects are possible, once again depending on the laser polarization:

- *Vacuum heating*, also known as Brunel effect, is allowed for p-polarized waves and oblique incidence, in order to have a non-zero driving force related to the electric component of the Lorentz force. This is capable of extracting electrons at the solid-vacuum interface and accelerating them. After half an oscillation, such electrons re-enter in the plasma, where the electric field is evanescent, as hot electrons [15].
- *JxB heating* dominates in the case of s-polarization or normal incidence; electrons are accelerated in a similar fashion to vacuum heating, but the driving force is now the magnetic term of the Lorentz force [15].

As will be clarified in Section 1.3.2, hot electrons play a fundamental role in laser-driven ion sources, being able to transport the absorbed energy in the high-density regions where the laser can't propagate [15].

Laser interaction with a near-critical plasma.

In the near-critical regime, an optimal coupling between laser and plasma can be achieved, enabling to increase the efficiency in laser energy absorption and hot electron production, both in terms of temperature and number. Indeed, in the over-dense regime, laser absorption can occur only over the skin depth, which is larger for lower densities, while in the under-dense regime, the energy transfer is maximized for higher electron density. Thus approaching the critical density it is possible to enhance both volume absorption of the laser pulse and energy transfer to hot electrons.

1.3. Laser-driven radiation sources

Exploiting an external drive, such as a laser pulse, charge separation can take place in a plasma, generating intense electric fields capable of accelerating particles. In the following sections an overview on the possible laser-driven radiation sources is given, with a particular focus on ion acceleration and its applications.

1.3.1. Different types of radiation produced by laser-plasma interaction

Electron acceleration occurs upon the interaction of a high-intensity laser pulse with a gas target, from which an under-dense plasma is generated. As described in Section 1.2.3, a propagating laser pulse can excite longitudinal modes thanks to the action of the ponderomotive force. According to the *Laser Wakefield Acceleration* mechanism, first proposed by T. Tajima and J. M. Dawson [16], if the proper resonance condition ($T_l = T_p/2 \simeq \pi/\omega_p$) between the laser pulse period (T_l) and that of the longitudinal modes (T_p) is met, these oscillations can become resonant and large amplitude plasma waves, known as wakefields, are excited, oscillating with a phase velocity that is close to the laser group velocity [17]. Electrons can be accelerated up to high energies over short distances, in the order of MeV/mm, with a maximum energy given by $\epsilon = 2m_e c^2(\omega/\omega_p)^2$ (where ω is the frequency of the laser). In addition to laser wakefield acceleration, other mechanisms can take place, the description of which is out of the scope of this work and can be found in [17].

Ion acceleration can take place if a high-intensity laser impinges on a solid target. Again, different mechanisms have been investigated [15] (see Section 1.3.2), Target Normal Sheath Acceleration being the most relevant one.

These accelerated ions can be exploited to induce (ion,n) reactions in a target material to produce neutrons. One of the possible configurations of such laser-driven neutron sources is the so called "*pitcher-catcher configuration*": ions are produced upon the interaction of the laser with the first target material (*pitcher*) and accelerated toward the second target (*catcher*) to induce the nuclear reaction producing neutrons. The catcher is usually made of Li or Be (if the impinging ions are protons or deuterons) and its thickness must be equal to the range, in that material, of the most energetic ions [18].

Additionally, also photon sources can be obtained by exploiting the interaction of a laser with the target. Indeed, characteristics X-rays of the target material are always present. Moreover, electrons, accelerated either exploiting the interaction of the laser

with an under-dense or an over-dense plasma (through the mechanisms highlighted in Section 1.2.3), can be exploited to produce photons. Essentially, these hot-electrons are made to travel across a thick high-Z solid target, experiencing deceleration and emitting Bremsstrahlung radiation while interacting with the nuclei of the target material. The emitted photos can reach MeV energies [19–22].

1.3.2. Ion acceleration: laser interaction with targets

Depending both on laser and target parameters, different ion acceleration regimes can be identified, as shown in Figure 1.4. Since with currently available laser technology and solid targets, the dominant mechanism, as supported also by experimental results, is the Target Normal Sheath Acceleration (TNSA), a qualitative description of this mechanism is here provided. For the other ones, it is possible to refer to [15, 23, 24].

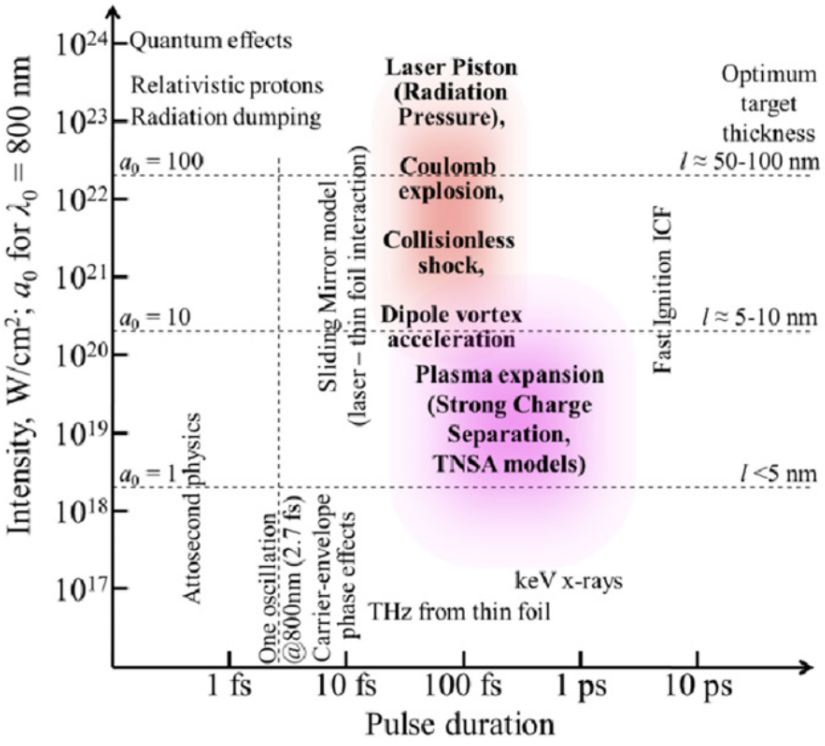

Figure 1.4: Representation of the possible regimes of ion acceleration according to pulse intensity and duration and optimal target thickness [23].

Target Normal Sheath Acceleration (TNSA)

A schematic representation of the TNSA process is provided in Figure 1.5. When a high-intensity laser (usually having $I > 10^{18}\ W/cm^2$) interacts with a solid target, an over-dense

plasma is formed and hot electrons can be generated, according to the mechanisms already highlighted in Section 1.2.3. If the thickness of the target is lower than the range of the electrons, they can travel through it and escape from the rear surface, leading to charge unbalance. The result is an intense electric field (in the order of 10^{10} V/cm) that extends for several Debye lengths from the back of the target, perpendicularly to it. This sheath electric field is capable of ionizing atoms and accelerates the resulting ions present on the rear surface [15, 23].

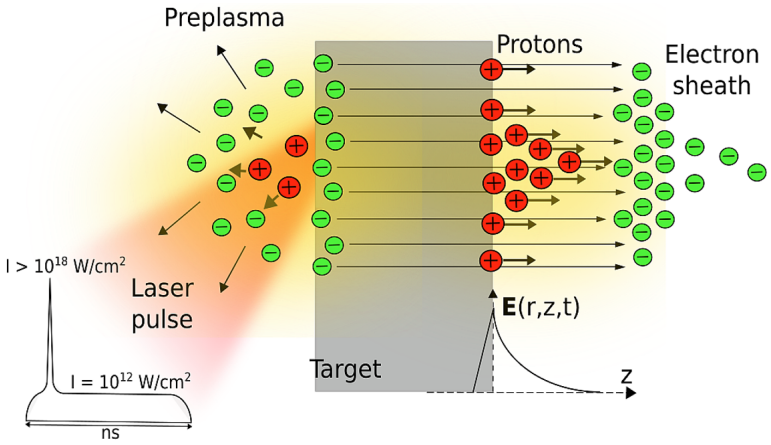

Figure 1.5: Schematic representation of TNSA [25].

The acceleration process is mostly effective on lighter ions, such as protons, which are generally present as impurities on the target. If protons are not enough to balance the electron negative charge, also heavier ions can be accelerated on longer time scales. Indeed, the accelerated protons will gradually shield the electric field and ions will be accelerated with lower energies, resulting in a spectrum characterized by an exponential decreasing trend and a well-defined cut-off maximum energy.

The magnitude of the electric field can be estimated by writing a balance between electrostatic and electrons thermal energies:

$$eE_s\lambda_d \sim T_e \tag{1.10}$$

being e the elementary charge, λ_d the Debye length, E_s the magnitude of the electric sheath field and T_e the electron temperature. At first approximation, it is possible to assume that the main accelerating force acting on electrons is the ponderomotive force.

Consequently, the electron temperature T_e results:

$$T_e \sim m_e c^2(\gamma - 1) \sim m_e c^2(\sqrt{1 + \frac{I\lambda^2[\mu m]}{10^{18}[W/cm^2]}} - 1) \tag{1.11}$$

being c the speed of light, γ the Lorentz factor, I the laser intensity and λ the laser wavelength. The quantity $I\lambda^2$ is called laser irradiance and is generally in the order of $10^{20}\ W/cm^2 \cdot \mu m^2$. Thus the electron temperature results in the order of MeV. Considering that the sheath field decays over distances in the order of μm, its magnitude is in the order of some $MV/\mu m$.

Properties and applications of laser-driven ion sources

Laser-accelerated ion beams show peculiar properties which make them attractive for several different applications, ranging from materials science to the medical field. Indeed laser-driven ion sources are characterized by good collimation since ions are accelerated along the electric field lines, perpendicularly to the target [15]. Half-opening angles are in the order of tens of degrees. An outstanding feature of laser-driven ion sources is the excellent beam quality. For example, a transverse emittance of $0.004\pi \cdot mm \cdot mrad$ has been reported, which is 100 times smaller than that associated with conventional accelerators [15]. Additionally, thanks to the intense electric sheath field, ions are accelerated up to MeV energies over short distances ($<\mu m$), while conventional accelerators work over meters. Therefore, more compact systems can be realized. Moreover, as previously outlined, ions are accompanied by the emission of electrons and characteristic X-rays. By employing a suitable target material, the accelerated protons can induce nuclear reactions to generate other kinds of radiation like neutrons and photons. Furthermore, the energy of the emitted particles can be tuned by working on the proper laser and target parameters. Therefore, laser-driven ion sources can provide greater flexibility with respect to conventional accelerators and are an appealing alternative to these.

To provide an example of a possible near-future application of laser-driven ion sources, Particle Induced X-Ray Emission (PIXE), can be mentioned [26]. It is a non-destructive characterization technique that exploits the interaction of MeV energy protons with the sample material. As a consequence of the interaction, characteristic X-rays of the irradiated material are emitted and detected, providing elemental information. Currently available tens of TW table-top lasers can accelerate ions up to suitable energies for PIXE.

A more challenging example is hadrontherapy [27]. This is a particular kind of radiation therapy, that exploits charged particles instead of conventional X-rays to treat tumors. The therapeutic energy window is in the range $60 - 250\ MeV$ for protons, while the

required currents are in the order of 10 nA. Therefore, it is evident that laser-driven ion sources are far from the therapeutic requirements, and improvements in energy, repetition rate, and reliability are needed.

These are just two of the many envisioned applications. Ion sources from laser acceleration may find a role also in the field of Inertial Confinement Fusion as beam ignitor in the Fast Ignition scheme (see Section 1.4.2) [15]. If used as neutron sources, laser-accelerated ions can be exploited also in Nuclear Activation Analysis (NAA) [28] or Boron Neutron Capture Therapy (BNCT) [15]. The former is a characterization technique based on the activation of the sample material upon interaction with neutrons. The latter is a radiotherapeutic technique to treat cancer. Additionally, laser-driven radiation sources could be exploited to perform Photon Activation Analysis (PAA), a nondestructive technique that exploits photons to perform elemental analysis [29]. Another possible application is the production of positrons for Positron Emission Tomography (PET). Generally, 20 MeV protons are exploited, energies that could be reached in the near future by exploiting moderate energies, ultra-short pulses, and high-repetition table-top lasers [15].

1.4. Inertial Confinement Fusion (ICF)

Inertial confinement fusion (ICF) is one of the two approaches, together with magnetic confinement (MCF), that are under investigation to obtain energy from controlled nuclear fusion reactions [30].

Among the various reactions of interest for nuclear fusion, the one involving Deuterium (D) and Tritium (T) is the most attractive, since it is characterized by the highest averaged reaction rate at lower plasma temperatures [13], as shown in figure 1.6.

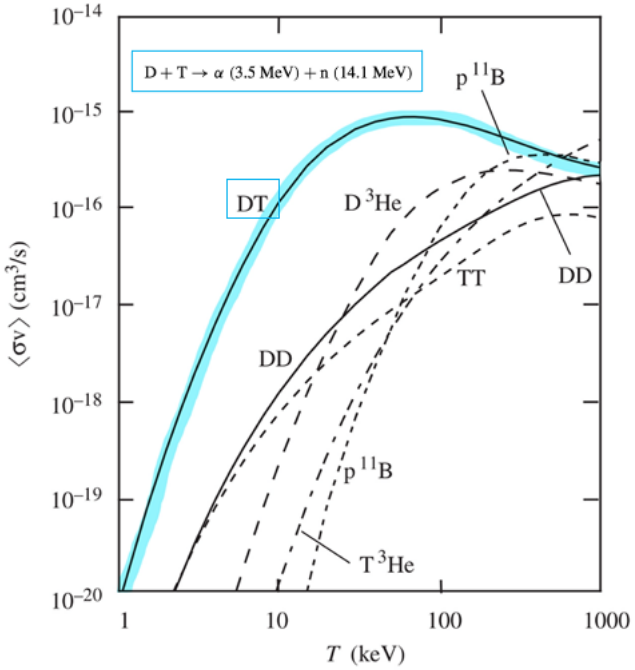

Figure 1.6: Maxwell-averaged fusion reactivities as a function of plasma temperature; the DT reaction is highlighted Adapted from [13].

1.4.1. The four stages of implosion

The basic idea of inertial confinement fusion is to exploit the energy of an external drive, for example a laser beam, to compress and heat the DT fuel, which is then maintained at fusion densities and pressures by its own inertia [31]. The entire process can be subdivided into four stages [4, 13], as depicted in Figure 1.7:

a. *Irradiation and Ablation*: the pellet (few mm in radius) containing the DT fuel (few mg) is irradiated symmetrically exploiting a laser beam, in a direct or indirect scheme (see Section 1.4.2) ; as a consequence, its outer surface is heated and ablated to generate a hot plasma which expands outwards.

b. *Implosion*: according to momentum conservation, the inner non ablated surface moves inward under the action of the ablation pressure leading to implosion and consequent compression of the fuel because of shock wave propagation.

c. *Stagnation and Central Ignition*: when the shock wave reaches the target center and is reflected back towards the converging shell, a deceleration phase begins and the imploding material stagnates in the center, converting its kinetic energy in thermal energy so that sufficiently high temperatures and pressures are reached in the central hot spot and the fusion reaction can ignite.

d. *Burn and Explosion*: alpha particles generated by the reaction slow down releasing their energy both into the hot spot, which self-heats, and into the surrounding compressed fuel, increasing its temperature and causing other fusion reactions to occur, leading to a propagating burn wave and the fuel rapidly expands outwards. [4, 13, 31]

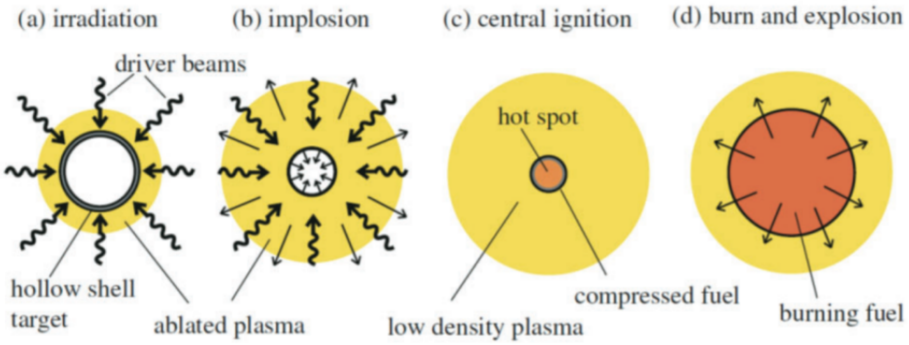

Figure 1.7: The four stages of implosion [4]

Typical parameters of the implosions are: compression of the capsule down to 100 μm, implosion velocity in the order of $3-4\cdot10^7 cm/s$, plasma temperature of 2-3 KeV (higher for ignition, around 10 KeV), ablation pressure in the order of 100 $Mbar$, hot spot densities of $10^{26} cm^{-3}$ (with a required ignition pressure of hundreds of $Gbar$), single-beam laser pulse intensity $\geq 10^{14} W/cm^2$ and pulse duration of few ns.

1.4.2. Direct, indirect and advanced schemes

Nowadays, the two main approaches to ICF are direct drive and indirect drive, shown in figure 1.8.

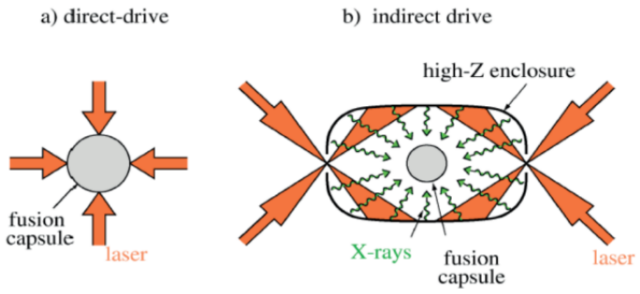

Figure 1.8: Schematic representation of direct (left) and indirect (right) schemes [4]

In the direct scheme, the target containing the DT fuel is directly irradiated by multiple

laser beams. In order for the implosion process to be effective, some requirements must be satisfied. First of all, efficient coupling between laser beam and target must be assured [4]. This is mostly related to the interaction between the laser and the coronal plasma generated in the ablation phase. Since the frequency of inverse bremsstrahlung (which is the main absorption mechanism in this case) is proportional to n_{cr}, by increasing this cut-off value it is possible to increase the absorption efficiency: for this reason, frequency-tripled lasers with submicrometric wavelength are usually employed [31]. Moreover, the beam intensity should be limited in order to reduce parametric instabilities [4]: in the case of SBS and SRS part of the laser energy is scattered and thus potentially lost, moreover SRS and TPD can produce hot electrons which may pre-heat the fuel, which is detrimental for the overall implosion efficiency [31]. Then, for an efficient exploitation of the energy transmitted to the fuel, the compression should be isentropic to minimize the invested energy [13] . A steep rise of the driver pressure to 100 MPa at the beginning of the pulse would launch a very strong shock, preheating the fuel and producing a large amount of entropy [31]. For this reason, a precisely time-shaped sequence of laser pulses is employed to achieve a strong, fast and almost adiabatic compression. Another critical issue is spherical symmetry: a deviation of the hot spot from its spherical symmetry would lead to an increase in both heat conduction losses and the fraction of escaping alpha-particles. Any kind of irradiation non-uniformity can lead to asymmetric implosions: long-wavelength non-uniformities are associated with the finite number of laser beams and with macroscopic defects of the target. Short-wavelength non-uniformities are associated with small amplitude surface defects and can grow exponentially due to Rayleigh-Taylor instabilities (RT). This is a kind of hydrodynamic instability that arises at the interface between two fluids when the denser one pushes the other. RT instability occurs firstly at the outer surface of the shell, due to the ablative pressure. It also develops at the shell's inner surface when it is slowed down by the expanding hot spot, at the end of implosion. RT instability tends to destroy the target and hinders the formation of the central hot spot, therefore its occurrence must be reduced[4, 13]. The RT growth rate is given by the following formula:

$$\gamma(k) = \alpha\sqrt{kg/(1+kL_n)} - \beta k V_a \tag{1.12}$$

being α and β coefficients depending on the ablation surface, L_n the density scale length, g the acceleration, k the wave number of the perturbation and V_a the ablation velocity. A good trade-off between fast implosions and hydrodynamic stability is a major objective. The use of multiple shocks has the additional benefit of reducing the shell non-uniformity growth factor associated with Rayleigh-Taylor instability. In direct drive, the energy coupled to the fuel is maximized since the target is directly irradiated. On the other

hand, it is characterized by a great drive non-uniformity, especially at small scales.

In the indirect scheme, the capsule containing the fuel is put at the center of a cavity called Holraum. The capsule is made of a high-density and high-Z material, like gold. When irradiated by the laser beams, the Holraum emits thermal (soft) X-rays (200 – 350 eV). The main advantages with respect to direct drive are symmetry of irradiation, stability, and smoothing of irregularities of laser the beam. Short-wavelength non-uniformities can be smoothened by the confinement of the X-rays in the cavity, while long-wavelength non-uniformities are hard to be smoothed out. The main disadvantages are the low conversion efficiency from laser to X-rays and energy losses.

Alternative approaches, known as advanced ignition schemes, have been developed aiming at separating compression and heating phases, exploiting external means to increase the DT temperature and trigger ignition: fast ignition employs energetic particle beams, shock ignition uses spherically convergent shocks, magneto-inertial fusion, relies on external magnetic fields.

1.5. Chapter summary

This Chapter was devoted to a basic description of the physics underlying laser-plasma interaction, focusing on two particular applications, laser-driven ion sources and ICF. It is worth highlighting the different laser parameters characterizing them. Generally, ion acceleration relies on ultra-high intensity TW lasers ($I > 10^{18}\ W/cm^2$) operating with pulses in the order of fs. Instead, ICF exploits PW lasers providing intensities in the order of $10^{15}\ W/cm^2$, over ns pulses. Targets play an important role during the interaction since their properties strongly affect the efficiency of laser energy absorption, consequently influencing the overall efficiency of the process considered. The next Chapter is dedicated to an overview on the State of the Art on targets for laser-driven ion sources and ICF. This discussion is propedeutic for the description of the objectives of the thesis work, focused on the production of advanced targets for experiments in these two fields.

2 | Advanced Targets for Laser-Plasma Interaction Experiments

This Chapter is devoted to the description of targets for laser-driven ion sources (Section 2.1) and for ICF (Section 2.2). In particular, different target designs for laser-driven ion sources are addressed, with a particular focus on Single Layer targets (Section 2.1.1) and Double Layer Targets (Section 2.1.3). Concerning ICF, the typical hollow-shell structure of the target is described in Section 2.2.1, highlighting the importance of the ablation layer. In Section 2.2.2 and 2.2.3 two possible solutions to enhance its performance are briefly discussed, namely the employment of mid-Z materials and plastic foams. These sections are propedeutic to understand the context and the objectives of the thesis work, which are presented in Section 2.3.

2.1. Targets for laser driven ion sources

As anticipated in the previous Chapter, laser-driven ion sources can be obtained by the interaction of a relativistic laser pulse (I>10^{18} W/cm^2) with a solid target. Despite their attractiveness, current laser-driven ion sources face limitations in meeting the requirements for certain applications. They should be relatively cheap, compact, stable and reliable, assuring shot-to-shot repeatability. Moreover, an increase in the available currents and energies of the accelerated ions is needed in some cases. The development of adequate laser technology and targetry is of fundamental importance to address these challenges [32]. TW laser systems are sufficiently compact to be used in universities, research centers and industry. They can provide high repetition rates (from Hz to kHz), consequently high currents and fluxes. Moreover, a further reduction of their dimensions is foreseen, enabling to realize portable ion-sources, which may find an application for example in the field of cultural heritage. A lot of effort has also been devoted to the investigation of different target design, mainly aiming at increasing the energy and number

of the accelerated ions. Some of the proposed concepts will be discussed in the following Sections 2.1.1- 2.1.3, with a particular focus on thin Single Layer solid targets (SL) and Carbon foam based Double Layer Targets (DLT), being them one of the main topics of this thesis work.

2.1.1. Single Layer targets

The most reliable and understood acceleration mechanism is TNSA. According to this model, the intensity of the accelerating electric field scales as $E = \sqrt{n_e T_e}$, where n_e is the electron density and T_e the electron temperature [22]. Thus, several strategies have been developed to increase these parameters by tailoring target properties.

The simplest target configuration consists in solid metallic or polymeric foils, with a thickness ranging from hundreds of nm up to hundreds of μm [15]. Target thickness is a parameter that can be exploited to tune the accelerated ions energy. For example, proton acceleration from the irradiation of Al thin solid targets have been investigated by Mackinnon et al. [33].In this experiment, the laser was characterized by 100 fs pulses and intensities exceeding 10^{20} W/cm^2, while the Al foils thickness ranged between 3 μm and μm. The experiment showed an increase in both temperature and cut-off energy in the ion spectra for decreasing film thickness. This is consistent with an increased electron density at the target rear side for thinner targets. Indeed, hot electrons are continuously reflected back and forth by the Debye sheath, at the target rear side, and by the $\mathbf{J}X\mathbf{B}$ force at the front of the target. If the transit double time for these energetic electrons is lower than the laser pulse duration, the electron density constituting the sheath field is enhanced by the electrons reflected at the front surface. Thinner targets are characterized by lower double transit time [33], which can explain the observations. Additionally, a higher variability in the cut-off energy of protons coming from the thinner foils was observed. This was attributed to small fluctuations in the laser prepulse, which for thin targets may have a detrimental effect, generating a preformed plasma which reduces the accelerating field [33]. Indeed, as shown in Figure 2.1, there is an optimal thickness value, depending on the laser parameters, together with a strong dependence on laser prepulse and contrast (i.e., the ration between the main pulse intensity and the prepulse intensity) [15].

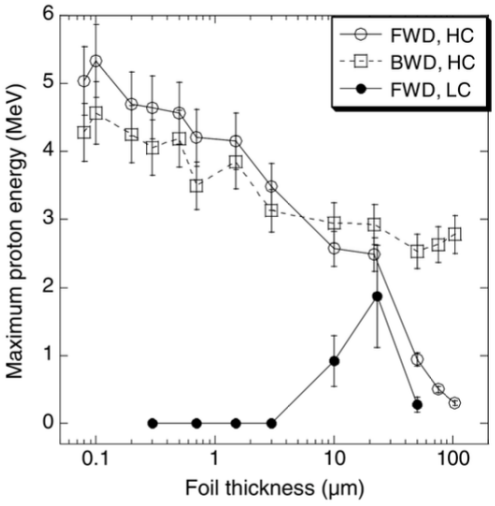

Figure 2.1: Variation of the maximum proton energy as a function of Al film thickness for different laser intensities and contrasts. HC is the case of high contrast 10^{10} with an intensity of $5 \cdot 10^{18}$ W/cm^2, LC is the case of low contrast 10^6 with an intensity of 10^{19} W/cm^2. Data for protons detected both in the forward direction (FWD) and in the backward direction (BWD) are reported [15].

Moreover, it should be noted that TNSA is dominant for target thicknesses ranging between hundreds of nm up to tens of μm, while for thinner films ($10-100$ nm) other mechanisms such as Light Sail Radiation Pressure Acceleration might be more relevant [15]. In this process, the momentum carried by the electromagnetic wave is transferred to the non-transparent medium, generating a radiation pressure. This radiation pressure acts on the electrons at the surface of the over-dense plasma, pushing them inward and causing a deformation of the plasma surface allowing the pulse to penetrate deeply into the target. Charge separation occurs, and a backholding electric field is generated accelerating ions. Since the target is thin enough, all the ions are accelerated before the end of the pulse so that part of it can further accelerate ions to higher energies [15]. In this case, high contrasts ($> 10^{10}$) are needed to avoid early disruption of the target by the prepulse.

2.1.2. Overview of advanced engineered solid targets

More advanced engineered targets have been proposed, based on proper designs to increase the efficiency in laser absorption and/or conversion into hot electrons. Some concepts are briefly reported below.

Modulated surface targets with known roughness of the irradiated surface, rely on multiple reflections of the laser beam and incidence under randomized angles to improve the laser

absorption efficiency. It has been demonstrated that up to 70% of the incident laser energy can be absorbed by targets having a roughness higher than 20%, almost independently from the incidence angle [34].

Grating targets exploit a periodic modulation of the front surface to trigger a resonant coupling between laser pulse and surface waves. High contrasts ($\sim 10^{12}$) are needed to avoid early disruption of these features by the prepulse. Grating targets realized by heat embossing of Mylar foils resulted in a maximum increase of a factor 2.5 in the cut off energy of protons with respect to plane targets [35].

Mass-limited targets are characterized by limited transverse dimensions, down to tens of μm. As a consequence, electrons at the surface can be reflected by the target edges back into the plasma. A hotter and denser plasma can be sustained for longer times, leading to an improvement in the proton energy [36].

Double Layer Targets consist in a solid thin foil covered with a low-Z nanostructured material to increase laser absorption. Some examples of Double Layer Targets are:

- *Nanosphere Targets*: the irradiated surface of a thin plastic foil is covered by a monolayer of polystyrene spheres, having dimensions comparable to the laser wavelength. This enables to increase both the maximum energy and the total number of the accelerated protons [37].
- *Nanowire targets*: the irradaited surface of the target is covered by carbon nanotubes. For example, exploiting thin diamond like carbon (DLC) foils covered with a carbon nanotube foam (CNF), the maximum proton energy increased by a factor 1.5 and the with respect to the uncoated DLC [38].
- *Carbon foam based Double Layer Targets (DLT)*: in this case a thin metallic foil is covered with a carbon foam deposited via Pulsed Laser Deposition. This type of targets will be described in more detail in the next section.

Most of the aforementioned targets are not suitable for high repetition rates [39] and have stringent requirements on laser parameters. However, Double Layer Targets (DLT) have the potential to operate at high repetition rates and exhibit greater flexibility in terms of laser parameters.

2.1.3. Carbon foam based Double Layer Targets (DLTs)

Carbon foams as near-critical layer

The idea behind DLTs is to exploit a layer of near-critical density to allow a better cou-

pling between the laser and the target, allowing for a volumetric energy absorption. The majority of lasers employed for ion acceleration operate within the infrared spectrum, such as 800 nm for Ti:Sapphire and 1600 nm for Nd:Glass lasers [18]. At these wavelengths, the critical density is approximately 10^{21} $electrons/cm^3$ [18]. For various materials, this corresponds to a mass density in the range $5 - 10$ mg/cm^3, notably lower than the solid density, by two or three orders of magnitude [18, 40]. Nanostructured materials having a large fraction of voids ($> 99\%$) represent a valuable choice as near-critical layers [18]. Among them, there are Carbon nanofoams , which can be directly deposited on the solid foil via Pulsed Laser Depositon (PLD) [18, 40–43].

PLD carbon nanofoams are a specific type of foam where nanoclusters assemble in a fractal-like manner into larger structures [42]. The result is a material exhibiting complex density profiles and spatial nonuniformities [18] at the nm and μm scales with void areas alternating to regions where the density approaches that of the solid [40, 42, 43].

A conceptual basic configuration and a cross-sectional view of a DLT are represented in the following Figure 2.2:

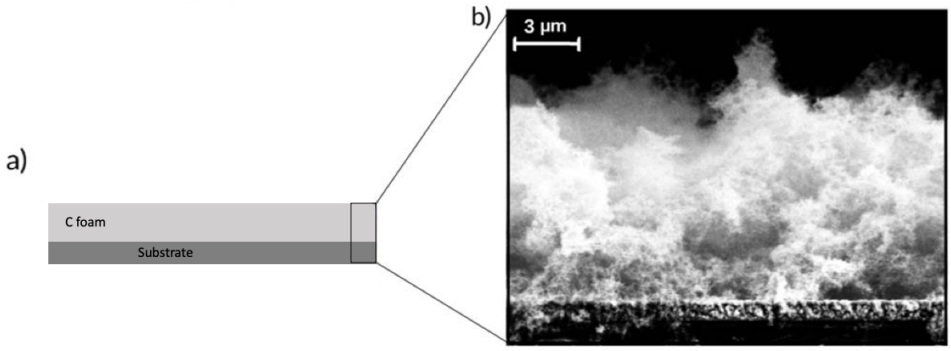

Figure 2.2: a) Conceptual representation of the DLT configuration. b) SEM image of a DLT (adapted from [18]).

Laser-DLT interaction

The characteristics of laser-DLT interaction have been investigated in several experimental and simulation campaigns to asses the role of the nanostructured material in the TNSA process [18, 39, 40, 44, 45]. DLTs have revealed several advantages over conventional solid layer targets (SL) [18, 40, 44]. Clear evidence of an enhanced TNSA process has been demonstrated. Indeed, the obtained spectra exhibit the distinctive signature of TNSA [18, 39], yet with notable improvements in the cut-off energy and number of accelerated ions compared to those achieved using SL. [18, 22, 44]. For example, a 2-fold increase

in the proton cut-off energy (18.5 MeV for DLT against 9.5 MeV for SL) and a 4-fold increase in protons having an energy higher than 4.7 MeV ($4 \cdot 10^9$ $protons/shot$ against $1 \cdot 10^9$ $protons/shot$) have been reported [22]. In this experiment, DLTs constituted by a 1.5 μm Al foil covered with a 4 μm slightly overcritical (3.3 n_c) foam were irradiated with a 30 fs laser pulse in the relativistic regime ($I = 10^{20}$ W/cm^2). Additionally, unlike SL, the maximum achievable energy is unaffected by laser polarization [18, 40]. Critical density and foam thickness should be properly tailored according to the laser parameters. In particular, there exists a optimal thickness, generally below 8 μm [46]. Examples of proton energy spectra and maximum proton energy for different thicknesses are reported in Figure 2.3

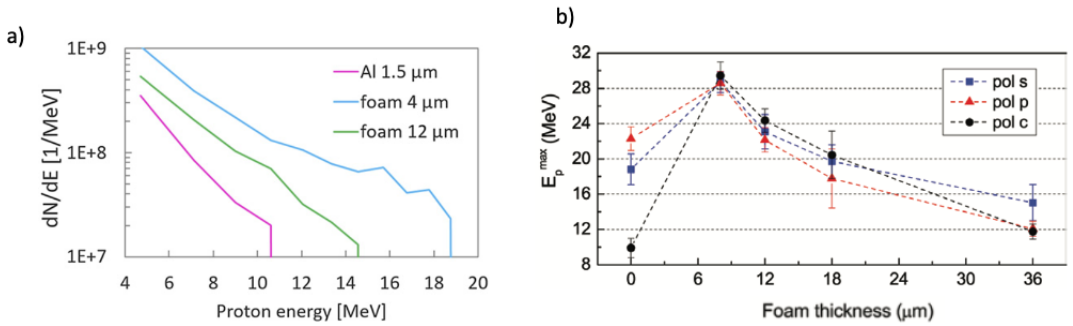

Figure 2.3: a) Single-shot proton spectra for different foam thicknesses [22]. b) Maximum proton energy as a function of foam thickness for s-, p- and c-polarization [40].

These experimental observations can be explained as follows. At relativistic intensities, the foam is completely ionized, leading to a near-critical plasma. Actually, using a high-contrast laser, the larger structures of the foam can survive long enough to significantly influence the interaction between the laser and the foam, as shown in Figure 2.4. Indeed, the resulting plasma shows density non-uniformities at the microscale which are of crucial importance in increasing the energy absorption both from electrons and ions [18, 22, 39, 40].

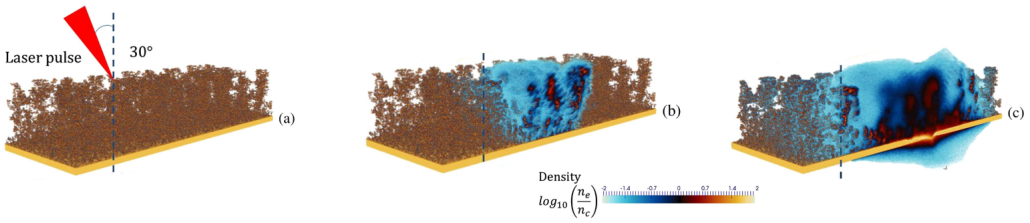

Figure 2.4: Simulation of the electron-density dynamics in the interaction of a laser pulse with the DLT at (a) 0 fs (beginning of the interaction), (b) 67 fs (during the interaction), (c) 134 fs (after the interaction is concluded) (Adapted from [39]).

Practically, the porous structure facilitates volumetric interactions [40], as the laser can propagate within the voids. The laser energy is efficiently absorbed by the near-critical surfaces, which are randomly distributed around the solid-density aggregates. Consequently, the interaction occurs at different angles of incidence and over a larger specific surface area, thereby optimizing the conversion of laser energy into hot electrons, independently from the laser polarization [22]. Nevertheless, it should be noted that these hot electrons must reach the target rear surface to contribute to the sheath field. If the foam is too thick, their transport efficiency is reduced [22]. In the case of a nanostructured material, also ions can absorb a significant portion of the laser energy. This happens as a consequence of the Coulomb-like explosion of the nanoparticles, a process which is absent in a homogeneous plasma [18].

Remarkably, DLTs irradiated with lasers at moderate intensities ($10^{16} - 10^{17} W/cm^2$) have successfully accelerated ions up to MeV energies, something unattainable with SL [44]. In this case only partial ionization of the foam occurs, generating an under-dense plasma through which the laser can propagate even in the non-relativistic regime [44].

These experimental and theoretical results indicate the robustness and versatility of DLTs compared to conventional SL, emphasizing their potential for laser-driven acceleration.

2.2. Targets for ICF

In the context of ICF, in addition to working on the laser parameters and irradiation strategies, a proper target design and engineering is of fundamental importance to optimize the implosion process. In the following Sections 2.2.1-2.2.3, the general structure of an ICF target is presented, followed by the state of the art approaches to improve its performances in the direct drive scheme.

2.2.1. The hollow-shell structure

An ICF target is generally a spherical hollow-shell, which can be compressed isentropically in an easier way and with a lower driver pressure with respect to a full sphere, guaranteeing the same implosion velocity [13]. As depicted in Figure 2.5, three different portions can be identified:

- an external layer (with a thickness of 3-60 μm), called ablator, which absorbs the laser energy making it available to promote the fusion reaction. Generally it is made of low-Z materials, such as plastics (CH);
- an internal layer with a thickness of 100 μm containing most of the fuel. The fuel is in the form of solid cryogenic DT , to minimize its entropy, which scales as $\sim p_0/\rho_0^{5/3}$ (being p_0 the pressure driving the shock wave and ρ_0 the fuel density);
- a central gaseous DT sphere, with a radius around 0.5-1 mm. Having a lower density, the entropy generated by the propagating shocks is higher, so that at the stagnation stage higher temperatures can be reached in the high-entropy gas with respect to the surrounding low-entropy DT, forming the hot spot [13].

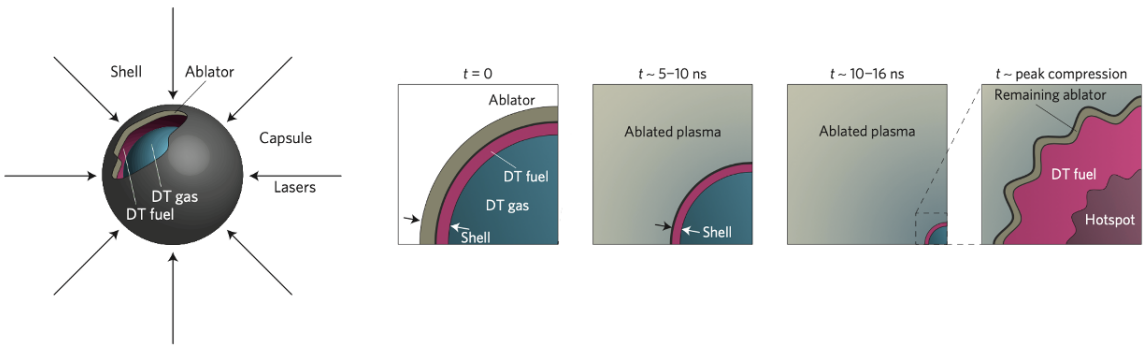

Figure 2.5: Schematic view of a typical ICF target and its evolution during the four stages of implosion [47].

The ablation layer is a crucial component of the ICF target, being responsible for laser absorption and fuel compression. An active branch of research in the field of ICF is devoted to the development of suitable ablation materials. The primary objective is to enhance the efficiency of converting laser energy into kinetic energy of implosion. To accomplish this, a compromise between laser absorption, hydrodynamic efficiency and radiation preheat must be achieved [48]. Mid-Z materials [48] and plastic foams [49–52] have been addressed in recent works.

2.2.2. Mid-Z materials for the ablation layer in direct-drive ICF

As outlined in Chapter 1, parametric instabilities such as TPD and SRS, and hydrodynamic instabilities, such as RT, have detrimental effects on the capsule implosion [14, 48, 53–55]. A mid-Z material, High Density Carbon (HDC), was successfully employed as ablator layer in the indirect-scheme [56]. Nevertheless, Mid-Z materials are attractive ablators also for the direct-drive scheme since they have proven in several experiments and simulations to be able to mitigate TPD, while maintaining an high hydrodynamic efficiency [14, 48], eventually reducing also RT [57]. A qualitative explanation of this behavior can be provided referring to Equations 1.9, 1.7 and 1.8.

Mid-Z materials offer improved laser energy absorption compared to CH by enhancing inverse Bremsstrahlung due to their higher atomic number (see Equation 1.9). As a result, the temperature T_e in the coronal plasma is correspondingly increased [14, 48]. Additionally, the density scale length L_n decreases because of the slower expansion of the heavier fluid [14]. Another advantage of using mid-Z materials as ablation layers is the formation of the Double Ablation Front (DAF) structure [14, 57]. In the case of low-Z plastic ablators, the incident laser energy is absorbed in regions where the plasma density is critical, leading to the generation of electrons. These electrons then transfer their energy to the ablation layer, heating it and driving the Electron Conduction Ablation front (EA). However, when mid-Z materials are irradiated, a second Radiative Ablation front (RA) emerges ahead of the EA. This occurs because mid-Z materials emit intense radiation that directly deposit its energy into the ablation material. It has been shown that such a structure is responsible for an increase in the ablation velocity V_a [57].

Thanks to lower L_n and higher T_e, mid-Z materials can increase the intensity threshold of TPD and enhance the collisional dumping of Langmuir Waves (refer to Equation 1.7), thus efficiently mitigating TPD. To make some examples, it has been demonstrated that SiO_2, HDC (High Density Carbon), silicon-, germanium- and chlorine-doped plastics show a reduced TPD with respect to CH abaltors. A similar discussion is valid for SRS, referring to Equation 1.8.

Concerning RT, the lower L_n increases its growth rate while higher V_a tends to reduce it. Some experiments showed that bromine- [57], silicon- and germanium-doped plastics [58] can reduce the RT growth rate. On the other hand, it should be noticed that the ablation pressure and mass ablation rate are increasing functions of A/Z, being A the mass number. Thus, low-Z materials, such as Be, are more promising to enhance the hydrodynamic efficiency [59, 60].

In a recent work [48] dedicated to indirect-drive, a solution to exploit the benefits of both

mid-Z and low-Z materials have been implemented by strategically layering the ablator. A multilayered target introducing Si and Be has been realized as shown in Figure 2.6. The outer mid-Z Si layer reduces TPD instability, while the inner Be layer is responsible for the higher hydrodynamic efficiency [48].

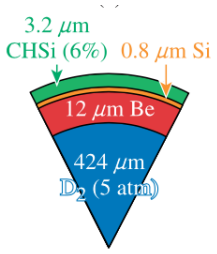

Figure 2.6: Cross-section of a multilayerd ICF target [48].

2.2.3. Plastic foams for the ablation layer in direct-drive ICF

In the field of direct-drive ICF, porous low-density structures of light chemical elements have been proposed as external layer of the target [49, 51, 52]. Indeed, different studies have demonstrated their capability of increasing laser absorption [49, 52], smoothing irregularities in the absorbed laser energy distribution [49, 50], increasing the ablation loading on the target surface [49, 51] and inhibiting hydrodynamic instabilities [52]. These interesting properties arise from their internal structure [49–52], in a similar fashion to what was explained previously.

In these types of experiments, foams of polymeric materials, like plastics ($[CH]_n$,$[CH_2]_n$), have been investigated. They can be produced with different structures, pore size and density exploiting various processing methods [49]. The resulting material has a structure characterized by a mixture of solid filaments and membranes with a thickness ranging from few μm to few hundreds of μm, a pore size varying from few μm to few tens of μm and an average density ranging from few mg/cm^3 to several hundreds of mg/cm^3.

The laser can propagate through the porous structure of the foam up to a distance called transparency length (L_0):

$$L_0 \simeq C(\frac{\rho_s}{\rho_a})^{1/5}\delta_0 \tag{2.1}$$

being C a constant dependent on the shape of the solid elements, ρ_s their density, ρ_a the average density of the foam (which can be either under-critical or over-critical) and δ_0 the pore size [52]. The solid elements evaporate under laser irradiation, generating a plasma which gradually fills the pores until an homogeneous plasma is developed [49–52]. The homogenization process can be divided in two stages [61]:

- laser absorption in the foam and implosion of the heated solid elements inside the pores; this process lasts tens/hundreds of ps;
- a slower process which leads to complete homogenization in few ns

. Thus, the homogenisation process has a duration of few ns, when lasers with intensity higher than 10^{13} W/cm^2 and large-pore materials (δ_0 around $10\mu m$) are considered. [49, 50]. Consequently, the porous structure survives long enough to effectively influence the laser-foam interaction. In particular, most of the laser light is absorbed in the partly homogenized plasma [61]. This inhomogeneous plasma with stochastically varying density allows volumetric absorption of the laser energy even in an over-critical foam. This is the reason behind the higher absorption efficiency in a plasma of a porous target compared to a plasma of a solid material. An increase up to 90% in the absorption efficiency of the first harmonic of a ns Nd laser have been experimentally observed [49, 51, 52]. Additionally, an experiment [51] has demonstrated that a polystyrene foam with large pores reflects a smaller fraction of light with respect to its solid counterpart. The time-resolved signal of the reflected light from the foam shows different features with respect to the signal coming from the solid target, proving that the porous structure manifests itself during the interaction [51]. The porous structure also influences the energy transfer in the laser-produced plasma, which is limited by the inhibited hydrodynamic filling of the pores and lack of free electrons during the homogenization time. These have been shown to increase the efficiency of conversion of the laser energy into compression of the target [49, 62], being the foam layer either under- [62] or over-critical [49]. Aiming at exploiting porous materials as absorbers in ICF targets, the interest is mainly for over-critical foams. Indeed, the density of the laser-produced plasma during the homogeneoization time increases with increasing density of the absorber. Additionally, the energy transfer from the hot plasma with density ρ to shock wave propagating in the cold solid with density ρ_s scales as $(\rho/\rho_s)^{1/2}$.

2.3. Context and Objectives of the thesis work

Conceptually, target fabrication is a complex process which goes through several steps, as schematically shown in Figure 2.7. As emerged in these two first introductory Chapters, the properties of the targets have a strong impact on laser-matter interaction.

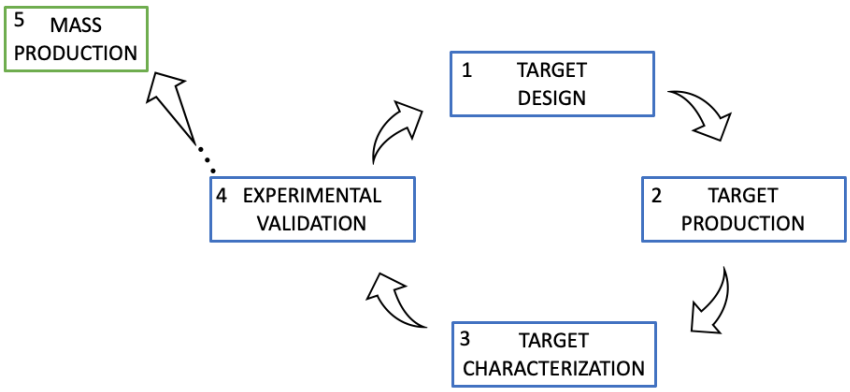

Figure 2.7: Diagram representing the different steps in target fabrication.

The design of a suitable and technically feasible target requires to consider various aspects. These include the existing theoretical and practical knowledge regarding the specific application or laser-matter interaction being studied, the available production techniques, the experimental conditions and setup (e.g. laser parameters, repetition rate, employed diagnostics ...). The characterization of the target plays a fundamental role as the experimental results strongly depend on its properties, including thickness, density, morphology and geometry. Therefore, it is crucial to conduct a comprehensive analysis of different properties for each sample, correlating them with the experimental results and evaluating the reproducibility of both. Moreover, experiments are necessary to evaluate the performances of the target and optimize its properties. In the pursuit of possible applications, mass production of the targets will become essential, necessitating scalability at an industrial level, together with the implementation of automatized production, characterization and assembly systems.

The thesis work is devoted to the production of nanostructured targets with controlled and tunable properties for laser-driven ion sources and ICF. This is achieved through an interdisciplinary and synergistic approach, exploiting advanced deposition techniques, typical of materials science.

Production of SL and DLT for laser-driven ion acceleration experiments

Several challenging aspects must be considered when designing a target for laser-driven ion sources. For example, as previously discussed, being able to tailor the target thickness is important improve the acceleration process. Moreover, as already mentioned, high repetition rates are required for their applications. Therefore, a fast and precise alignment of the target is needed. As an example, for a repetition rate of 1 Hz, samples must be

correctly positioned in 100 ms with micrometric precision. To accommodate this demand, relatively large foils are typically employed, enabling multiple shots to be conducted at different positions. Each irradiated point represents a target. Additionally, the use of high-intensity lasers leads to the generation of debris and shock waves during the interaction. The vaporized material can contaminate the neighboring targets and the optical diagnostics. Moreover, the propagation of the shock wave can damage the non-irradiated targets.

A typical target configuration is the *free standing film on perforated holder*. The thin foil is clamped between the two perforated masks constituting the holder (see Figure 2.8). Once they are clamped, free-standing films are obtained in correspondence of the holes. A film is considered "free-standing" when it is not in contact with a support. This target configuration enables for high repetition rates and partially reduces target damaging thanks the upper protective mask.

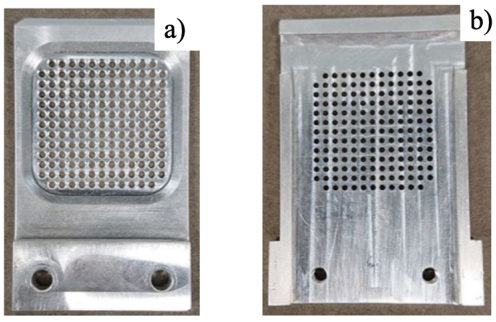

Figure 2.8: Picture of a) outer side of the front mask and b) inner side of the back mask of a perforated holder.

Usually, laminated foils are employed as thin films, both for SL and DLT. They are commercially available but present some limitations. From the manufacturing point of view, they are produced in a limited number of materials and thicknesses, ranging from hundreds of nm up to several μm [18]. Moreover, the sub-micrometric ones are characterized by an uncertainty on the thickness of the 30% with respect to the nominal value. Additionally, since these foils are manually fixed to the holder, their breakage or the formation of wrinkles and ripples can take place. All these aspects might undermine the shot-to-shot reproducibility, thus representing an obstacle for the realization of targets that can work at high repetition rates for the generation of quasi-continuous beams of ions.

To address these limitations, advanced physical vapor deposition (PVD) techniques can be exploited. Among them, Magnetron Sputtering (see Section 3.2) offers precise control over various properties of metallic nanostructured films, including density, morphology,

thickness and composition. However, films produced by PVD need to be deposited onto a substrate, thus the realization of free-standing films via Magnetron Sputteiring represent a non-trivial challenge. During two previous thesis works [63, 64] conducted at Micro and Nanostructured Materials Laboratory (NanoLab) of Politecnico di Milano, a strategy to directly realize Ti free-standing films on the perforated holder has been developed. As sketched in Figure 2.9, a sacrificial layer of sucrose or caramel is used to fill the holes prior to deposition and dissolved afterwards, obtaining free-standing films.

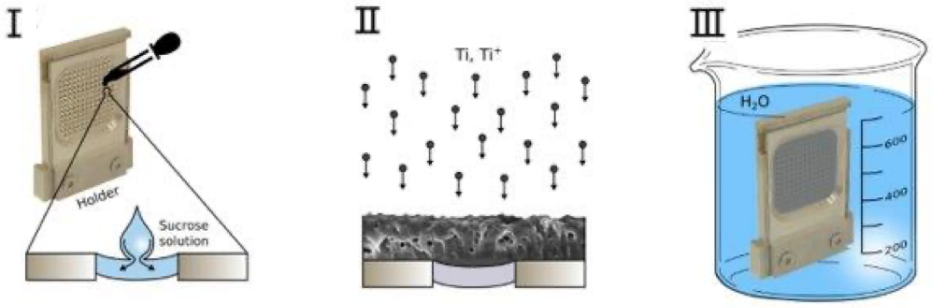

Figure 2.9: Schematic representation of the procedure followed to deposit free-standing films directly on the holder. I) Prior to deposition, the holes are filled one by one with a sucrose solution or caramel and made to solidify. II) The film is deposited via Magnetron Sputtering directly on the holder. III) The target is immersed in water to dissolve the sacrificial layer and obtain the free-standing films in correspondence of the holes [65].

This procedure presents some limitations. The preparation of the substrate is a time consuming process as each hole must filled individually. Moreover, achieving homogeneous hole filling is crucial since any inhomogeneity in the sacrificial layer can lead to the formation of micro-cracks in the films. Additionally, capillary forces allow the caramel/sucrose to fill small holes, in the order of $1-2\ mm$, such as those depicted in Figure 2.8. However, this phenomenon does not apply in the case of larger holes. Films can be produced over a limited range of thickness, between $200-1200\ nm$. Thinner films are prone to breakage, while thicker films are unattainable because the sacrificial layer can not withstand the high temperatures reached during prolonged depositions. When the production of DLTs is addressed, another critical aspect arises. Although PLD allows direct foam deposition onto the film, the resulting coverage is not uniform. This lack of uniformity arises because the free-standing film, acting like a vibrating membrane, causes detachment and prevents proper adhesion of the carbon clusters on the substrate. This effect is detrimental for thinner films.

With the aim of overcoming some of the aforementioned criticalities, another strategy has

been developed in this thesis work, based on a "fishing" approach, already known from the literature, also in the field of laser-driven ion sources [66].

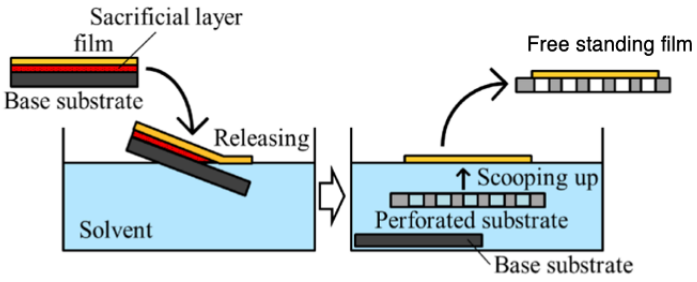

Figure 2.10: Schematic representation of the fishing procedure (adapted from [66]).

Basically, the substrate is covered with a sacrificial layer prior to deposition. After the deposition has been performed, the sacrificial layer is dissolved in an appropriate solvent. Thanks to surface tension, the thin film can float on the solvent surface. Finally, the film is fished with the perforated holder [66].

Concerning laser-driven ion acceleration, the main goal of the thesis work is the optimization of the fishing procedure to realize nanostructured free-standing films exploitable in experiments. Thus, several aspects will be addressed: realization of the sacrificial layer, morphological and mechanical properties characterization of the deposited films and integrity of the realized targets. Two different materials will be investigated to realize the free-standing films, Aluminium (Al) and Copper (Cu), exploiting Magnetron Sputtering. Additionally, the range of obtainable thicknesses and the compatibility with foam deposition will be studied. To produce the complete DLT, PLD will be considered to deposit carbon foams. In addition, this procedure will allow to assess the compatibility of the realized solid layer with the deposition of the low-density one.

Production of carbon foam targets for direct-drive ICF experiments

As outlined in Sections 2.2.2 and 2.2.3, mid-Z materials and plastic foams have shown several advantages over conventional plastic ablators. Specifically, mid-Z materials, such as carbon, can mitigate laser-plasma instabilities, while plastic foams, thanks to their internal structure, are capable of increasing the laser energy absorption, smoothing out laser inhomogeneities and increasing the ablation pressure. Carbon foams, deposited via PLD, represent a promising solution to combine the interesting properties of both mid-Z and porous materials. Additionally, PLD is a more versatile process with respect to the chemical methods conventionally employed to produce plastic foams. For example,

multi-elemental compositions can be easily obtained, together with functionalized density gradients.

It must be noted that, carbon foams have a different structure with respect to plastic foams, as it is evident from Figure 2.11.

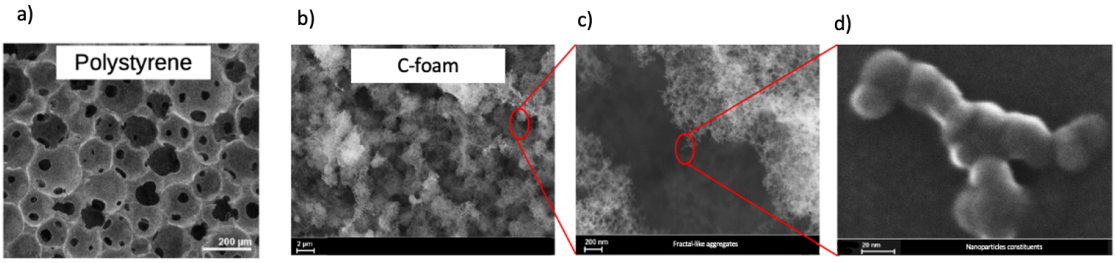

Figure 2.11: Comparison between a) plastic and b) carbon foams. c) and d) show the Carbon foam at different magnification to highlight its multi-scale structure: c) shows fractal-like aggregates with characteristic dimensions in the order of $0.1 - 5\ \mu m$, d) shows the nanoparticles constituents with characteristic dimensions in the order of $5 - 20\ nm$ (adapted from [67]).

Plastics foams are characterized by solid constituents and voids of characteristic dimensions in the order of μm, while carbon foams show a multi-scale structure, with fractal-like aggregates in the order of μm and nanoparticle constituents down to some nm. The laser-foam interaction in conditions relevant for ICF (i.e, ns pulses and moderate intensities) is a widely unexplored topic. A recent theoretical thesis work, conducted in collaboration between ENEA Frascati and Politecnico di Milano [68], addressed this issue. The simulations showed that to enable a high laser energy absorption and conversion in implosion energy, foams with thicknesses up to hundreds of μm are needed, when their density is in the order of tens of mg/cm^3. This thickness value is much greater than those usually deposited at NanoLab for the production of DLTs. The aim of the thesis was to assess the feasibility of depositing carbon foams with these thicknesses via PLD, on different kinds of substrates of interest to perform experiments. The produced targets were also employed in an experimental campaign conducted at the ABC laser facility at ENEA Frascati (see Chapter 6) aimed at a preliminary investigation of the interaction between the laser and a material characterized by lengths scales that are comparable or even smaller than its wavelength.

The deposition techniques employed to realize both targets for laser-driven ion sources and carbon foam targets for ICF are described in the next Chapter 3.

3 | Experimental and Characterization Techniques

3.1. Physical Vapor Deposition

Physical Vapor Deposition techniques (PVD) are based on the vaporization of a solid or liquid target, from which atoms or molecules are ejected and travel in a vacuum or low-pressure atmosphere toward the substrate, where they condense. Among the possible inert working gas, Argon (Ar) is the most employed one. By tuning its pressure, films with different properties can be obtained. It is also possible to perform reactive depositions introducing a reactive gas, like Oxygen (O) or Nitrogen (N). PVD techniques can be classified according to the strategy adopted to vaporize the source material. Some examples are listed in the following:

- *Vacuum Evaporation* is based on the thermal evaporation of the source material, achieved via thermal heating or high energy electron beam heating. The vaporized material travels straight toward the substrate, with few or no collisions thanks to the low pressure. The composition of the vapor is proportional to the relative vapor pressure of the material in the molten source.
- *Sputter Deposition* exploits the bombardment of a target material by energetic ions, obtained by an ion gun or a working gas plasma. Atoms of the target material are ejected from its surface as a consequence of momentum transfer from the energetic bombarding particles. Target can be either mono elemental, compounds, or alloys. The deposited films preserve the bulk composition of the source material.
- *Arc Vapor Deposition* is based on the generation of a high current, low voltage arc between two electrodes. In Cathodic Arc, the vaporized target is the cathode, while the substrate is the anode. The opposite is true for Anodic Arc deposition. The ejected material is strongly ionized.
- *Ion Plating* exploits evaporation, sputtering, or arc erosion of the source material

to obtain the film-forming species. Concurrently, the substrate is bombarded by atomic-sized energetic particles produced in a working gas plasma or by an external ion gun to change film growth process.

- *Pulsed Laser Deposition* uses laser pulses to ablate the target material. A plasma of evaporated species generates and expands toward the substrate. Deposition can be performed either in vacuum or tuning the pressure of a working gas.

The focus of the next Sections 3.2 and 3.3 is on the two PVD techniques employed in the thesis work, Magnetron Sputtering and Pulsed Laser Deposition, respectively. Their working principle is described, and the main differences between different operating modes are highlighted, together with the effect on the resulting film.

3.2. Magnetron Sputtering

Magnetron Sputtering (MS) can be considered an evolution of the simplest sputtering configuration, the so-called diode sputtering. In the diode setup, two electrodes are placed in a vacuum chamber, filled with an inert working gas at low pressure, generally Ar. A high potential difference is set between the cathode and the anode, usually by applying a continuous DC voltage, so that a discharge is generated and a plasma of working gas ions is formed. These ions are accelerated toward the target (the cathode) and, if they are energetic enough, atoms are ejected from it [69]. Indeed, sputtering is a threshold process, since sufficient energy must be transferred to the target atoms to enable them to overcome their surface binding energy. The energy threshold is generally around tens of eV. Once the target atoms are sputtered, they travel toward the substrate (anode). During the sputtering process also electrons are generated and attracted by the anode. Two important parameters can be introduced: sputtering yield and deposition rate. The sputtering yield is defined as the number of ejected target atoms per impinging ion. It has a complex dependence on several quantities like energy and mass of the bombarding ion, angle of incidence, and atomic mass and surface binding energy of target atoms. The deposition rate can be defined as the amount of material deposited per unit time. To increase this quantity, a high ion current at the cathode must be achieved. This can be obtained by increasing the working gas pressure or increasing the discharge voltage. Both solutions may have detrimental effects. At high pressure, the sputtered atoms arrive at the substrate with lower energy, worsening film properties (e.g., compactness). Increasing the voltage, more electrons are produced and attracted toward the substrate, increasing its temperature and damaging the growing film. To avoid these drawbacks, Direct Current Magnetron Sputtering (DCMS) has been implemented.

3.2.1. Direct Current Magnetron Sputtering (DCMS)

In DCMS a DC power supply is employed to apply a constant voltage (hundreds of V) between the two electrodes. The difference with respect to the diode configuration consists in the introduction of a magnetic field that can trap secondary electrons ejected by the target material [69]. This leads to the formation of a denser plasma above the sputtered target ($10^{14} - 10^{16}\ m^{-3}$), and, in turn, to a higher probability of gas atoms ionization, and, thus increasing the deposition rate. Nevertheless, the target atoms' ionization fraction is low, in the order of few percent. The magnetic field is produced by permanent magnets placed behind the cathode/target [69]. For circular electrodes, the magnetic dipole is constituted by an inner solid disk and an outer ring. Three different configurations are possible, according to the relative strength of the magnets [70].

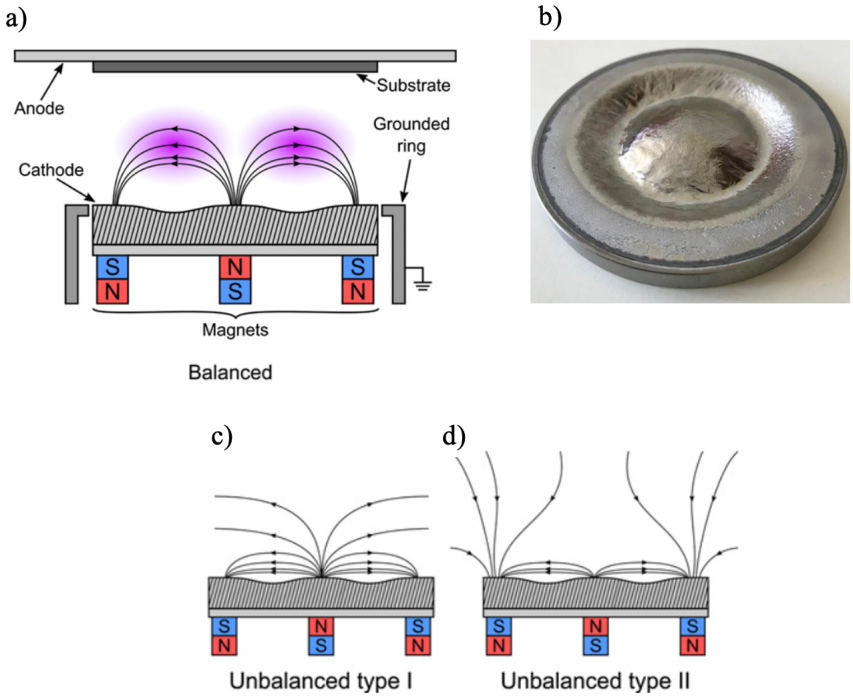

Figure 3.1: Schematic representation of a) balance magnetron, c) unbalanced magnetron of Type I, d) unbalanced magnetron of Type II [70]. b) Picture of a Ti target in which the racetrack is visible.

A balanced magnetron configuration (Figure 3.1a)) is obtained when the two magnets are equivalent. In this case, the magnetic field lines form a radial parabolic shape that closes between the inner and outer poles. A toroidal plasma is formed as a consequence of the combination of this magnetic field shape with the electric field established between

the two electrodes. If the inner magnet is stronger than the outer one, an unbalanced magnetron configuration of Type I is obtained (Figure 3.1c)). Not all the magnetic field lines are closed on the target but some of them are directed toward the wall of the chamber. Conversely, if the outer magnet is stronger than the inner one, part of the magnetic field lines are directed toward the substrate. This configuration is called Type II (Figure 3.1d)) [69, 70]. The main difference between these configurations lies in the confinement of the plasma. In the balanced magnetron, the plasma is strongly confined near the target, thus the substrate sees relatively low ion current densities (in the order of 1 mA/cm^2). In the unbalanced magnetron of Type I, the current density at the substrate is even lower. On the contrary, with the unbalanced magnetron of Type II, the plasma can extend up to the substrate, leading to higher current densities ($> 2\ mA/cm^2$) [69, 70]. These differences affect film growth. For example, denser films can be obtained with Type II magnetrons, while porous metal films can be produced with Type I [69, 70]. It is worth noticing that the particular toroidal-plasma shape causes an annular consumption of the target. This eroded region, visible in Figure 3.1b), is called racetrack. As a consequence of this peculiarity, no more than 50% of the sputtered target can be efficiently exploited.

3.2.2. High Power Impulse Magnetron Sputtering (HiPIMS)

Magnetron sputtering can also be operated in pulse mode. In particular, High Power Impulse Magnetron Sputtering (HiPIMS) exploits pulses with a time duration, known as pulse on time, in the range $5 - 5000\ \mu s$, with a repetition frequency between $10\ Hz - 10\ kHz$. In these conditions, high peak power densities, in the order of few kW/cm^2, can be obtained, while maintaining an average value of few W/cm^2, close to that of the DCMS regime [70]. Thus, operating at low duty cycles (defined as the ratio of the pulse on time to the overall duration of the cycle), in the order of $1-5\%$, high target peak current densities (A/cm^2) can be reached, about two-three orders of magnitude larger than those achievable with DCMS. The transition between a DCMS-like operating mode and a HiPIMS mode is evident in the voltage-current characteristic curves. Assuming a power-low dependence of the current on the voltage, the slope of the curve is reduced when moving from DCMS to HiPIMS, as shown in Figure 3.2a). The higher discharge current leads to a higher electron plasma density with respect to DMCS, around $10^{18}\ m^{-3}$. Consequently, a larger fraction (tens percent) of the sputtered atoms is ionized. The higher fraction of ionized species can be detected via Optical Emission Spectroscopy (OES). During the sputtering process, plasma species are excited to higher electronic levels by collisions with electrons. De-exciting, they emit radiation in the visible range. Each peak in the resulting spectrum can be associated to a specific plasma species, either neutrals or ions [71]. The DCMS

spectrum is dominated by Ar peaks, while in HiPIMS the most important contribution come from the sputtered material and the fraction of ionized species increases. This difference is well exemplified in Figure 3.2b) which reports the OES spectra of a DCMS discharge and a HiPIMS discharge considering titanium (Ti) as sputtered target.

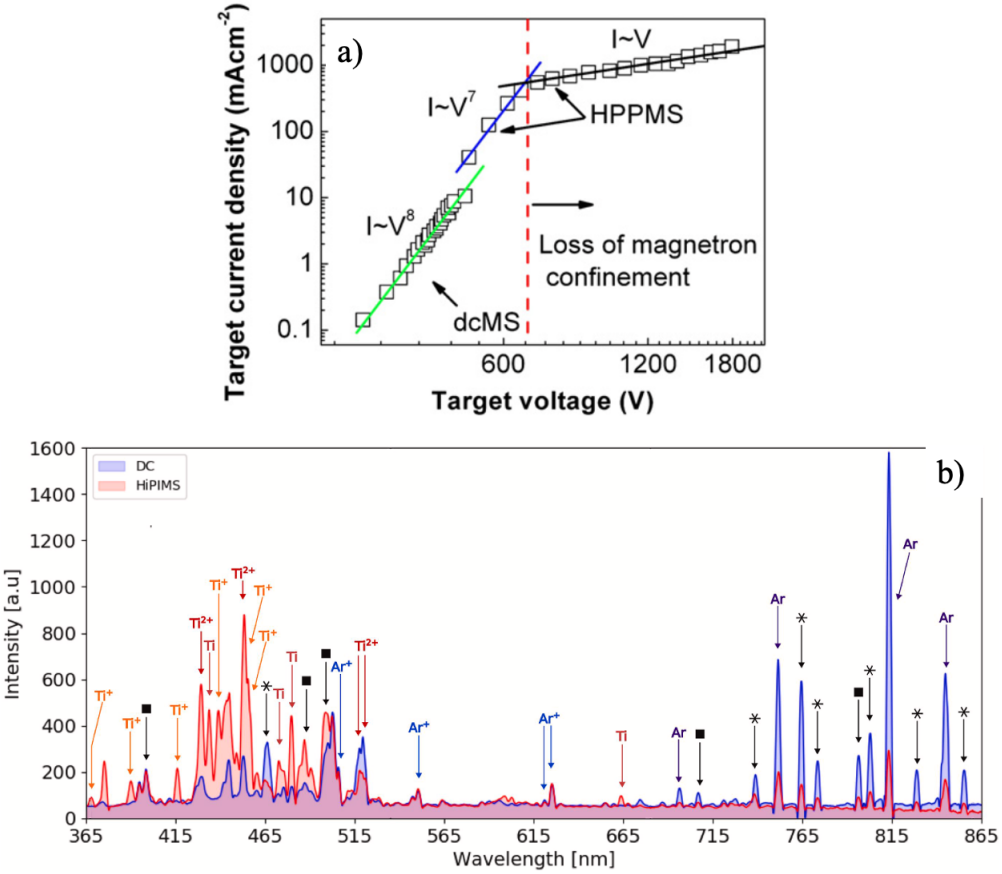

Figure 3.2: a) Typical current-voltage characteristic curve of a Magnetron Sputtering discharge operated from a DC-like regime to HiPIMS [72]. b) OES of a Ti-DCMS discharge (blue) and Ti-HiPIMS discharge (red). The right portion of the spectrum is mainly attributable to Ar, while the left portion to Ti [73].

The high discharge current densities characterizing HiPIMS are reached thanks to a process known as ion recycling, schematically represented in Figure 3.3a) [70]. It can be briefly described as follows. Working gas ions are attracted toward the target where they sputter some of the target atoms and are neutralized. Gas atoms embedded in the target are ejected under bombardment by other ions. A fraction of the ejected gas atoms are lost while the others are ionized with a certain probability (α_g) and attracted back toward the target with a probability β_g. This is known as working gas recycling [69]. In a similar fashion, a fraction of the sputtered target atoms are deposited at the substrate or lost,

while the another portion is ionized with a probability α_t and attracted back toward the target with a probability β_t, promoting further sputtering (self-sputtering). This is known as self-sputter recycling [69]. The relative importance of the two recycling mechanisms depends on several factors including the set process parameters and the specific sputtered material.The discharge current density evolves in time according to the importance of ion recycling, as shown in Figure 3.3b).

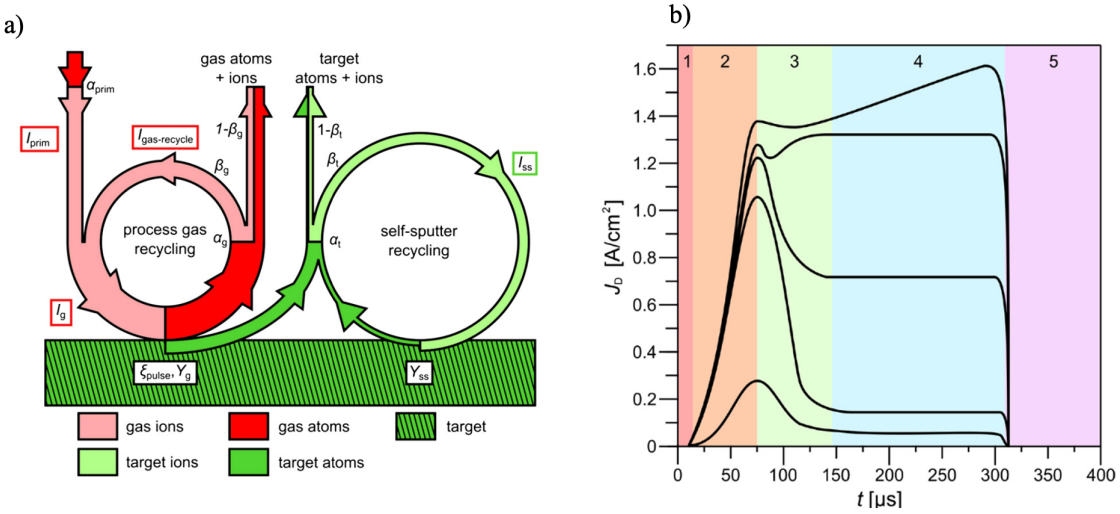

Figure 3.3: a) Scheme of the ion recycling model. b) Possible temporal evolution of the discharge current density according to the specific processes characterizing the HiPIMS plasma. In all cases, a pulse on time equal to 300 μs is considered [69]

.

The initial phase of the discharge, characterized by a current rise, is ruled by the working gas ions (1-2 in Figure 3.3b)). Subsequently, a current decrease occurs, due to gas rarefaction, mainly attributed to the impact with sputtered species (2-3 in Figure 3.3b)). At this point, the discharge current can evolve in three different ways. In the case of low sputtering yield materials, the discharge current decreases, reaching a plateau at low values, comparable to those achieved in DCMS [69]. For high sputtering yield materials, the discharge currents can reach significantly higher values thanks to ion recycling. In the middle curve of Figure 3.3b), ionized atoms of the working gas are necessary to induce self-sputtering. This regime is called working gas sustained self-sputtering [69]. The top two curves show considerable ion recycling (working gas and/or self-sputtering) which leads to the self-sustained self-sputtering. In this case, a large fraction of the sputtered species is attracted back to the target and the discharge is dominated by metal ions [69]. In general, thanks to the high fraction of ionized atoms, HiPIMS leads to film densification and better adhesion to the substrate, with respect to DCMS. Additionally, the energy of

the depositing species can be properly tuned, for example by applying a substrate bias, to tailor film properties. The main drawback of the HiPIMS regime resides in the lower deposition rate with respect to DCMS [74]. This can be attributed to the back attraction of the highly ionized metal atoms toward the target [75]. Additionally, it is known that the increase in ion energy causes re-sputtering and densification of the growing film, reducing its thickness and, consequently, the deposition rate [76].

Magnetron Sputtering deposition system at NanoLab

The Magnetron sputtering apparatus employed in this thesis work can be operated either in DCMS or HiPIMS regimes, exploiting two DC power supply of 6000 W and 1500 W connected to a pulsing module. Two confocal magnetron sources are located in the bottom part of a vacuum chamber, while the sample holder is in the upper part. It is connected to a motor which enables its rotation to assure a better uniformity. A negative bias voltage can be applied to it, to tailor the energy of the film forming ions. Vacuum is obtained by operating in series two pumps. The primary scroll reduces the pressure down to $1-10\ Pa$, while the turbomolecular pump can provide the high vacuum $10^{-5}\ Pa$.

3.2.3. Film Morphology and Stress Generation

Film growth and morphology

According to the so-called Volmer-Weber mechanism [77], film growth develops in different stages. At the beginning, the particles of the vaporized flux sticks on the substrate, thus becoming adatoms characterized by a certain mobility. When two or more adatoms impinge, nucleation of small islands occurs. Proceeding with the deposition, these islands get larger and they may eventually coalesce. The substrate is covered by a continuous film which increases its thickness as long as deposition proceeds [77]. The resulting film morphology is mainly dominated by surface and bulk diffusion processes of adatoms. The parameter which has the major impact on these is the homologous temperature T_h, defined as the ratio between the substrate temperature and the material melting temperature. According to this parameter only, it is possible to develop a Structure Zone Diagram, in which four zone can be individuated [78]:

- **Zone I** ($T_h < 0.2$): surface diffusion is negligible, therefore the adatom mobility is low, causing a continuous nucleation of grains. As film thickness increases, the result is a fine columnar grain microstructure with the presence of pores at the grain boundaries and lattice defects. The dimensions of the grains slightly change during growth [79].

- **Zone T** ($0.2 < T_h < 0.3$): in the transition zone surface diffusion becomes significant but grain boundary diffusion is still limited. This leads to competitive growth causing the development of V-shaped grains with an inhomogeneous structure across the film thickness. The microstructure is characterized by small and fine grains for the first deposited layers, and larger grains for the subsequent ones [79].
- **Zone II** ($0.3 < T_h < 0.5$): both surface and bulk diffusion are operative, leading to uniform columnar grains, the dimensions of which increase with increasing film thickness, both near the substrate and at the surface [79].
- **Zone III** ($T_h > 0.5$): in this case, also crystallization can take place, as the deposition temperature is close to the melting one, resulting in a dense microstructure with large grains.

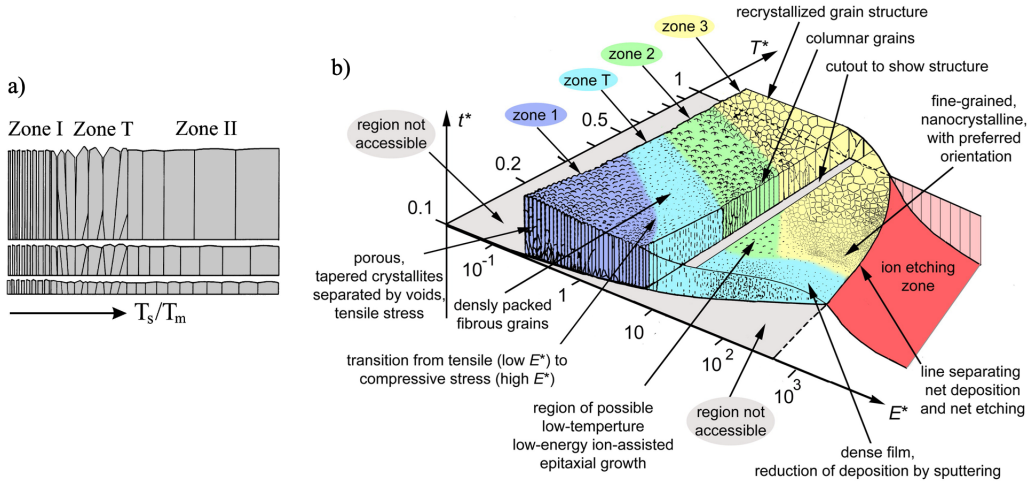

Figure 3.4: a) Structure Zone Model which takes into account only the temperature effect. b) Revisited Structure Zone Model to take into account the effects of energetic ion bombardment, taken from [80]. E^* is the normalized energy axis, accounting for displacement and heating effects caused by high energy bombarding species. T^* is a generalized temperature accounting for temperature shifts caused by the impinging high energy species. t^* represents the thickness of the film, which can diminish due to etching.

This simple description is complicated if one considers the effect of pressure, which determines the energy of the film forming species, as in the case of DCMS. Therefore, also kinetic effects should be taken into account in addition to thermal ones mainly determined by T_h. The overall picture is further enriched if energetic and ionized depositions, such as HiPIMS, are considered. In this case, the growing film is subjected to high fluxes of energetic particles which can cause temperature shifts, heating displacement, etching

(re-sputtering of the grown film), and other effects that must be taken into account. A complete diagram that considers all the effects mentioned was developed by Anders and is shown in Figure 3.4 [80].

Stress generation and evolution

Stress generation and evolution during film growth is a complex topic, which is still not well understood. Without claiming for exhaustiveness, a brief overview of the possible stress inducing mechanisms encountered in PVD techniques is presented. The film stress is the result of the combination of these contributions, some of which operate simultaneously. Intrinsic stresses are directly connected to growth kinetics. Generally, during the nucleation stage, compressive stresses are registered, due to capillary forces arising in the small islands bonded to the substrate. During the coalescence stage, grain boundaries are formed and tensile stresses originate, as a consequence of the attractive forces between the columns. In the post-coalescence stage, compressive stresses may arise, meaning that the film is denser than it would be at equilibrium. This is attributed to the insertion of atoms at grain boundaries [79]. Moreover, grain growth with increasing film thickness is an additional source of strain [79]. In general, if the grain size changes at the surface of the film, the tensile stress induced in the coalescence stage may be relaxed in the new layers. If the grain size changes in the bulk, tensile stresses are generated since the film is constrained to the substrate [79]. Consequently, it can be argued that materials growing according to Zone I are characterized by tensile stress, that reaches a steady-state value, since the grain dimension does not change. Zone T materials show transitions between Compressive-Tensile-Compressive (CTC) stresses [77]. This is because surface diffusion may be enough to promote densification and tensile stresses are also relaxed by the formation of C-shaped grains. Conversely, in Zone II films, since grain dimensions change also in the bulk, an additional tensile stress is developed [79, 81]. When energetic depositions are considered, the high energy of the film-forming species is an additional factor affecting film stresses, usually causing compressive ones [81]. It can enhance adatoms' mobility, favoring the incorporation of atoms at grain boundaries. Additionally in the atomic peening mechanism, momentum is transferred from the bombarding species to the atoms of the film, leading to a denser configuration or to stress-inducing defects, like entrapment of interstitial working gas atoms or recoil implantation of the film atoms [81]. The overall stress state of the film can be considered as the superposition of intrinsic stresses and energetic bombardment-induced stresses, which can be considered as the mechanisms acting independently from one another.

3.3. Pulsed Laser Deposition (PLD)

Pulsed Laser Deposition (PLD) belongs to the family of PVD techniques. In this case, a laser is used to vaporize the target material. The process can be qualitatively described as follows. In a vacuum chamber, a target is shot by subsequent laser pulses. The laser energy is transferred to the material and, consequently, the target material is removed from its surface [43], generating a plasma. The ablated species travel in a controlled background atmosphere until they reach the substrate where the film is grown. PLD is characterized by a variety of operational parameters which are tunable over wide ranges, making it a versatile technique. By properly choosing the working conditions, compact or porous nanostructured films of different materials can be obtained, with controlled properties, on virtually, any kind of substrates [42, 43]. Some examples of working parameters are laser pulse duration, laser fluence, repetition rate, background pressure, and working gas composition. The resulting film properties depend on the target material. A schematic view of the PLD apparatus is shown in Figure 3.5. In general, if the deposition process is carried out in vacuum, the ablated species are free to expand, reaching the substrate with sufficiently high energy to form a compact film. When a working gas at high pressure (from tens to hundreds of Pa) is present, porous materials, known as foams, can be obtained through a snow-fall-like aggregation process [42]. The ablated species are slowed down via collisions with gas atoms or molecules and the plasma plume is confined in space. This enables the sticking of ablated species among them, while in flight toward the substrate. Subsequently, larger aggregates increase their dimensions by clustering smaller nanoparticles present in the vacuum chamber. Finally, the low-density fractal-like aggregates reach the substrate, obtaining a foam.

According to the laser pulse duration, two regimes of deposition can be identified, characterized by two different ablation physics. Nanosecond-PLD (ns-PLD), the most employed one, is based on a thermal ablation process. Femtosecond-PLD (fs-PLD) is driven by a more complex and poorly understood electronic ablation dynamics [43] and is less widespread. In the following Sections 3.3.1 and 3.3.2, ns-PLD and fs-PLD are addressed. The main aim is considering how the different pulse lengths and pressures affect films' morphology and density, specifically focusing on Carbon as ablated material. This discussion is relevant in the context of the thesis work since, as anticipated in Chapter 2, they are currently emplyed as near-critical layers in DLTs for particle acceleration and might be promising material for the ablation layer in ICF targets.

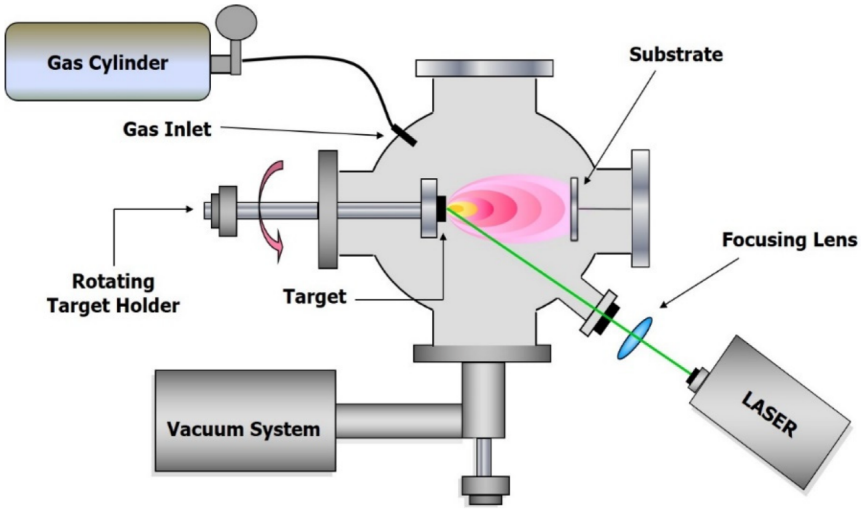

Figure 3.5: Schematic representation of the PLD apparatus. [82].

3.3.1. ns-PLD

Ablation mechanisms in ns-PLD

In ns-PLD, the laser pulse duration is longer than both electrons and ions dynamics time scales, which are in the order of fs and ps, respectively. Consequently, the laser photons can couple to both electronic and ionic vibrational modes, increasing the temperatures of both species. This leads to the heating of the material, with consequent melting of a portion of the target surface. Thus, vaporization occurs in the thermal ablation regime [83]. Additionally, the laser pulse is long enough to interact with the plasma plume. The consequence is a poor energy transfer to the target. The ablated species are electrons, atoms, ions, and small atomic clusters [43]. The ablation process in ns-PLD is schematically reported in Figure 3.6a)).

Effect of working gas pressure on Carbon foam properties

As previously anticipated, when depositions are carried out in vacuum ($10^{-3}Pa$), a compact, near-bulk density film could be obtained [43]. When a working gas is present, the ablated species are slowed down via collisions and they can cluster together. Increasing the gas pressure, the collision probability is increased and the ablation plume is more confined, leading to a higher sticking probability. Consequently, larger Carbon aggregates are formed, with dimensions varying according to an exponential trend, leading to a porous nanostructured material, with a sponge-like morphology (see Figure 3.7a)) [43]. As a consequence, density decreases with increasing pressure. At low pressures, the film has a density close to the bulk one, since gas is not effective in slowing down the ablated

species. Then, a sharp decrease is observed when the pressure overcomes the threshold value corresponding to the transition between compact and porous film. Further increasing the pressure leads to a decrease in density until an asymptotic value is reached, as the energy of the ablated species can not be further reduced [43].

ns-PLD system at NanoLab

The ns-PLD set up at NanoLab consists of a Q-switched Nd:YAG laser (wavelength = 532 nm), capable of delivering pulses with a duration of $5-7$ ns, a repetition rate of 10 Hz and a maximum energy per pulse of 1 J. Thanks to proper optics, the laser is directed toward the deposition chamber and focalized on the target with an angle of 45 °. Both target and substrate are mounted on motorized holders which can rotate and translate in the three directions. The required level of vacuum is obtained by the operation in series of a scroll pump, for low vacuum, and a turbomolecular pump, for high vacuum.

3.3.2. fs-PLD

Ablation dynamics in fs-PLD

In the fs regime, the laser pulses are shorter than the characteristic time scales of ion dynamics, thus energy is transferred directly only to the target electrons [84]. Additionally, the energy transfer is more efficient than in the ns- regime, since the fs laser pulse can not interact with the plasma plume. Therefore, the ablation of the target is attributed to electrons. Two main electronic ablation processes have been identified [84], non-thermal melting and Coulomb explosion. Non-thermal melting consists of a quick disordering of the material, caused by the motion of ions. Despite being cold, ions are subjected to forces arising from a sudden change in their potential energy as a consequence of the excitation of a large number of electrons. Coulomb explosion sets in when the electrons are ejected from the target material. Thanks to space-charge effects, electromagnetic fields can be produced and ions can be emitted, if they can overcome their binding energy. These mechanisms lead to target fragmetation. Consequently, the ejected material is in the form of nanoparticles. The ablation process in fs-PLD is schematically reported in Figure 3.6

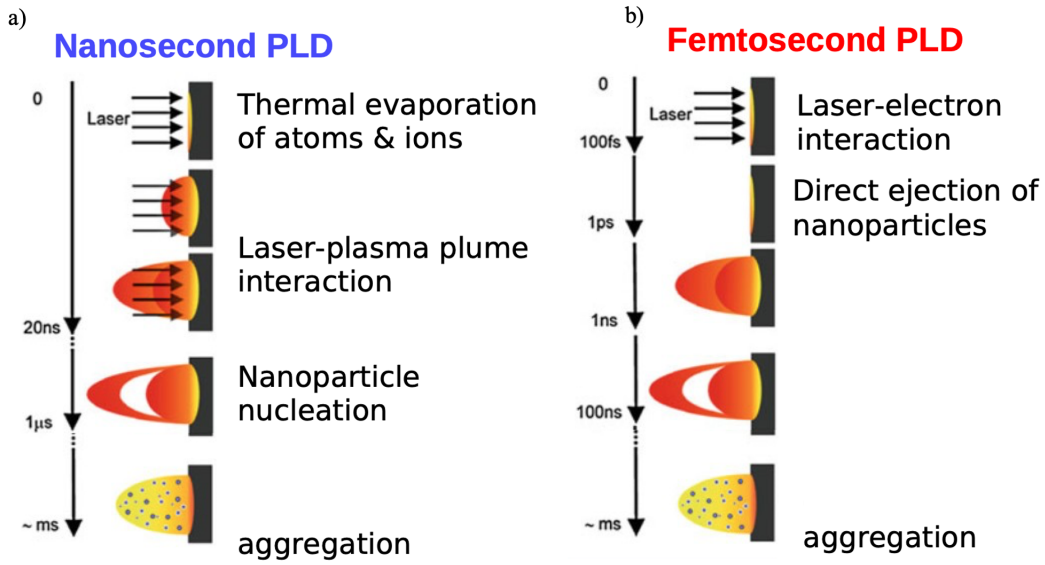

Figure 3.6: The Schematic representations of a) the ns-PLD ablation process and of b)the fs-PLD ablation process (adapted from [67]).

Effect of working gas pressure

Despite the different ablation physics, the general trends highlighted for ns-PLD are still valid. Aggregates tend to increase their dimensions with increasing pressure, leading to a more porous, less dense carbon foam. Nevertheless, there is one relevant difference between fs-PLD and ns-PLD aggragates [43]. While ns-PLD carbon foams are characterized by one family of aggregates, two populations can be identified in the case of fs-PLD, a large aggregate population and a small aggregate population [43]. Consequently, with increasing working gas pressure, the transition from a compact to a porous film is not net, as it was in the case of ns-PLD. An intermediate step is present, in which a mixed deposit develops, consisting of a nanostructured compact film covered with porous aggregates. Moreover, the resulting Carbon foam morphology is different, showing a web-like network (see Figure 3.7b)). Additionally, at the same pressure level, fs-PLD deposited foams result denser with respect to ns-PLD ones [43].

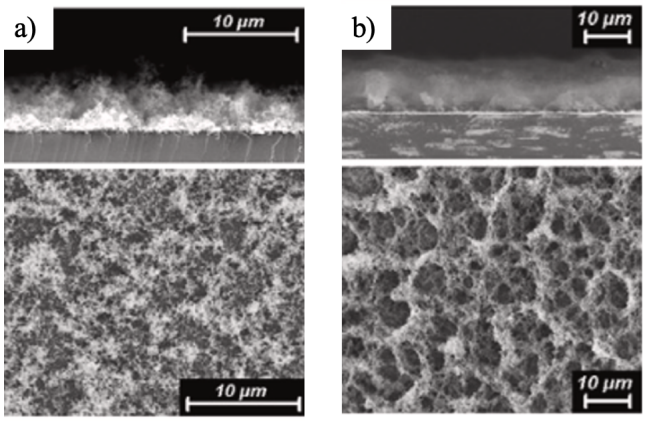

Figure 3.7: a) ns-PLD and b) fs-PLD SEM images of carbon foams deposited under the same condition. The different morphology is evident (adapted from [43]).

fs-PLD system at NanoLab

The fs-PLD setup at NanoLab consists of a CPA Ti:Sapphire laser (wavelength = 800 nm), capable of delivering pulses with a duration of 80 fs, a repetition rate of 1 kHz and a maximum energy per pulse of 5 mJ. Thanks to proper optics, the laser is directed toward the deposition chamber and focalized on the target with an angle of 45 $grad$. Both target and substrate are mounted on motorized holders which can rotate and translate in the three direction. The required level of vacuum is obtained by the operation in series of a scroll pump, for low vacuum, and a turbomolecular pump, for high vacuum.

3.4. Scanning Electron Microscopy (SEM) for Morphological Characterization

In a Scanning Electron Microscope (SEM), an electron beam is exploited to image submicrometric objects. Both planar and cross-sectional views can be obtained. The former provides surface morphology information while the latter can be also used to estimate the thickness. The analysis is performed in vacuum to reduce the probability of interaction of the electrons with atoms and molecules of the atmosphere. Electrons are produced by an electron gun via thermoelectric effect or field effect. Then, they are accelerated reaching energies in the range $1 - 30$ keV. Subsequently, the electron beam is properly focused and bent to scan the sample surface on which it is focused. The interaction gives rise to different signals, each of which carries different information. Backscattered electrons (BSE) are generated during the elastic interaction of electrons with the nuclei of the target material. Their yield depends on the square of the atomic number, thus they pro-

vide qualitative information on sample composition, with brighter areas corresponding to higher-Z elements. Secondary electrons (SE) are produced after inelastic scattering with the valence electrons of the sample. Their yield has a weak dependence on Z, while it is strongly influenced by the incidence angle. Additionally, they are emitted with energies lower than 50 eV, thus only those generated at the superficial layer can come out of the sample. Consequently, SE do not provide information on sample composition but they are sensitive to surface topology. X-rays are emitted during the de-excitation of electrons, previously excited by the primary beam. They can be exploited to perform Energy Dispersive X-Ray Spectroscopy (EDXS). An X-ray spectrum is recorded, in which some peaks, corresponding to characteristic X-rays of the elements present in the sample, are visible. Their intensity is correlated with elemental abundance. Therefore, by properly analyzing the X-ray spectrum, quantitative information on sample composition can be obtained. EDXS is also exploited to measure the mass thickness (i.e., the product between the mass and the density of the material), which is related to the intensity ratio between the characteristic X-rays of the sample to those of the substrate. By combining SEM and EDXS it is possible to retrieve the film density, dividing the mass thickness by the geometrical thickness [85].

3.5. Surface Curvature Method for Stress Characterization

Several techniques for measuring the stress state of a film are reported in the literature. Among them, the surface curvature method represents a valuable choice, having the major advantage of being non-destructive [79, 81]. The stress state of the film influences that of the substrate, inducing its curvature. These two quantities are related to one another through the Stoney equation [86]:

$$\sigma_f = \frac{E_s}{1-\nu_s}\frac{t_s^2}{6t_f}(1/R - 1/R_0) \tag{3.1}$$

where σ_f is the stress of the film, E_s and ν_s are the Young modulus and the Poisson ratio of the substrate, t_s and t_f are the substrate and the film thicknesses, respectively, R_0 is the substrate's curvature radius prior to deposition, R the one after it. The Stoney equation is valid if thin substrates are used ($t_s << R$) and under the thin film approximation (i.e., $t_f << t_s$). If the latter holds, the curvature behavior of the substrate depends only on its mechanical properties and not on those of the deposited film. The only film parameter coming into play is its thickness.

The apparatus installed at NanoLab is based on laser reflection [87]. A laser beam (5 mW, 630 nm) passes through two etalons used to duplicate it along two different directions forming an angle of 45°. A 3x3 beam array is formed. The central spot is obscured because it is more intense than the four lateral ones. Thus a 2x2 array is exploited for the measurement. After proper focusing, light impinges on the sample and is reflected with an angle of 60°. The reflected spot positions are recorded by a camera. A sequence of frames is acquired and elaborated with a computer code that computes the relative distance between the centroids of the four spots from which the curvature radius can be obtained. This measurement is computed before and after the thin film has been deposited on the substrate. Finally, stresses are retrieved employing the Stoney equation.

4 | Deposition of Nanostructured Materials for Targets in Laser-Plasma Interaction Experiments

In this Chapter, the production and characterization of thin metallic films and carbon foams are addressed. Indeed, as already outlined in Chapter 2 knowing the properties of the target is of fundamental importance. Cu and Al films are widely employed as targets for laser-driven ion sources. In Section 4.1 their production via Magnetron Sputtering is addressed. For both materials, the deposition parameters and plasma characteristics are described, moving then to their morphological and mechanical characterization. Finally, a discussion of the obtained results is presented for both Cu and Al. These preliminary depositions are also exploited in Chapter 5 to evaluate the deposition rates in the different working conditions (i.e. DCMS, HiPIMS) and to assess the effect of a sacrificial layer on the film properties. Section 4.2 is focused on the production of carbon foams via ns- and fs-PLD and their morphological characterization.

4.1. Production and characterization of thin metallic films via Magnetron Sputtering

4.1.1. Copper thin films deposited via DCMS and HiPIMS

One of the aims of the thesis work is the realization of free-standing films through a fishing procedure. Since the thickness of the free-standing film is one of the target parameters which can be tailored to tune the energy of the accelerated ions, it has been decided to explore a reasonably wide range of thicknesses. For each material and deposition condition, some points in the range $100 - 800\ nm$ were selected as case studies.

Deposition Parameters and Plasma Characteristics

Copper films were deposited via DCMS and HiPIMS according to the parameters reported in Table 4.1. In both cases, single side 500 μm thick (100) Silicon (Si) wafers, polished with isopropyl alcohol, were considered as substrates for film production. The depositions were performed using a circular Cu target (diameter = 76 mm, purity = 99.99%). Prior to each deposition, the vacuum chamber was evacuated to a base pressure lower than $10^{-6}/10^{-7}$ $mbar$ and then filled with Ar (99.99% purity) with a constant inlet gas flow rate of 80 $sccm$ and pressure equal to 0.5 Pa. Substrates were fixed on a rotating holder (rotational speed = 5 rpm) to assure better uniformity during the deposition. No heating was applied to the substrates.

	Power [W]	Voltage [V]	Current [A]	Pulse Duration [μs]	Duty Cycle
DCMS	547(600)	517(600)	1(2)	-	-
HiPIMS	295(350)	676(900)	0,3(10)	100	1,75

Table 4.1: Deposition parameters in DCMS and HiPIMS. The values in round brackets are the set values.

Copper is one of the metals with the highest sputtering yield, second only to Silver [88]. This is evident from the large current densities achieved at relatively low voltages (see Figure 4.5). Concerning the HiPIMS regime, Figure 4.1a) represents the evolution of the discharge current density as a function of the applied voltage. In all cases, the pulse length is kept fixed at 100 μs. The obtained shapes are in agreement with the ones reported in the literature, showing a transition from a middle-range HiPIMS discharge to a full HiPIMS operating mode [88]. At lower voltages, 590 V in this case, the current density increases up to a maximum value and then decreases. This means that the plasma is ruled by Argon (Ar) ions. Increasing the voltage, the sputtered metal begins to greatly affect the discharge, and the condition of sustained self-sputtering is achieved, corresponding to a change in the slope of the curve. A steady state is then reached, since the increased sputtering and ionization are compensated by losses of the sputtered atoms, which can reach the substrate, contributing to the deposition rate. As the voltage is increased, the discharge current is higher and the steady state is reached faster as all the processes happen earlier in time [88]. The voltage-current characteristic curve in Figure 4.1b) shows a net change in slope, representing a net transition between the middle range and the HiPIMS regimes.

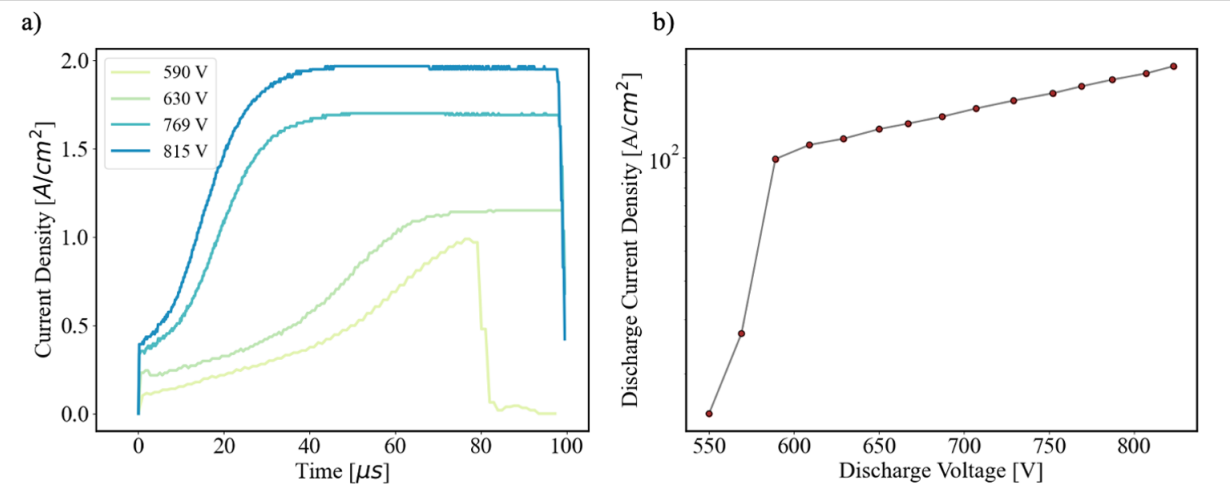

Figure 4.1: a) The temporal evolution of the experimentally acquired discharge currents as a function of the applied voltage. b) The voltage-current characteristic curve for the Cu HiPIMS discharge.

Considering the OES represented in Figure 4.2, it is possible to appreciate the difference between the HiPIMS and the DCMS plasma compositions. In DCMS, the contribution of Ar is dominant even though some peaks attributed to atomic and ionized Cu are also visible, thanks to the high sputtering yield. These emission lines gain in intensity when working in HiPIMS conditions, while the contribution of Ar is strongly reduced.

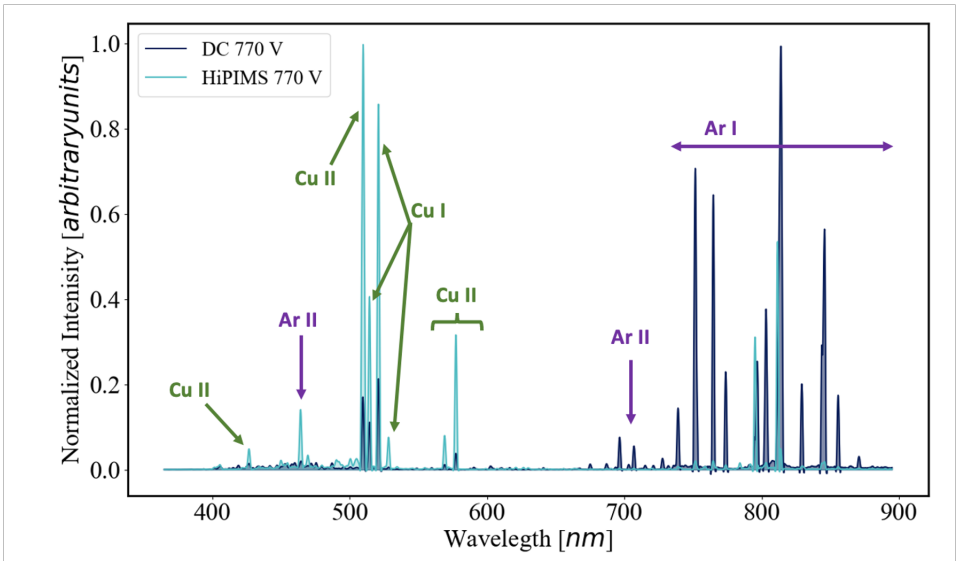

Figure 4.2: OES of the Cu plasma in DCMS and HiPIMS under comparable working conditions. Cu I and Ar I refers to atomic Cu and Ar, while Cu II and Ar II refer to Cu and Ar singly ionized. The peaks have been attributed according to [89, 90]

Morphological Characterization

In Figure 4.3, the SEM planar and cross-sectional views of two samples (approximately 400 nm thick) deposited in DCMS and HiPIMS are reported for comparison. From the morphological point of view, no substantial difference between DCMS and HiPIMS deposited films are observed. They show a compact microstructure with small grains and smooth surfaces. As expected, grains dimensions increase with increasing film thickness [91] and they are larger in the case of DCMS. The cross section images (Figure 4.3c) and d)) reveal a ductile behavior to fracture for the films. Indeed the columnar grain structure expected for Cu films according to the literature [92] is barely visible due to film deformation after sample cleavage. Moreover, it is possible to notice that portions of the film are detached from the substrate, due to the low adhesion of Cu to Si.

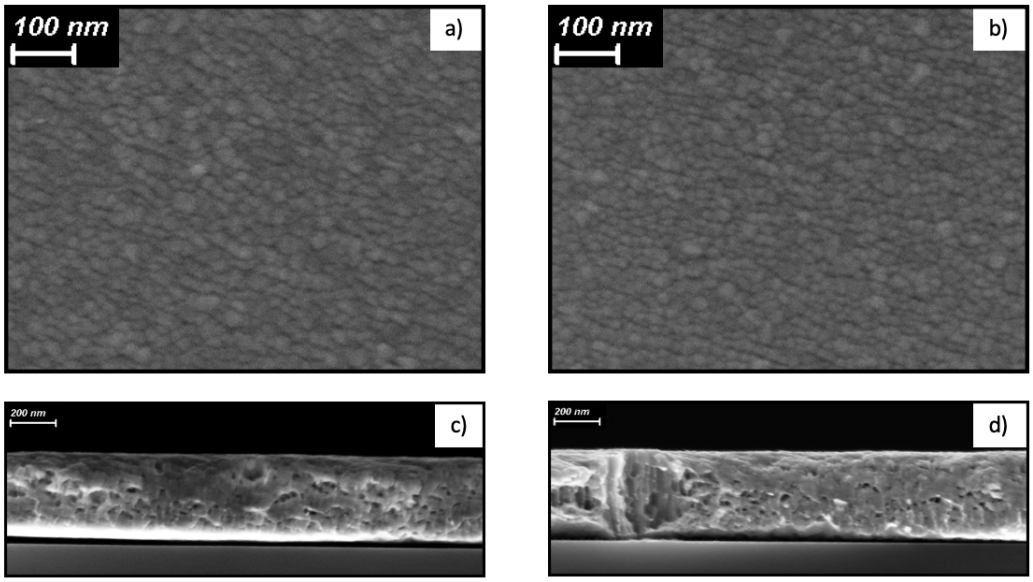

Figure 4.3: SEM images of Cu samples with a thickness around 400 nm realized via DCMS (a) planar view and c) cross-section) and HiPIMS (b) planar view and d) cross-section).

Mechanical Characterization

The mechanical characterization was performed exploiting the surface curvature method described in Chapter 3. Three substrates were mounted on the holder during each deposition, to have better statistics. The uncertainties have been calculated as experimental standard deviation from the set of nominally identical samples. It is worth noticing though, that at low thicknesses the error bars are quite large since the growth is still not fully developed, thus the measurements at $100 - 200$ nm are purely indicative. As shown

in Figure 4.4, films deposited in DCMS show relatively low values of stresses. Moreover, they are all tensile except for one point at around 200 nm of thickness. On the other hand, films deposited in HiPIMS show a transition from compressive stresses at lower thicknesses to tensile stresses.

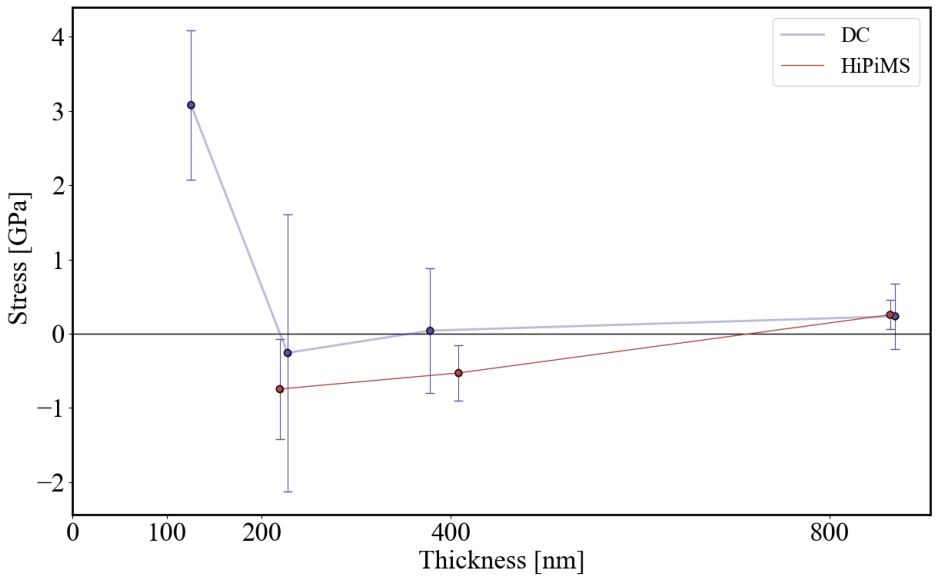

Figure 4.4: Average residual stress as a function of thickness for Cu films deposited in DCMS (blue line) and HiPIMS (red line).

Discussion of the results

Generally, tensile stresses are correlated to grain boundary shrinkage. This phenomenon is more relevant when bombardment occurs via low-energy ions. The resulting film contains a large fraction of voids which, due to the surface tension of their inner surfaces, tend to shrink the film generating tensile stresses [92]. On the other hand, the impact of high-energy ions enhances surface diffusion and local heating, promoting the collapse of voids and also contributing to the generation of compressive stresses via ion peening [92]. The experimental results obtained by the Stoney measurements are in agreement with these hypotheses: films deposited via DCMS are mostly characterized by tensile stresses, while films obtained via HiPIMS show compressive stresses. Moreover, the stress evolution and fine grain microstructure of the DC-sputter film are close to the typical features of low-mobility materials. Indeed, considering the substrate at room temperature and $T_m = 1368\ K$, the homologous temperature results $T_h = 0.21$.

4.1.2. Aluminum thin films deposited via DCMS and HiPIMS

Deposition Parameters and Plasma Characteristics

Aluminum films were deposited via DCMS and HiPIMS and biased HiPIMS according to the parameters reported in Table 4.2. In all cases, single side 500 μm thick (100) Silicon (Si) wafers, polished with isopropyl alcohol, were considered as substrates for film production. The depositions were performed using a circular Al target (diameter = 76 mm, purity = 99.99%). Prior to each deposition, the vacuum chamber was evacuated ti a base pressure lower than $10^{-6}/10^{-7}$ $mbar$ and then filled with Ar (99.99% purity) with a constant inlet gas flow rate of 80 $sccm$ and pressure equal to 0.5 Pa. Substrates were fixed on a rotating holder (rotational speed = 5 rpm) to assure better uniformity during the deposition. No heating was applied to the substrates. The rationale behind the third regime will be explained in the following.

	Power [W]	Voltage [V]	Current [A]	Pulse Duration [μs]	Duty Cycle
DC	506(560)	470(600)	1(2)	-	-
HiPIMS	564(620)	770(850)	0.6(10)	100	1.75
HiPIMS +bias(*)	506(560)	750(850)	0.6(10)	100	1.75

Table 4.2: Deposition parameters in DC, HiPIMS and HiPIMS + delayed bias. The values in round brackets are the set values. The bias parameters are reported in Table 4.3

	Power [W]	Voltage [V]	Current [A]	Pulse Duration [μs]	Delay [μs]
***bias**	0(100)	100(110)	0(2)	100	60

Table 4.3: Delayed bias parameters. The values in round brackets are the set values.

Al is characterized by a self-sputtering yield of 1.1, which exceeds unity but is much lower compared to that of Cu equal to 2.6 [69]. Consequently, the discharge current density can still evolve in the self-sustained self-sputtering regime and reach a plateau [69, 88], but on longer time scales with respect to Cu. In fact, a pulse duration of 400 μs is necessary to observe the full evolution. Within 100 μs, it is reasonable to assume that working gas self-sputtering is established. Furthermore, still concerning the waveforms, a transition between a middle-range HiPIMS discharge to a HiPIMS discharge can be observed with

increasing voltage [93]. However, this transition is not clearly evident in the characteristic curve depicted in Figure 4.5b), likely due to the lower self-sputtering yield.

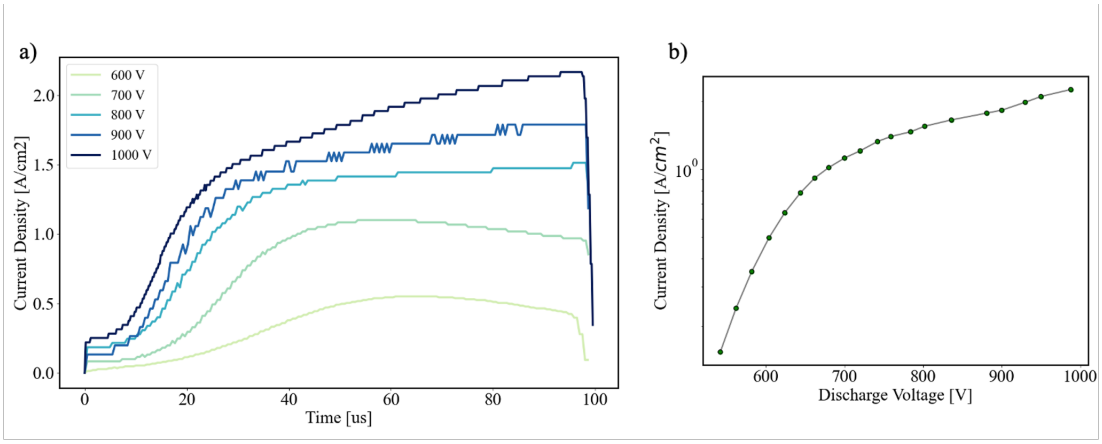

Figure 4.5: a) The temporal evolution of the experimentally acquired discharge currents as a function of the applied voltage. b) The voltage-current characteristic curve for the Cu HiPIMS discharge.

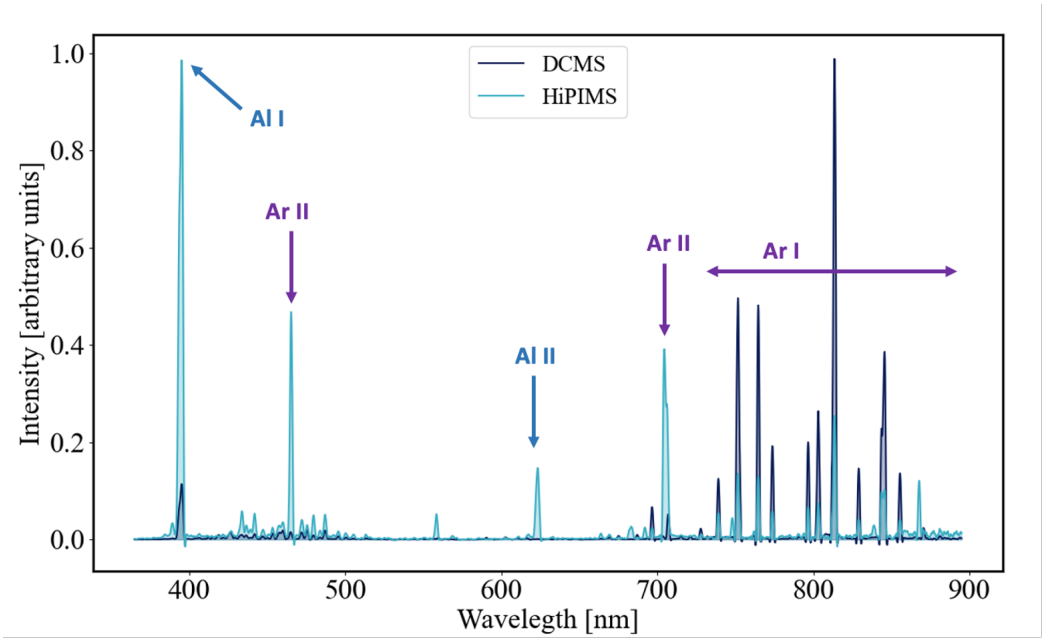

Figure 4.6: OES of the Al plasma in DCMS and HiPIMS under comparable working conditions. Al I and Ar I refers to atomic Al and Ar, while Al II and Ar II refer to Al and Ar singly ionized. The peaks have been attributed according to [89].

As expected, the OES in Figure 4.6 show significant differences in plasma composition between the DCMS and HiPIMS. The DC plasma is predominantly composed of Ar

species, with only one peak attributed to atomic Al. In HiPIMS, the intensity of the emission lines from Ar is strongly reduced, while the signal from Al species is increased.

Morphological Characterization

In Figures 4.7 and 4.8, SEM planar and cross-sectional views of Al samples realized in DCMS, HiPIMS and HiPIMS with delayed bias are shown.

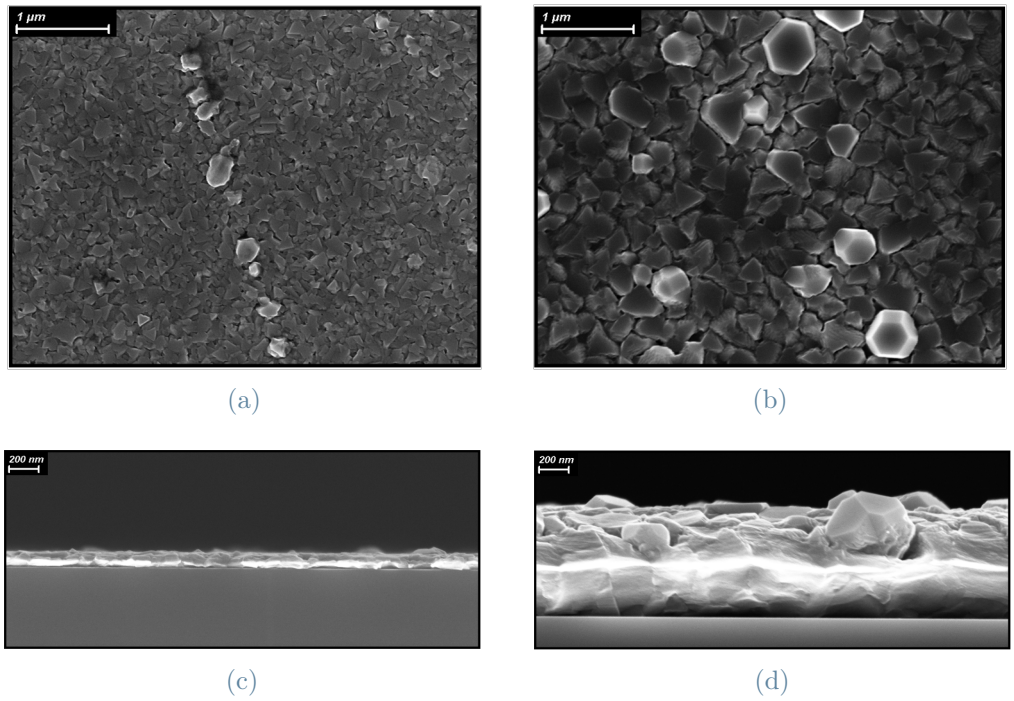

Figure 4.7: SEM images of DC-sputtered Al samples. (a) planar and (c) cross-section of a 100 nm thick film, (b) planar and (d) cross-section of a 800 nm thick film.

As far as DCMS samples are concerned, the microstructure changes with film thickness, transitioning from small and dense grains (see Figures 4.7a) and 4.7c) to larger and coarser ones (see Figures 4.7b and 4.7d). Moreover, the formation of some protrusions, known as hillocks, can be observed. Their dimensions increase with increasing film thickness, in agreement with what is described in the literature [94]. Both the coarse grain structure and the presence of hillocks worsen the surface uniformity of the film.

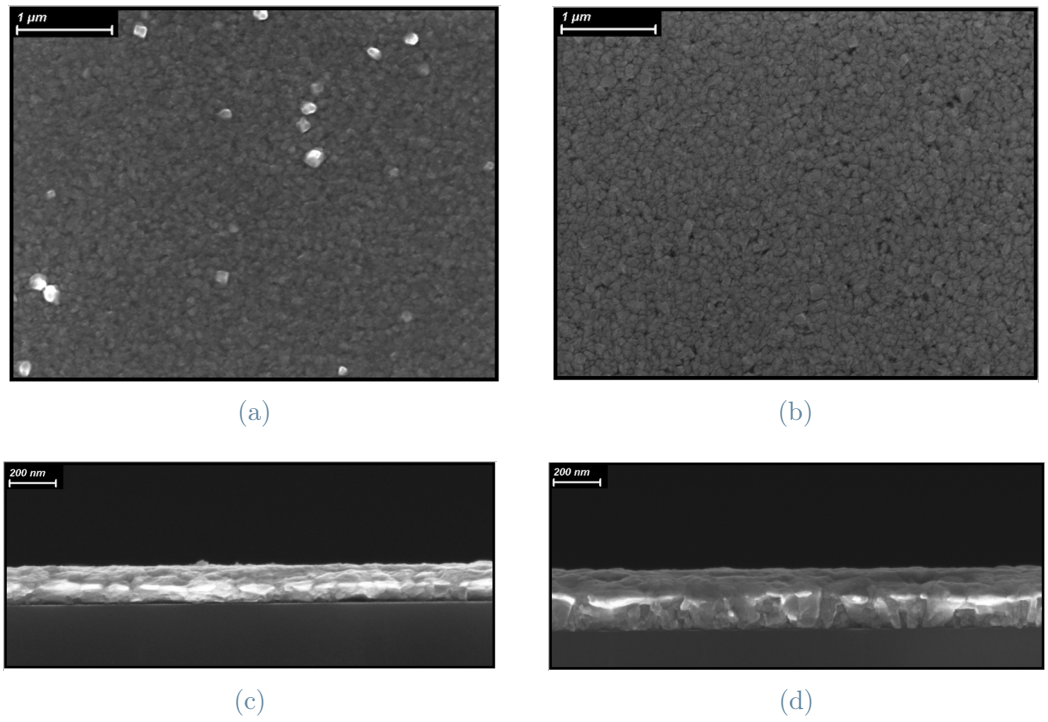

Figure 4.8: SEM images of Al samples deposited via HiPIMS ((a) and (c)) and biased HiPIMS ((b) and (d)). (a) Planar and (c) cross-section of a 160 nm thick film. (b) Planar and (d) cross-section of a 247 nm thick film

In the high energy case of HiPIMS (Figure 4.8a) and c)), it is possible to notice that the film exhibits a compact microstructure, with small and fine grains and a smooth surface even at higher thicknesses. Furthermore, hillocks appear to be reduced in number and dimensions. To further increase the species' energy and flux towards the film, a third approach was employed, applying a delayed bias. The bias was applied 60 μs after the main pulse, taking into account the delayed generation of metal ions to maximize their acceleration [70]. The delay time was estimated qualitatively by looking at the waveforms. At 60 μs the current density is close to its maximum value, thus it is reasonable to think that a high fraction of metal species are present. The biased HiPIMS had the effect of completely suppressing hillock formation (see Figure 4.8b) and d)) but some voids appear at the surface of the film. In the three deposition conditions, Al films show a ductile behavior to fracture, as can be seen by the cross-sections.

Mechanical Characterization

The stress evolution of Al films, depicted in Figure 4.9, shows a more complex behavior compared to Cu, continuously transitioning between compressive and tensile states. Both DCMS and HiPIMS sputtered samples display stresses of comparable magnitude but with

different trends. In particular, films deposited in DC show an almost CTC behavior, and stress relaxation occurs with increasing thickness. On the other hand, the average stresses associated with HiPIMS shift from an initial tensile stress to a compressive one, with no apparent stress relaxation. It seems like the CTC transition is shifted toward lower thicknesses. Introducing the bias, the full CTC transition is visible again but shifted towards higher thicknesses with respect to the DC case and with higher compressive stresses at low thicknesses: at around 100 nm there is one order of magnitude difference between DCMS and HiPIMS sputtered films.

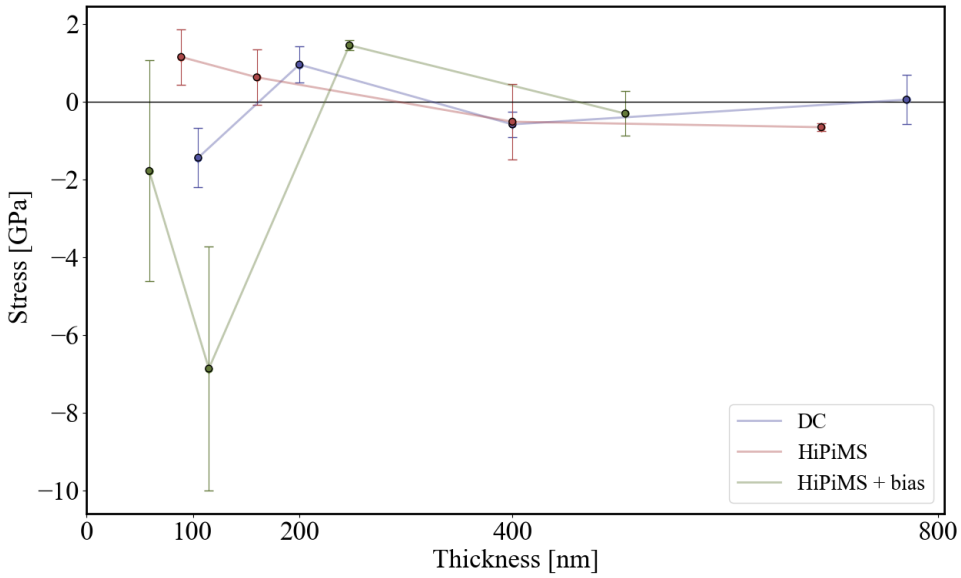

Figure 4.9: Average residual stress as a function of thickness for Al films deposited in DCMS (blue line), HiPIMS (red line), biased HiPIMS (green line).

Discussion of the results

Concerning DC-sputtered films, both the microstructure [95] and the stress evolution [77] as a function of thickness are characteristic of Zone-T or high mobility materials. Indeed, the homologous temperature results $T_h = 0.31$, considering the substrate at room temperature and $T_m = 933\ K$. Hillocks are reported to be a mechanism of compressive stress relaxation [94, 96]. They form due to the diffusion of atoms to the grain boundary triple points [94] and grow as a consequence of the plastic deformation of the film [94, 96]. Thus, their presence may explain the relatively low compressive stresses (- 1.5 GPa at maximum) and the almost stress-free sample at the higher thickness of 800 nm, where hillocks are larger. The denser and finer microstructure exhibited by films deposited in

HiPIMS is a consequence of the densification process, promoted by the higher ion energy and the higher fraction of ionized target atoms with respect to DCMS [97]. The reduction of hillocks in this regime might be attributed to the higher adatom mobility and enhanced etching by Ar ions. This hypothesis is confirmed by the suppression of hillocks exploiting the more energetic deposition of biased HiPIMS. The higher adatom mobility is witnessed by the shift of the CTC transition towards higher thicknesses [73]. The high values of compressive stress might be attributed to defect formation, atomic peening and grain boundary densification, associated with energetic depositions, but also to the absence of hillocks.

4.2. Production and characterization of carbon foams via PLD

4.2.1. Carbon foams deposited via ns-PLD and fs-PLD

Deposition Parameters and Plasma Characteristics

In the case of ns-PLD, depositions were performed using a circular pyrolitic graphite target, ablated by a laser with a wavelength of 532 nm. The energy of the laser was maintained fixed at 500 mJ for all depositions. The target moves vertically while rotating at 359 $^{\circ}/s$. As a consequence, the laser ablates the target following a spiral path. This enables optimal exploitation of the graphite surface. Si substrates are fixed on a rotating holder (rotational speed = 11 rpm) to assure better uniformity during the deposition. The substrate to target distance was maintained fixed at 70 mm. The chamber was evacuated to a base pressure lower than 10^{-3} $mbar$ and then filled with Ar. Samples were produced according to the deposition conditions reported in Table 4.4.

	Pressure [Pa]	Ar Flux [sccm]	Deposition time [min]
Sample 1	200	20	10
Sample 2	100	20	10
Sample 3	5	-	6

Table 4.4: ns-PLD deposition parameters. At high pressures (200 Pa and 100 Pa), the Ar flow rate was set to 20 $sccm$ and the pressure was manually adjusted during the deposition. At the low pressure of 5 Pa, a feedback mechanism was exploited to automatically change the gas flow rate to maintain the pressure fixed.

Concerning fs-PLD, one reference sample has been deposited, according to the following parameters. A circular pyrolitic graphite target was ablated by a laser with a wavelength of 800 nm. The energy of the laser was measured to be 3.8 mJ on target. The target moves vertically while rotating at 3.2 $^{\circ}/s$ to enable optimal exploitation of the graphite surface. Si substrates are fixed on a rotating holder to assure better uniformity during the deposition. The substrate to target distance was maintained fixed at 3.8 cm. The chamber was evacuated to a base pressure lower than 10^{-3} $mbar$ and then filled with Ar at a pressure of 300 Ps.

Morphological Characterization

SEM and EDX analyses have been performed to qualitatively investigate the characteristics of the deposited foams.

From the SEM images in Figure 4.10, it is possible to appreciate the different morphology obtained in ns-PLD with varying Ar pressure.

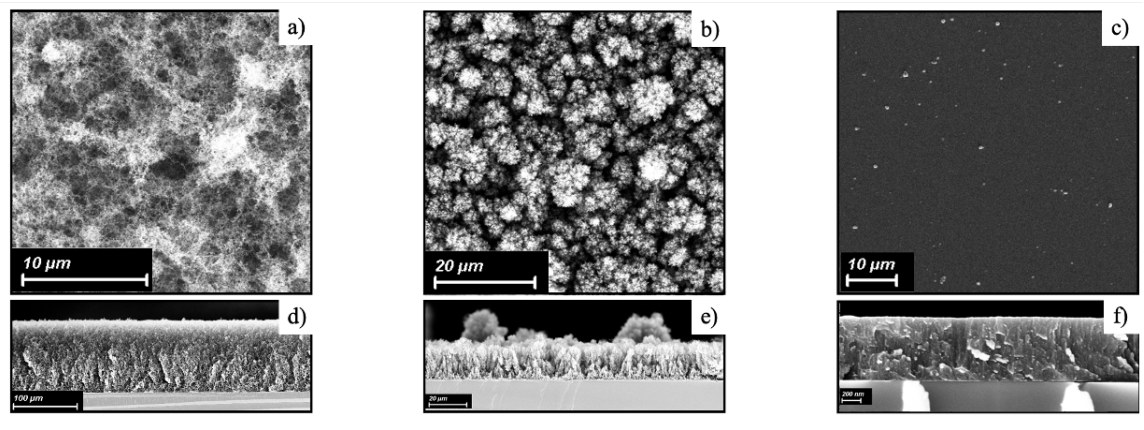

Figure 4.10: SEM planar and cross-sectional views of the ns-PLD deposited carbon samples. a) Sample 1: Carbon-Foam obtained with 200 Pa Ar pressure, b) Sample 2: Tree-Like-Carbon obtained at 100 Pa Ar pressure, c) Sample 3: Compact-Carbon obtained at 5 Pa Ar pressure.

At 200 Pa a typical sponge-like porous structure is obtained. Decreasing the pressure down to 100 Pa aggregates result to be more compact, acquiring a tree-like shape. At 5 Pa a compact carbon film is obtained. Accordingly, the mass density increases with decreasing pressure. From EDX measurement it resulted that the Carbon-Foam, the Tree-Like-Carbon and the Compact-Carbon are characterized by a density of 6 $g/cm3$, 26 $g/cm3$ and 2000 $g/cm3$, respectively.

In Figure 4.11, the SEM images of the fs-PLD sample are reported. It is possible to

notice a more irregular morphology, with the presence of large aggregates. From EDX measurements, the foam density resulted 7.5 mg/cm^3. Therefore, despite the higher pressure (300 Pa vs 200 Pa), the fs-PLD deposited foam is denser than the one obtained via ns-PLD. These features are typical of fs-PLD due to the larger aggregates directly ablated from the target.

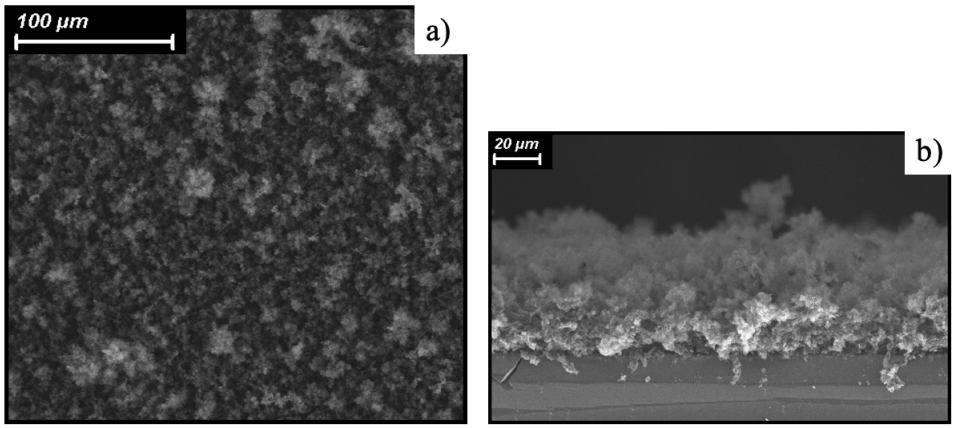

Figure 4.11: SEM a) planar and b) cross-sectional views of the fs-PLD deposited carbon foam.

5 | Development of a strategy to realize free-standing films

In this Chapter, the realization of free-standing films through a fishing procedureIt can be subdivided into four steps, as shown on the left of Figure 5.1: realization of the sacrificial layer on the substrate (discussed in Section 5.1), deposition of the film (discussed in Section 5.2), detachment of the film from the substrate and its fishing with the target holder (both described in Section 5.3). In Section 5.4, in view of the realization of DLT, a preliminary investigation of carbon foams deposition on the obtained free-standing films is addressed. Finally, Section 5.5 is devoted to a discussion of the results.

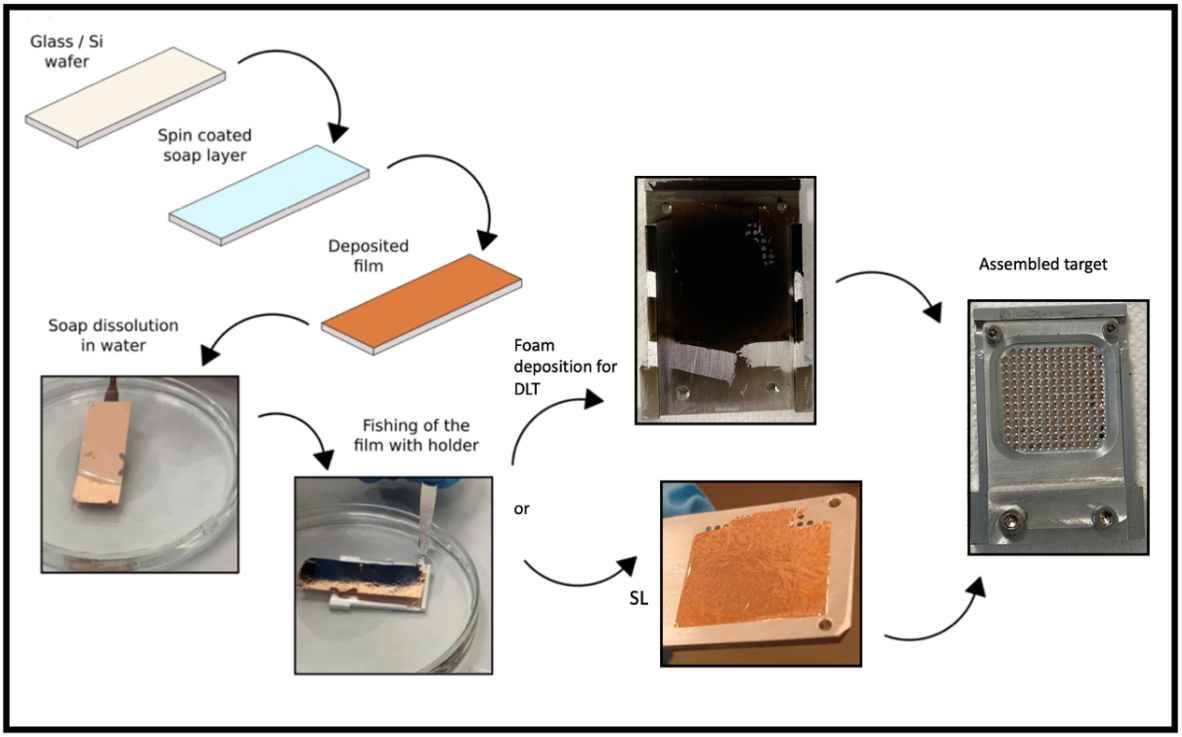

Figure 5.1: Schematic representation of target production. On the left, the fishing procedure is represented. On the right, the obtainment of SL or DLT is shown.

5.1. Realization of the sacrificial layer

The first step of the fishing procedure is to realize the sacrificial layer. The material employed as parting agent should fulfill certain requirements to effectively serve this purpose. For instance, it should be soluble in an easily available and non-toxic solvent, like water. Moreover, it must be compatible with the employed deposition technique and should not affect the properties of the film. In the literature, different kinds of sacrificial layers have been employed. Thermally deposited NaCl has been used as a parting agent to realize ultra-thin DLC [98] via Filtered Cathodic Vacuum Arc (FCVA) and gold thin films via DC sputtering [66]. In both cases, the NaCl morphology was transferred to the film. In another work, a pure betaine-sucrose solution was exploited as sacrificial layer to realize C-foils via sublimation induced by resistive heating [99]. In this case, the covering process must be carried out in controlled humidity conditions to avoid re-crystallization of sucrose, which would prevent the subsequent detachment of the film [100].

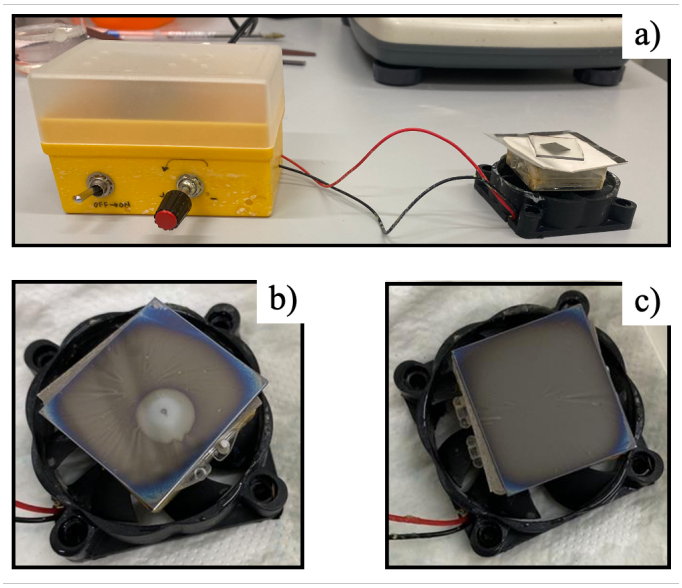

Figure 5.2: a) Spin-coating realized exploiting computer vents. b) Si substrate covered with a layer of soap after one spin-coating of 1 *min*. c) Si substrate covered by a soap layer after the second spin-coating.

In the context of this thesis, soap was exploited as a sacrificial layer for the fabrication of Cu and Al free-standing films, deposited via DCMS and HiPIMS. Dish soap was chosen as the parting agent because of its affordability, it is easily available and does not require particular operating conditions. The process consists in the coverage of the Si substrate with a water solution containing a specific percentage of soap, followed by spin-coating

(see Figure 5.2a)) for a duration of 1 *min*. This process is repeated one more time to assure a better coverage of the substrate and better uniformity (see Figure 5.2b) and c)). Water dries quickly after the spin-coating is completed. It is worth noticing that the spin-coating device is home-made, realized with computer vents. Thus, it is not possible to have a completely optimized process. This technique offers several advantages, including the short preparation time required for each sample and the possibility of covering large areas, in the order of tens of cm^2. However, determining the optimal soap concentration is a critical aspect. It turned out to depend on several factors, such as the type of substrate (e.g. Si or glass), the deposited material (Cu or Al in this case), and the deposition conditions, as described in Section 5.2.1.

5.2. Deposition of the Cu and Al films via Magnetron Sputtering on the sacrificial layer

Cu and Al films were deposited according to the conditions and parameters reported in the previous Chapter. Those preliminary depositions were exploited to estimate the deposition rates. The deposition rate of Cu in DCMS was around 65 nm/min and it decreased in HiPIMS down to 21 nm/min. The deposition rates for Al in DCMS, HiPIMS and biased HiPIMS were 35 nm/min, 10 nm/min and 7 nm/min, respectively. Several trial depositions were performed to assess the optimal concentration of soap in solution and its effect on the film properties. To do so, representative thicknesses have been selected to investigate relatively thin, intermediate, and thick samples. In particular, the estimated deposition rates were exploited to realize films in the order of 100 nm, 400 nm and 800 nm, for both materials and for each deposition conditions considered.

5.2.1. Assessment of the concentration of soap

The required concentration of soap for the spin-coating water solution was investigated considering different combinations of substrates and deposition regimes. Cu and Al samples have been deposited in DCMS, HiPIMS and biased HiPIMS (in the case of Al), on Si or glass substrates covered with increasing amounts of soap. In Section 4.1.1, it was observed that Cu exhibits a poor adhesion on Si substrates. Consequently, the introduction of the soap layer had a detrimental effect, causing the delamination of most of the samples. Better performances were obtained employing glass substrates instead of Si ones. In this case, a concentration of 6% of soap by weight of solvent was sufficient to detach the film from the substrate. On the other hand, Al showed a better adhesion to Si. Indeed, the concentration of soap needed to detach the films was found to be higher.

In particular, with 6% no detachment occurred. Increasing the concentration up to 15%, only small portions of the films were separated from the substrate. With 30% a gradual full detachment of the films was achieved, both for those deposited in DCMS and HiPIMS, but not for the biased case.

5.2.2. The effect of the sacrificial layer on film morphology and stresses

The presence of the parting agent on the substrate alters the adatom-surface interaction [101]. This might potentially impact film growth, consequently affecting its morphology and stress state. To investigate these effects, films deposited on Si substrates covered with different amounts of soap were characterized by SEM and Stoney analysis. Unfortunately, glass substrates, used in the case of Cu, prevented from performing these characterizations. Therefore, the following discussion is based on the results concerning the depositions of the Al films. Looking at the SEM planar views reported in Figure 5.3, it is possible to observe the appearance of some features when the soap layer is present. These have different characteristics depending on the amount of soap, the deposition conditions, and the film thickness.

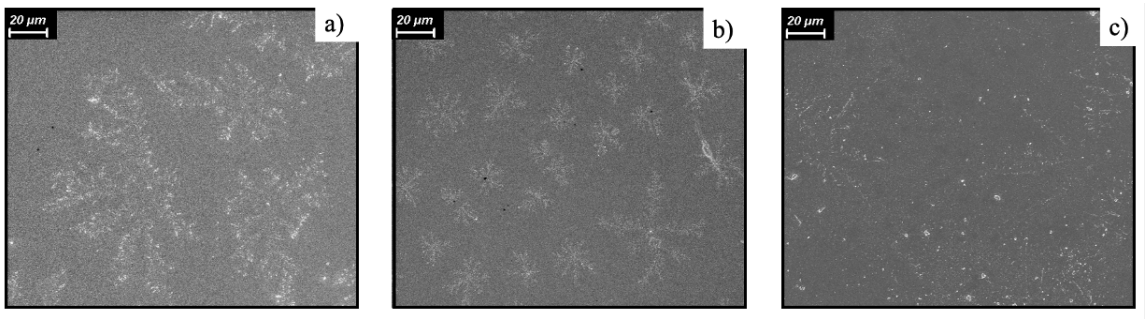

Figure 5.3: SEM planar view showing the formation of fractal-like structures due to the presence of soap. a) DCMS 100 *nm* film on 15% of soap. b) Biased HiPIMS 100 *nm* film on 30% of soap. c) HiPIMS 100 *nm* film on 30% of soap.

Regarding the 100 *nm* thick samples, the following observations can be made. It can be observed that the DCMS deposited samples present fractal-like structures due to the soap presence, as illustrated in Figure 5.3a). These are characterized by a distinct branched structure when the soap concentration is 15%, whereas the branching pattern diminishes at the higher concentration of 30%. Similar considerations can be made for the HiPIMS samples (see Figure 5.3c)). Conversely, in the case of biased HiPIMS (see Figure 5.3b)), the effect of the soap layer is noticeable only at the highest concentration, resulting in

the presence of branched structures but smaller in size compared to the DCMS scenario. As the film thickness increases, the fractal-like characteristics disappear. Specifically, at 400 nm, no observable soap effect is evident for any of the deposited films in DCSM, HiPIMS or biased HiPIMS, as depicted in Figure 5.4. The same holds true for the 800 nm films produced via HiPIMS and biased HiPIMS. Interestingly, the surface of the sample deposited in DCMS appears to be affected by the presence of soap at 30% (see Figure 5.3c). Nevertheless, the influence exerted by the soap layer on the morphology of the film is restricted to only some portions of it. Furthermore, the morphological characteristics described in Chapter 4 are preserved. In the case of DCMS samples, large and coarse grains are present together with the formation of hillocks. A more compact and fine microstructure is observed in the case of HiPIMS and biased HiPIMS, with the suppression of hillock in the latter (see Figure 5.4).

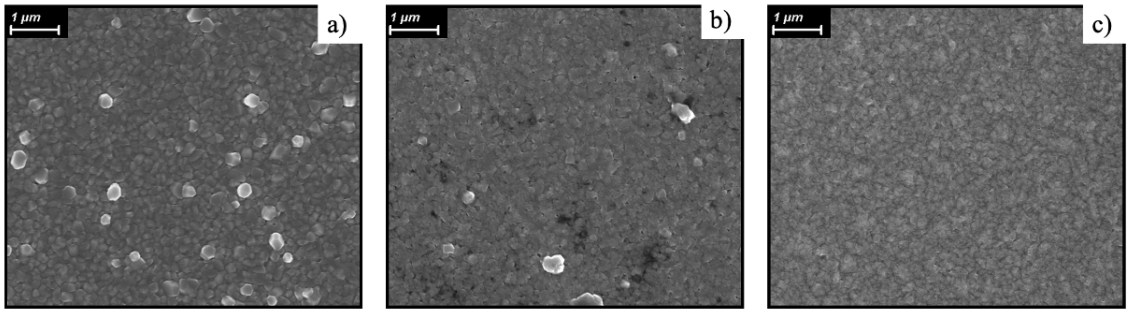

Figure 5.4: SEM planar view showing the surface morphology of 400 nm films on 30% soap layer for different deposition conditions. a) DCMS, b) HiPIMS, c) biased HiPIMS.

Concerning the mechanical characterization, surface curvature measurements have been performed on three nominally identical samples in each of the three deposition conditions for a reference thickness of 400 nm. The stresses were assessed on the naked Si substrates prior to spin-coating and after the deposition of the film on the soap layer. Compared to the findings reported in Chapter 4, the results indicated that the sacrificial layer has no appreciable effect on the average stress state. This is in agreement with the observation that the morphology of the films has not significantly changed.

5.3. Fishing procedure on perforated holders

To separate the film from the substrate, a gradual immersion of the sample in water is required. Detachment begins when the liquid is able to penetrate between the metal and Si (or glass) surfaces. To facilitate this initial stage, the film is intentionally scratched at the borders. Water gradually lifts the metal from the substrate. This procedure works

better with ductile materials (such as Cu or Al). Thanks to its large surface-to-volume ratio, the detached film can float on water under the action of surface tension, which also helps in keeping it flat. Finally, the film is scooped up with the perforated target holder. Thanks to capillary forces, the wet film attaches to the solid portions of the target, while free-standing films are obtained in correspondence of the holes.

The three types of holders employed, each with distinct hole dimensions and/or shapes, are shown in Figure 5.5. The first one (Type I), manufactured by SourceLab company, presents perforations measuring 1 mm in diameter. Another test holder (Type II) was created by cutting metallic grids featuring holes approximately 2 mm in diameter. The third target holder (Type III), is characterized by perforations in the form of elongated stripes, approximately 5 mm wide.

5.3.1. Obtained free-standing films: integrity and defects

As anticipated, Cu films deposited on soap-covered Si wafers delaminated, while more favorable results were obtained using glass slides. Specifically, exploiting DCMS, free-standing films with thicknesses ranging from 50 nm up to 2 μm and areas of several cm^2 were successfully fabricated on Type I target holders, as shown in Figure 5.5e) and f). For the detachment of thicker films, a solution containing 6% of soap by weight of solvent proved to be sufficient. A concentration of 12% was required in the case of thinner 50 nm samples. On the other hand, Cu films deposited using HiPIMS experienced wrinkling and fracturing as soon as water started to penetrate.

Considering Al, free-standing films were successfully obtained on the type II holder. These films had an area of several cm^2 and thicknesses ranging from 50 nm to 800 nm. These results were achieved by exploiting both DCMS and HiPIMS. A solution containing 30% of soap by weight of solvent proved to be sufficient for all the explored thicknesses and in both deposition conditions. Instead, in the case of biased HiPIMS, the films did not detach from the surface.

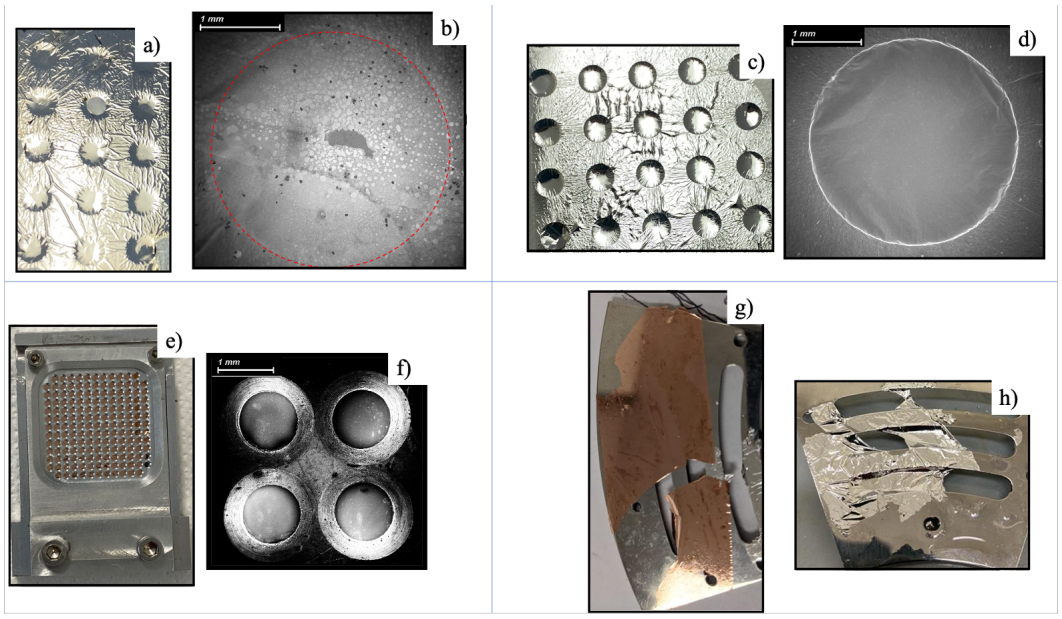

Figure 5.5: Pictures and SEM images representing some of the obtained free-standing films. On the upper-left, a) shows a 100 nm Al free-standing film obtained via DCMS on the type II holder and b) the SEM images of one of its holes where residues of soap are visible. On the upper right c) shows a 50 nm Al free-standing film obtained via HiPIMS on the type II holder and d) the SEM image of one of its holes where some corrugations are present. On the bottom-left e) shows a 200 nm Cu free-standing film obtained via DCMS on the holder of type I and f) a magnification of a set of its holes. On the bottom-right g) shows a 800 nm Cu free-standing film obtained via DCMS on the holder of type III and h) a 100 nm Al free-standing film obtained via HiPIMS on the holder of type III.

To assess the integrity and surface features of the free-standing films, some representative pictures and SEM micrographs are reported above in Figure 5.5. In general, it can be noticed that films with a thickness $\geq$ 200 nm were able to cover the target without breaking (see Figure 5.5e), 5.5f) and 5.5g)). Instead, for lower thicknesses, some of the free-standing films resulted cracked. Moreover, it is possible to observe that thinner films tend to collapse in correspondence with the holes under the action of water surface tension, as shown in Figure 5.5a), 5.5c) and 5.5g) . This effect, which is more evident as the size of the perforation increases, leads to the breakage of the film. As far as small holes are concerned, collapsing is not detrimental as the films remain intact. Additionally, it is reasonable to assume that all free-standings collapse in the same way, thus laser focusing should not be affected by it. Most of the free-standing films appear flat. In certain cases some corrugations are present, as depicted in Figure 5.5d). They originate from the borders of the holes and propagate inwards. Also, some residues of soap are visible (see

Figure 5.5b)).

5.4. Carbon foam deposition via fs-PLD on the free-standing films

To investigate the feasibility of the realization of DLTs, preliminary depositions of Carbon foams via fs-PLD have been performed on some of the obtained free-standing films, according to the parameters reported in Chapter 4. Specifically, the 200 nm Cu film, the 100 nm Al film and the 50 nm Al film have been tested.

All of them could endure the deposition, even if a "membrane effect" could be qualitatively observed. The free-standing films, solicited by foam deposition, vibrate limiting the aggregation of the foam. However, this effect seems to be less relevant with increasing foam thickness.

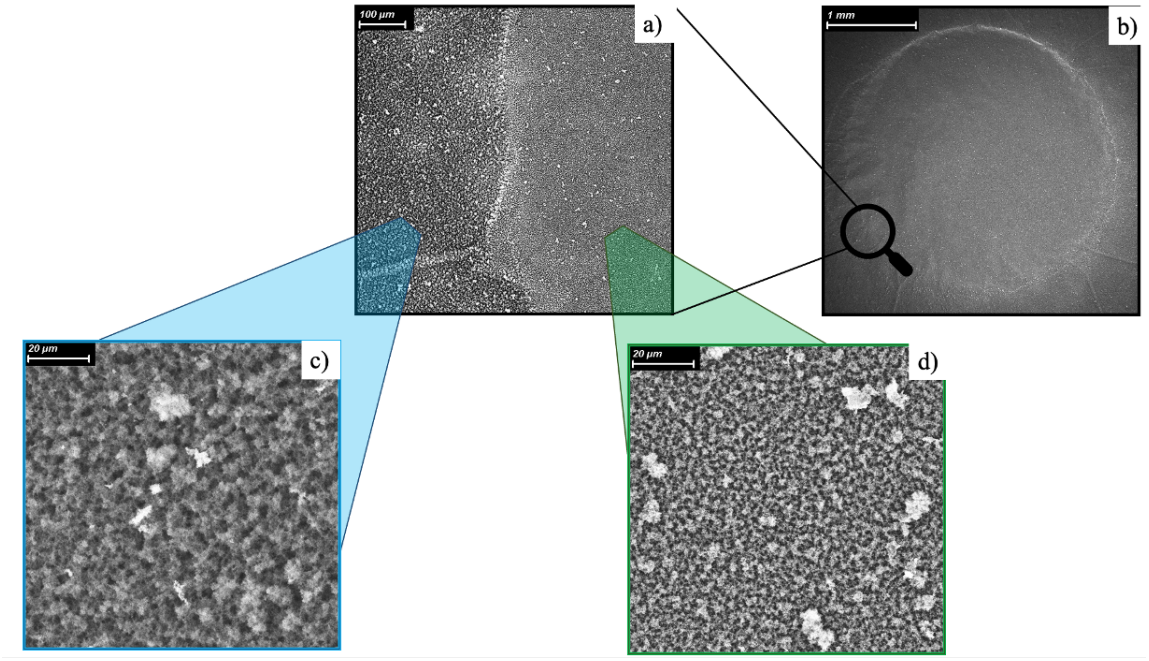

Figure 5.6: SEM images showing the deposition of a thinner foam on the 100 nm Al free-standing film. a) magnification of the boundary between the free-standing film and the solid holder. b) image of the free-standing film on the hole. c) foam on the solid holder. d) foam on the free-standing film.

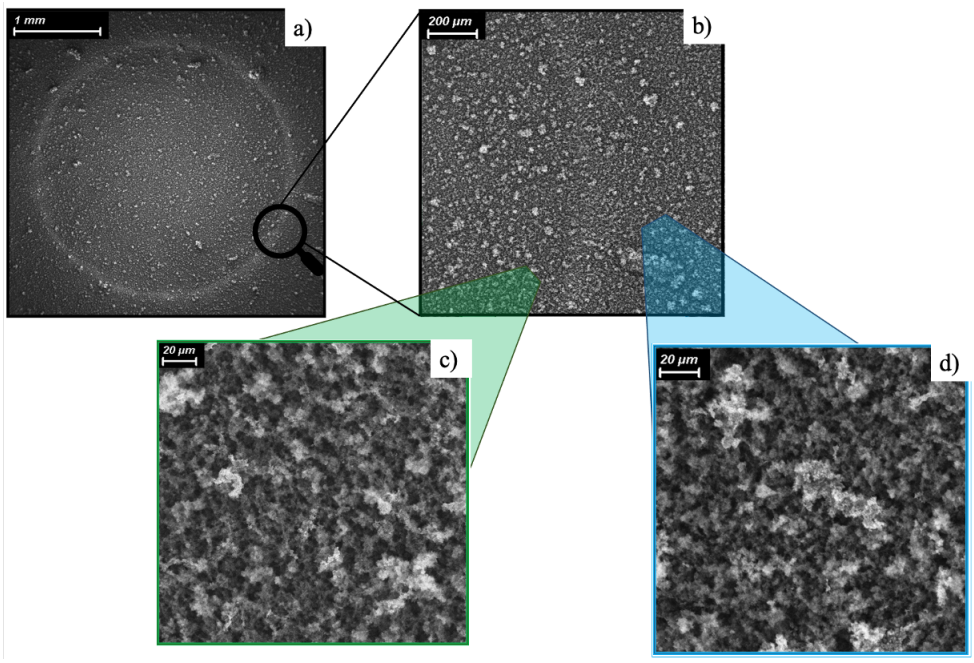

Figure 5.7: SEM images showing the deposition of a thicker foam on the 100 *nm* Al free-standing film. a) Image of the free-standing film on the holder. b) magnification of the boundary between the free-standing film and the solid holder. c) foam on the free-standing film. d) foam on the solid holder.

Figures 5.6 and 5.7 show two 100 *nm* thick Al films, covered by foams of different thicknesses: a thinner foam and a thicker foam, respectively. Notably, the morphology of the thin foam shows discernible differences between the section deposited on the free-standing film (Figure 5.6d)) and the section deposited on the Al covering the solid portion of the holder (Figure 5.6c)). Specifically, the foam aggregates on the free-standing film appear to be smaller in size. In the case of the thicker foam, no appreciable difference can be noticed (see Figure 5.7c) and Figure 5.7d)). These observations are further supported by the comparison between Figure 5.6a) and Figure 5.7b), which present magnified views of the boundary between the free-standing film and the solid region of the holder. A net border appears in the case of the thinner foam (Figure 5.7b)), while the distinction between the two areas is more challenging in the case of the thinner foam (Figure 5.6a)).

5.5. Summary and discussion of the results

In this Chapter, a fishing procedure to realize free-standing films has been presented. Soap is exploited as sacrificial layer and metallic films are deposited via Magnetron Sputtering. It has been explored the feasibility of obtaining a wide range of thicknesses, which is of

interest for the realization of SL targets. Additionally, the mutual compatibility between free-standing films and carbon foam has been investigated to assess the possibility of realizing DLT. Two different metals have been tested, Al and Cu.

A critical summary of the obtained experimental results is provided in the following, highlighting the achieved goals and issues, also in comparison with the previous hole-filling technique described in Chapter 2. The possibility of obtaining free-standing films exploiting a sacrificial layer of soap depends on the combination of deposited material (i.e., Cu or Al), type of substrate (i.e., Si or glass), and deposition regime (i.e., DCMS, HiPIMS, biased HiPIMS). Cu resulted to be a challenging material. It has poor adhesion to Si. Consequently, the interposition of the soap layer had a detrimental effect. All deposited films on Si, either in DCMS or HiPIMS, were delaminated. Better results were obtained by employing glass substrates. In this case, Cu free-standing films have been obtained by exploiting DCMS and a spin-coating solution containing 6% of soap (by weight of solvent). The range of the achievable thicknesses considerably exceeds that reached by the previous free-standing approach. Indeed, thicknesses from 50 nm up to 2 μm were realized, against the 200 $nm - 1200$ nm range. Considering HiPIMS-sputtered Cu films instead, they crumbled as soon as they were put in contact with water. This outcome highlights the interplay between morphology and stresses. Indeed, DCMS and HiPIMS-sputtered Cu films are characterized by the same grain structure but different stress states, mainly tensile and mainly compressive, respectively. Films realized via DCMS revealed tensile stresses, while those obtained via HiPIMS were subjected to compressive ones. Conversely, Al films provided greater flexibility in terms of deposition conditions. Free-standing films were obtained by exploiting either DCMS or HiPIMS, covering the Si substrates with a spin-coating solution containing 30% of soap. A higher concentration of soap (with respect to the case of Cu) is needed to overcome the strong adhesion of Al to Si. Film thicknesses in the range of 50 $nm - 800$ nm were achieved. The stress state of Al films in this thickness interval can be either tensile or compressive. This observation further corroborates the hypothesis of the interplay between microstructure and stress state. Considering Al films deposited via biased HiPIMS, no detachment from the substrate occurred. A possible explanation can be given considering the energy of the depositing species. With the application of a bias, ions are accelerated at higher energies when compared to conventional HiPIMS. It is reasonable to assume that part of them is energetic enough to etch the soap layer and stick to the substrate, inhibiting detachment. Another important result should be highlighted. Since in the hole-filling technique, each perforation must be filled individually, this is a quite time-consuming procedure that enables the realization of only small-area free-standing films. Conversely, the fishing procedure is

faster, and large-area free-standing films can be obtained if the proper thickness is chosen. The bottleneck of the procedure is the need for several preliminary depositions to guess the optimal concentration of soap. The fished films showed better performances also considering the production of DLTs. In the previous thesis works employing the hole-filling technique, a "vibrating membrane" effect was highlighted. During the foam deposition via PLD, thin films vibrate since they are subjected to mechanical solicitations. This caused coverage reduction along the radial direction, for small film thicknesses. The "vibrating membrane" effect is qualitatively observed also with the fishing procedure but, the film looks uniformly covered, even considering the low thicknesses 100 nm and 50 nm. Additionally, it was noted that increasing foam thickness, this effect is suppressed.

6 | Production of carbon foams as ablation layer in ICF targets and experimental campaign

As mentioned in Chapter 2, part of the thesis work was dedicated to the production of carbon foam targets for experiments of relevance in the field of ICF. In particular, according to the motivations presented in Sections 2.2 and 2.3, PLD-deposited carbon nanofoams might be of interest as ablation layer in targets for direct-drive ICF. As highlighted in Chapters 3 and 4, PLD is a versatile technique that enables to act on several parameters to tailor the properties of the deposited materials. The deposition conditions in ns-PLD and the reference samples for the production of foams have already been discussed in Section 4.2. In this Chapter, the main focus is devoted to the realization of the complete targets, highlighting the critical aspects and assessing the feasibility of the use of PLD (Section 6.1). The obtained targets have also been tested in an experimental campaign conducted at the ABC laser facility in ENEA, Frascati, described in Section 6.2. Section 6.3 is dedicated to an overall discussion of the results obtained in this Chapter.

6.1. Production of carbon nanostructured targets

The lasers employed in ICF are characterized by intensities in the order of $\geq 10^{14}\ W/cm^2$ and pulses in the order of ns. Simulations demonstrated that with these laser parameters, foams must have a thickness of hundreds of μm, corresponding to a mass-thickness up to thousands of mg/m^2 (for a foam having density in the order of tens of mg/cm^3), to enable proper laser energy absorption and conversion into implosion energy [68]. Foams with this characteristic have never been deposited at NanoLab. The aim of this part of the thesis work was to assess the feasibility of depositing high mass-thickness foams on different types of substrates that could have been employed in the foreseen experimental campaign (see Section 6.2).

Dealing with PLD-deposited carbon foams, there is a relevant aspect that must be taken

into account. As all PVD techniques, also PLD relies on the growth of the coating on a substrate. Due to their state of aggregation and growth dynamics (see Chapter 3), the manipulation of carbon foam samples is quite delicate, and they can not be separated from the substrate. Therefore, the most effective solution is to conduct the deposition directly on a substrate attached to the holder. Thus, a proper target design is required, and its compatibility with the deposition technique and conditions must be assessed.

6.1.1. Substrates and Holders

In the context of the thesis work, different target configurations have been realized, considering the possible will of investigating plasma expansion and ablation loading.

In particular, thin free-standing films can be exploited as substrates aiming at investigating plasma expansion and the velocity of shockwave propagation through optical diagnostics. The employed substrate should interfere as less as possible during the interaction. Two substrate-holder pairs have been tested. One is represented in Figure 6.1a). The substrate is a thin plastic (CH) foil of 100 nm in thickness, bound to a thin Al frame, mounted on a glass stick. The small thickness of the CH foil should not have a detrimental effect on plasma evolution. Additionally, thanks to the low-Z, X-ray emission is limited, thus it should not affect too much the possibility of obtaining information on plasma emission. On the other hand, two critical aspects might arise. It can not be given for granted that such a thin plastic foil can endure the PLD deposition. Additionally, despite being thin, the Al frame may obscure the view of the optical diagnostics devoted to the imaging of plasma expansion. The second substrate-holder pair was fabricated on purpose. The plastic holder was produced via 3D printing. The vertical stick ends with a C-shaped head. The C aperture measures few mm. The substrate was cut from thin Al foils measuring 1 μm in thickness and attached to the borders of the C-shaped head, shown in Figure 6.1d). The C-aperture should not obstacle the line of sight of the optical cameras and the thicker Al foil should be able to endure PLD conditions. However, these holders have been manually assembled, consequently, the Al foil is not perfectly flat, showing corrugations and being, in some cases, not well adherent to the plastic frame.

Concerning the measurement of the ablation loading, thick bulk substrates are used. As a consequence of the shockwave propagation, a crater is dug in the solid and its volume is directly correlated to the laser-ablated loading efficiency. For this purpose, commercially available Al disks with a thickness of 6 mm have been chosen as substrates. Al is a ductile material, therefore the crater should be able to fully develop inside the disk without breaking it.

In Figure 6.1b) the employed substrates are shown, arranged on the target holder for the deposition.

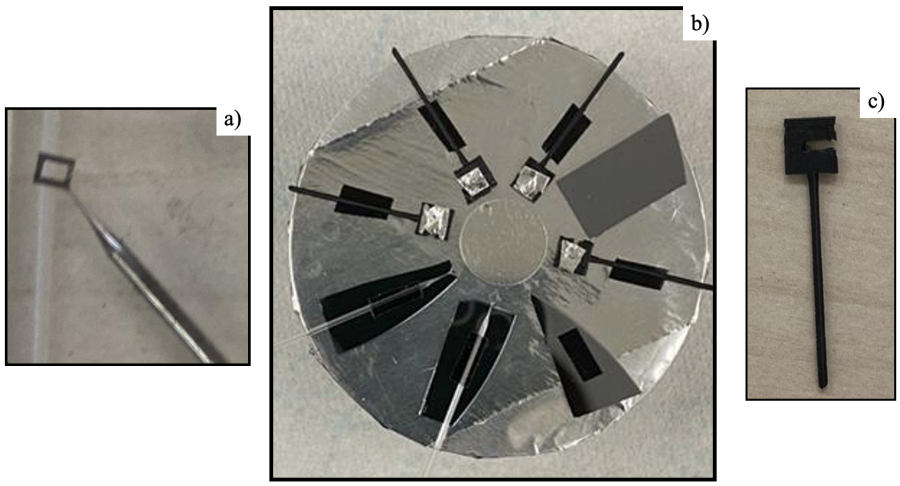

Figure 6.1: a) Glass stick holder with the thin CH substrate. b) bulk Al disk, at the center, glass stick and C-shaped holder arranged for the deposition. c) C-shaped holder before the attachment of the Al foil.

6.1.2. Depositions of nanostructured carbon films

Carbon nanostructure films depositions were performed according to the parameters reported in Section 4.2, varying the deposition time. Therefore, the compatibility of the realized holders with different deposition conditions in ns-PLD and different carbon densities and thicknesses has been explored. Samples of C-Foam (CF), C-Tree-Like (CT), and C-compact (CC)spanning a wide range of mass thicknesses, from around 130 mg/m^2 up to around 1600 mg/m^2 have been realized.

During PLD deposition, substrates are subjected to mechanical solicitations. Due to these solicitations, thin films tend to vibrate and this might have a detrimental effect on their integrity, especially if the deposition of thick foams or CC are considered. Thin plastic substrates could endure all CF depositions, even the longer one of 2 hours leading to the thicker foam of 1600 mg/m^2 (see Figure 6.3e)). Additionally, a uniform coverage is evident Conversely, the growth of compact carbon lead to the breakage of the substrates, even in the case of the thinner sample. Concerning C-shaped holders, they have been able to withstand the depositions of C-Foam, C-Tree-Like, and C-compact over the whole range of mass thicknesses. An example of obtained C-Foam target is shown in Figures 6.2b) and c). However, the growth of compact carbon caused wrinkling of the Al substrate, as visible in Figure 6.2d). Similar considerations can be made for the bulk Al disk substrates. No

issues arose when C-Foam and C-Tree-Like were considered (see Figure 6.3c)), while some of the C-compact samples resulted delaminated, as demonstrated in Figure 6.3, especially with increasing thickness.

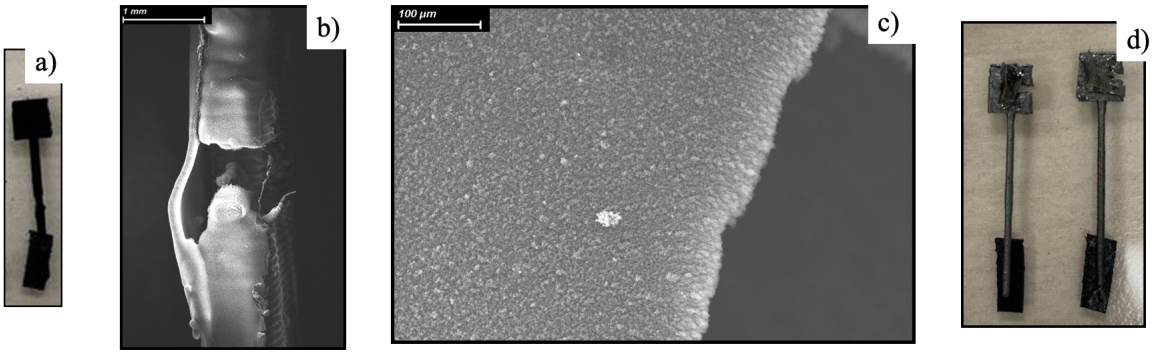

Figure 6.2: Targets realized on the C-shaped holders. a) shows a C-Foam target of 800 mg/m^2 in mass thickness. b) and c) are its SEM cross-sectional and planar view, respectively. d) shows two C-compact targets: wrinkling is evident for the one on the left.

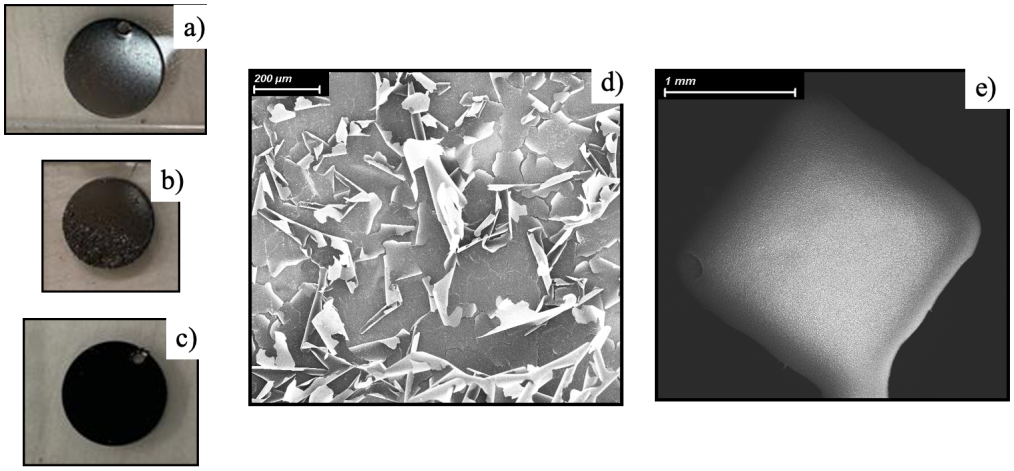

Figure 6.3: Targets realized on bulk Al substrates. a) and b) show C-compact samples realized under the same conditions, a) is intact while a portion of b) is delaminated. A magnification of the damaged portion is shown in d). c) shows a Tree-Like sample. e) shows the integer uniformly covered CH thin substrate after deposition of a 1600 mg/m^2 foam.

A possible explanation for these experimental outcomes is the following. In the case of foam depositions, both C-Foam and C-Tree-Like, the high pressures (200 Pa and 50 Pa, respectively) slow down the aggregates, which arrive gently on the substrate, according

to the snowfall-like model illustrated in Chapter 2. Probably, the lower pressure of 5 Pa enables the ablated species to reach the substrate with relatively high energy, inducing stresses in the carbon film and, consequently in the thin substrates.

6.2. Experimental Campaign

Part of the produced targets was employed in an experimental campaign conducted at the ABC laser facility, described in Section 6.2.1. The aims of the experiment and the selected targets are reported in Section 6.2.2. Section 6.2.3 is devoted to a preliminary presentation of the experimental observation.

6.2.1. ABC Laser Facility

ABC is a laser facility hosted in the research center ENEA, Frascati. It is devoted to laser-matter interaction experiments, relevant in the field of ICF. A schematic representation of the facility is shown in Figure 6.4.

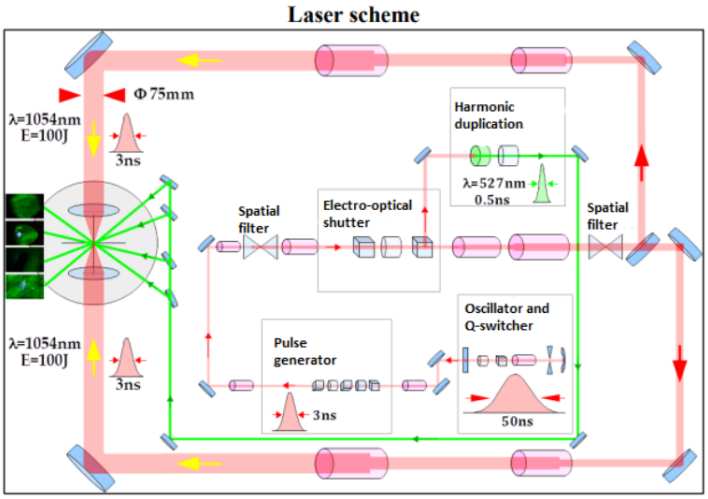

Figure 6.4: ABC laser scheme taken from [68].

A Nd-glass laser can deliver two synchronized counter-propagating main beams, characterized by the following parameters [102].

- Maximum energy delivered: 100 J
- Wavelength: 1.054 μm
- Pulse duration: $0.8 - 3$ ns

- Pulse raising time: $0.5 - 1.5\ ns$
- Spectral range: $0.15\ THz$
- Maximum intensity: $10^{15}\ W/cm^2$

An additional beam can be extracted at the pre-amplification stage, from one of the two lines. Its frequency is doubled (Second Harmonic Generation process), leading to a wavelength of $0.527\ \mu m$ and is exploited for diagnostic purposes. The beams are directed towards a deposition chamber, equipped with several diagnostics. Among the available ones, it is worth mentioning those employed during the experimental campaign. Optical diagnostics such as visible shadowgraphy, Schlieren shadowgraphy, visible interferometry and Streak cameras, can be exploited to investigate different aspects of plasma expansion. Visible spectroscopy, Time of Flight (ToF) spectroscopy performed with diamond detectors and Faraday Cups, diodes for X-rays, and SLIX (see Section 6.2.3) are used to retrieve information on plasma emission. Photo-diodes are used to measure the intensity of transmitted and reflected laser light, to evaluate the absorption efficiency of the target.

6.2.2. Aim of the experiment

The aim of the experimental campaign was to practically investigate the behavior of carbon foams in ICF relevant conditions. Indeed, while their interaction with lasers having relativistic intensities has been extensively studied in the field of laser-driven ion sources, their irradiation in ICF conditions (i.e., higher power, lower intensity, longer pulses) is still an unexplored topic. simulation results showed a slower shockwave propagation and an increased ablation loading with respect to the case of the homogeneous material. Additionally, a high absorption efficiency was found. These can be consequences of the homogenization process, well known for plastic foams (see Section 2.2.3). The homogenization time depends on both pore size and foam density. Therefore, C-Foam (CC) and C-Tree-Like (CT) targets have been exploited to investigate the effect of different morphologies and densities. C-compact (CC) was used as the homogeneous benchmark, while bare Al foils and disks as reference samples. To allow for a comparison among targets featuring several different characteristics (e.g., morphology, density, thickness), three reference mass thicknesses have been selected, in the order of 400 mg/m^2, 800 mg/m^2 and 1600 mg/m^2. In Table 6.1 the employed targets are reported.

Shoot	Type of material	Substrate	Type of holder	Thickness [μm]	Density [mg/cm^3]	Mass thickness [mg/m^2]
6345	C-Foam (CF)	1 μm Al	C-Holder	267	6	1602
6350	C-Foam (CF)	1 μm Al	C-Holder	150	6	900
6354	C-Foam (CF)	100 nm CH	Glass stick	267	6	1602
6358	C-Tree-Like (CT)	1 μm Al	C-Holder	60	26	1560
6362	C-Tree-Like (CT)	1 μm Al	C-Holder	30	26	780
6364	C-Compact (CC)	1 μm Al	C-Holder	0.8	2000	1600
6368	Al bulk	Al bulk	Al bulk	1300	2700	
6372	μm Al	1 μm Al	C-Holder	1	2700	
6376	C-Tree-Like (CT)	Al bulk	Al bulk	60	26	1560
6378	C-Foam (CF)	Al bulk	Al bulk	267	6	1602
6382	C-Tree-Like (CT)	1 μm Al	C-Holder (UP)	60	26	1560
6384	C-Tree-Like (CT)	Al bulk	Al bulk	30	26	780

Table 6.1: Targets employed in the experimental campaign with the respective shot number. UP means that the C-shaped aperture looks upward, while in the other cases, it is in the lateral position.

These targets have been irradiate with a laser having an intensity of 10^{14} W/cm^2, an average energy of 40 J, a pulse duration of 3 ns (FWHM) and a spot diameter of 100 μm. The critical mass density corresponding to a wavelength of 1054 μm is 3.3 mg/cm^3, thus all targets are over-critical.

6.2.3. First experimental observations

The analysis of the data obtained from the experimental campaign is still in progress. This Section is devoted to a qualitative discussion of the preliminary observations, focusing the attention on the shadowgraphs, schlieren and SLIX images, which I directly contributed to examine.

Shadowgraphy and schlieren are two complementary optical techniques based on the deflection of the light of a probing beam when gradients in the index of refraction are encountered [103, 104]. A laser-produced plasma tends to expand toward the vacuum and its density decreases moving far from the target. The density gradient causes a gradient in the index of refraction of the plasma, as they are connected according to the following relation:

$$n = \sqrt{1 - n_e/n_c} \tag{6.1}$$

being n the index of refraction, n_e the electron plasma density and n_c the critical density. In conventional shadowgraphy, the strongly refracted rays are cut and only the un-deviated ones are imaged. Therefore, a 2D time integrated snapshot of the plasma is obtained, in which darker regions correspond to a high density plasma. Bright areas can be both due

to the light of the probing beam or plasma auto-emission. Conversely, in the schlieren shadowgraphy an obstacle is used to cut the un-deviated rays while the refracted ones are imaged. Thus the refractive regions are represented as bright areas. Activating the probe beam at different delay times with respect to the main beam, it is possible to get an idea of plasma evolution in time, acquiring images at different instants [104]. SLIX is composed by a set of four stripes, sensible to X-rays, which are emitted by the expanding plasma. After the interaction with the radiation, spots become visible. Their brightness is correlated to the intensity of the X-rays. The stripes can be activated at different time delays, to have an idea of the radiation emission in time.

Considering first the C-shaped targets, shot 6372, performed on the bare Al thin substrate, is taken as a reference. Looking at the schlierens at 2 ns, reported in Figure 6.5, it is possible to observe a greater plasma expansion when a carbon sample is present with respect to the bare Al. Additionally, C-Tree-Like foams show a neat plasma border.

Figure 6.5: Schlierens take at 2ns from the main beam, for the reference Al target, CC, thick CT and thin CT. This diagnostic was not active for the shots on the CF targets.The corresponding shot number is reported for each sample.

From the shadowgraphs at 4 ns shown in Figure 6.6, by comparing the reference shot to those performed on compact carbon, the thicker CT and the thicker CF, it is possible to appreciate the different plasma emission. In particular, a red glow, associated to TPD, is present in the compact and C-Foam samples, while it is absent in the case of bare Al. Also the C-Tree-like does not show any red spot, but this is probably due to the fact that the Al substrate was not perfectly adherent to the holder, thus obscuring the emission. This red glow appears more evident in the thinner C-foam and is also present in the thinner C-Tree-Like.

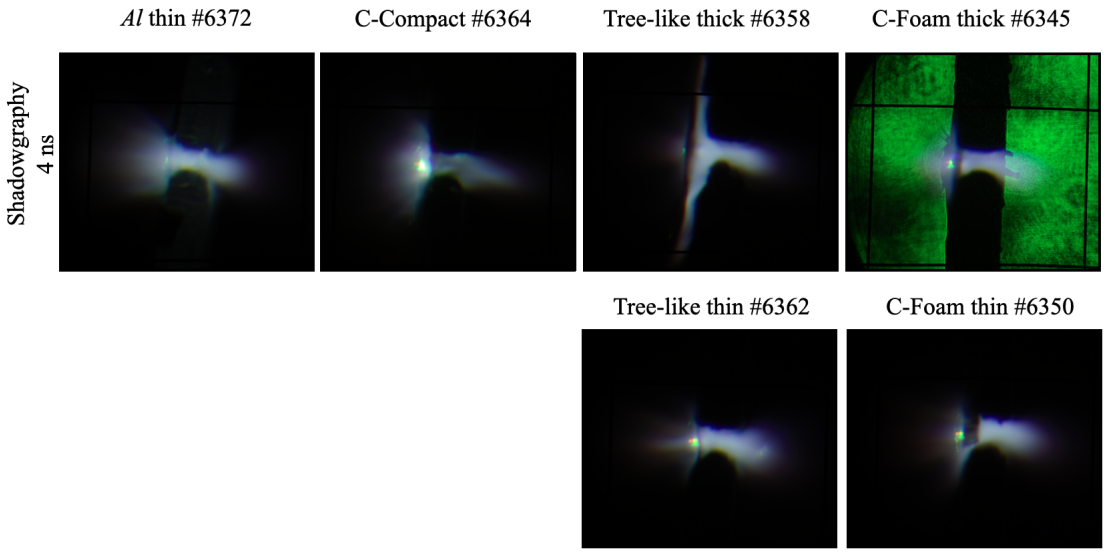

Figure 6.6: Shadographs at $4ns$ from the main beam, for the reference Al target, CC, thick Tree-Like (CT), thick C-Foam (CF), thin Tree-Like (CT) and thin C-Foam targets (CF). The corresponding shot number is reported for each sample.

Moving further by considering the shadowgraphs at 10 ns reported in Figure 6.7, it is possible to observe elongated plasma puffs in front of the target. When Carbon samples are present, these puffs are evident also behind the target, especially in the case of CF and CT. Additionally, the development of a critical-plasma can be observed.

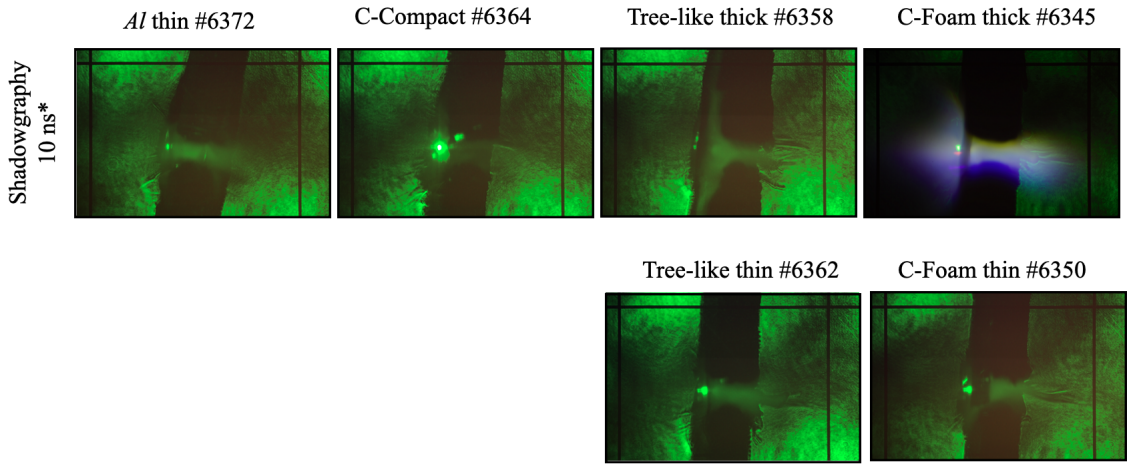

Figure 6.7: Shadowgraphs at $10ns$ from the main beam, for the reference Al target, C-compact (CC), thick Tree-Like (CT), thin Tree-Like (CT) and thin C-Foam (CF) targets. The shadowgraphs of the thick C-Foam (CF) was taken at 12 ns The corresponding shot number is reported for each sample.

In all images discussed so far, a green spot is visible, always in the same position but with different brightness. It is not clear whether it can be associated to a Second Harmonic Generation (SHG) process or to a reflection of the diagnostic beam by the plasma.
Concerning the SLIX in Figure 6.8, X-ray emission appears to be higher and to last longer in time in the case of the thick CF, followed by the thinner one, CC, the thick CT, the thin CT. Bare Al shows the shortest duration. The thin Tree-Like seems to have the lower emission intensity.

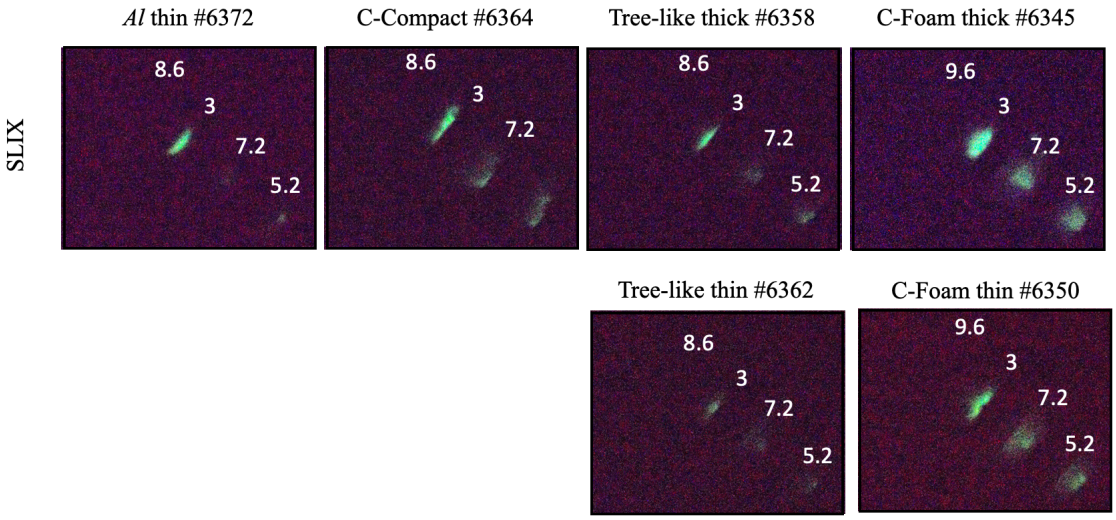

Figure 6.8: SLIX images for the bare Al target, C-Compact (CC), thick Tree-Like (CT), thick C-Foam (CF), thin Tree-Like (CT) and thin C-Foam (CF). The time delays of activation for each SLIX stripes is shown.

Similar considerations can be made in the case of the thick Al substrates. Bare Al, thick Tree-Like and thick CF are compare din Figure 6.9. From the Schlieren at 2 ns, the plasma is more expanded when a foam, either CF or CT is present, with respect to the bare Al case. Additionally, the CF shows a strong and directional emission towards the laser. Considering the shadowgraphs at 4 ns, the red glow appears for the CT, while it is probably covered by the substrate in the case of CF. Again, in the shadowgraphs at 10 ns it is possible to see the developement of a critical/over-critical plasma both in the case of the C-Tree-Like and CF.

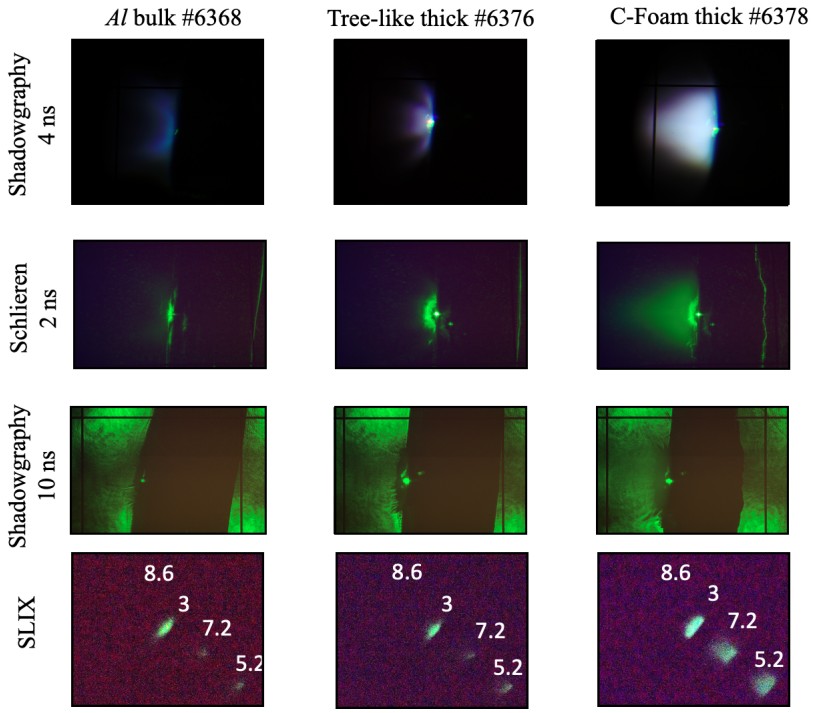

Figure 6.9: In this Figure the shadowgraphs at 4 ns and 10 ns, the schlierens at 2 ns and the SLIX are reported for the three irradiated targets: bare bulk Al which is used as reference, thick Tree-Like (CT) and thick C-Foam (CF). The corresponding shot number is reported for each sample. The time delays of activation for each SLIX stripes is shown.

A shot was also performed on the holder with the thin CH substrate and the thicker CF. The shadowgraphs and SLIX images are reported in Figure 6.10. TPD appears to be reduced with respect to the corresponding sample on the Al thin substrate. Also, X-ray emission from the SLIX appears to be limited in time. These different qualitative results are indications that the Al substrate took part in the interaction in the shots previously examined. This signals the fact that the foams employed in the experiment were transparent to the laser, since it has interacted with the substrate. In the shadowgraph taken at 10 ns there is an evident over-critical plasma puff in front of the target.

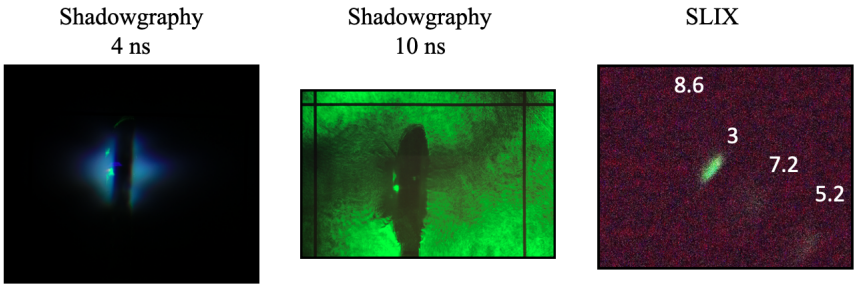

Figure 6.10: In this Figure the shadowgraphs at 4 ns and 10 ns, and the SLIX are reported for the target constituted by the thick C-foam on CH substrate. The time delays of activation for each SLIX stripes is shown.

These qualitative observations are in agreement with the other diagnostics. For example, visible spectroscopy confirmed what has been discussed about TPD. A peak at 3/2 Ω , appears in the spectra of the carbon samples, while it is absent in the case of bare Al. This peak, at 3/2 of the laser frequency, is associated to TPD [105]. Additionally, the intensity of the peak shows a decreasing trend with mass thickness and an increasing trend with density.

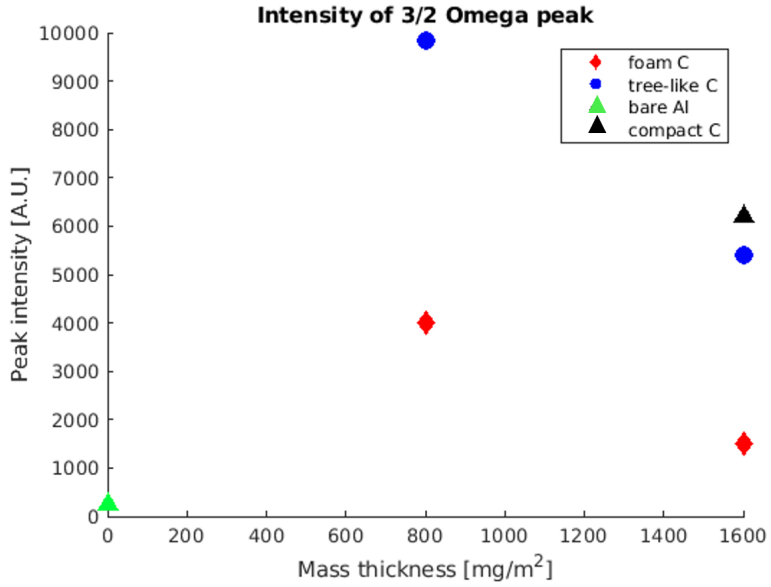

Figure 6.11: The intensity of the 3/2 Ω peaks at different sample mass-thickness is represented. Courtesy of A. Maffini.

6.3. Discussion of the results

The realization of carbon foams targets via ns-PLD and their interaction with a laser in ICF-relevant conditions have been addressed. Concerning the fabrication process, different target configurations and substrates have been tested to assess the compatibility of the PLD technique with the target requirements. These latter depend on the laser parameters and the type of analysis to be performed. For example, if plasma expansion is of interest, thin substrates should be employed. On the other hand, if ablation-loading is under investigation, bulk substrates are required to enable the formation of a crater. Therefore, a 100 μm CH foil, a 1 μm Al foil and a bulk Al disks were employed as substrates. Depositions were performed according to the parameters reported in Chapter 4. As far as the carbon foams are concerned, no particular issues occurred. Foams having a mass-thickness up to 1600 mg/m^2) were successfully deposited on thin Al substrate at both 200 Pa and 50 Pa. The CH substrates were employed only at 200 Pa and they could endure the deposition of the 1600 mg/m^2 CF. Conversely, CC caused damage of the thin substrate and delamination of the film deposited on the thick Al disk. These two different outcomes are probably related to the different kinetic energies of the depositing species. The preliminary qualitative experimental observations give a clear indication that carbon foams play an important role during the interaction with the laser. A different plasma expansion and emission can be observed when comparing foams of different thicknesses and densities. These results highlight the fact that carbon foams could be a promising choice as ablation materials thanks to the versatility of the deposition technique. Several different combination parameters could be tested to obtain the optimal foam characteristics.

7 | Conclusions and future developments

The general goal of the thesis work consisted in the production of engineered targets for laser-plasma interaction experiments exploiting advanced deposition techniques. Targets play a fundamental role in the interaction, since their characteristics determine the coupling with the laser. Therefore, precise control and tunability of target materials properties are of major importance. In general, Physical Vapor Deposition (PVD) techniques are highly versatile methods that can well suit this function. In particular, at the Micro and Nanostructured Materials Laboratory (NanoLab) of Politecnico di Milano, Magnetron Sputtering and Pulsed Laser Deposition (PLD) are exploited in this field. The required target properties depend on the specific interaction under investigation and on the laser parameters. In particular, two main areas framed this thesis work, laser-driven ion sources and Inertial Confinement Fusion (ICF). Therefore, two different classes of laser were considered. In the case of laser-driven ion sources, ultra-high intensity lasers ($I \geq 10^{18}\ W/cm^2$) delivering energies in the order of J in fs pulses are generally employed. High intensity lasers ($I \geq 10^{14}$) delivering energies in the order of tens of J in ns pulses were considered for ICF.

Concerning laser-driven ion sources, the thesis work evolved along two directions. At first, a reliable and versatile procedure to realize large-area free-standing films was developed based on a fishing procedure. Then, the feasibility of realizing a complete Double Layer Target was investigated. Concerning the fishing procedure, a solution of water containing a proper amount of soap is spread over Si or glass slides via spin coating. The metallic film is deposited on the soap-covered substrate via Magnetron Sputtering. Then, water is exploited to dissolve the surfactant layer by gradually dipping the sample. The film floats on water thanks to surface tension, which also helps to keep it flat, reducing the formation of wrinkles. Finally, it is fished with a perforated holder, and free-standing films are obtained in correspondence to each perforation. To assess the effects of the soap layer on film properties, morphological and mechanical characterizations were performed on Al samples deposited on both bare Si substrates and soap-covered ones. The presence

of the soap layer affects film morphology only in some portions of it, with the appearance of fractal-like features. It has also been observed that this effect is reduced for increasing film thickness. Concerning the mechanical properties, films deposited on the sacrificial layer showed the same stress state characterizing the reference samples. Therefore, it can be concluded that films properties are not significantly modified in the presence of a soap layer.

The possibility of tailoring target properties is a relevant aspect for laser-driven ion sources. Exploiting different deposition conditions, films with different characteristics can be obtained. Therefore, the compatibility of the fishing procedure with distinct materials and Magnetron Sputtering regimes has been explored. Cu and Al films have been realized via DCMS, HiPIMS, and, in the case of Al, biased HiPIMS. Moreover, different film thicknesses have been investigated. This parameter influences the maximum achievable ion energies, especially if SL targets are considered. The possibility of spanning the range of obtainable free-standing film thicknesses with high reproducibility is of significant importance. Concerning Double Layer Targets, exploratory carbon foams depositions via PLD have been performed to investigate the mutual compatibility with the fished free-standing films. Additionally, different types of holders have been tested to assess the feasibility of realizing targets of large areas.

In light of the experimental results discussed in Chapter 5, the following conclusions can be drawn. The fishing procedure performs well when ductile materials are employed, like Cu and Al. Nevertheless, the possibility of obtaining free-standing films exploiting a sacrificial layer of soap depends on the interplay between deposited material (i.e., Cu or Al), type of substrate (i.e., Si or glass), and deposition regime (i.e., DCMS, HiPIMS, biased HiPIMS). The bottleneck of the fishing procedure is the assessment of the optimal concentration of soap, which, in principle, must be assessed for each film-substrate pair and deposition condition. Al samples showed good results when deposited on Si substrates via DCMS and HiPIMS, providing flexibility on the deposition conditions. A spin-coating solution containing 30% of soap (by weight of solvent) was necessary. Concerning Cu, it resulted to be a more challenging material. Due to its poor adhesion to Si, glass substrates have to be employed. Promising results were obtained only for Cu deposited via DCMS. In this case, a spin-coating solution containing 6% of soap was exploited. When the proper combination of film material, substrate type, deposition conditions and concentration of soap is chosen, good results can be obtained. Indeed, thicknesses from 50 nm up to 2 μm were realized. Therefore, the fishing procedure enabled to extend the range obtained with the hole-filling technique (see Chapter 2), which was 200 $nm - 1200$ nm. Concerning Double Layer Targets, the fishing procedure seems to guarantee better compatibility between

free-standing films and carbon foams with respect to the hole-filling technique, showing a uniform coverage of the film even at small thicknesses.

The other part of the thesis work was dedicated to the pioneering production of carbon nanofoams targets for experiments in ICF-relevant conditions. Three types of nanostructured carbon films were considered, characterized by different densities and morphologies:

- Carbon foams with a sponge-like morphology (CF), and density of 6 mg/cm^3.
- Carbon foam with a tree-like morphology (CT), and density of 26 mg/cm^3.
- Carbon compact (CC) films with a density close to the bulk value 2000 mg/cm^3.

For each type of carbon film, three mass thicknesses were considered, in the order of 400 mg/m^2, 800 mg/m^2 and 1600 mg/m^2. These large values of mass-thickness, considerably higher than those usually exploited for Double Layer Targets, are relevant in ICF conditions and have never been deposited before at NanoLab. Therefore, the possibility of producing such samples and the mutual compatibility with the substrate had to be investigated. Carbon foam depositions were performed directly on target holders or substrates, exploitable in certain experimental configurations. The employed holders/substrates were thin (100 nm thick) plastic (CH) free-standing films, thin (1 μm) Al free-standing films, and bulk Al disks. Exceptionally, the thin CH foils could endure all CF depositions, even the one with the highest mass-thickness of 1600 mg/m^2. Moreover, substrates resulted covered with good uniformity. The same holds true for both thin Al films and bulk Al disks substrates. Equivalent considerations can be made for the CT samples on Al thin films and bulk disks. The realization of CC samples gave rise to some issues. The CH foils could not resist the deposition, neither that of the thinner CC. Concerning Al foils, some of them resulted wrinkled. Additionally, some of the samples deposited on the Al bulk were delaminated. This behavior can be ascribed to the presence of intrinsic stresses in the compact carbon film. Therefore, it has been demonstrated the feasibility of depositing carbon foams characterized by incredibly high mass-thicknesses and tunable properties on different and even delicate substrates. Carbon compact films depositions are of more concern.

The produced targets were also exploited in an experimental campaign carried out at the ABC laser facility (Frascati). The aim was an explorative investigation of the interaction of carbon nanofoams with a laser beam in ICF-relevant conditions, which are very different from those typical of ion acceleration experiments (10^{14} W/cm^2 vs 10^{18} W/cm^2, ns vs fs pulses, respectively). The preliminary experimental observation highlighted the transparency of the produced samples to the laser wavelength of 1054 nm. Despite that,

substantial differences in the outputs of the several employed diagnostics could be noted when comparing different C-foam samples. Therefore, a first promising conclusion can be drawn: the foam micro/nanostrucutre has an effect on the interaction with the laser.

Owing to the promising results obtained, it might be interesting to carry on the work done during this thesis work. Concerning targets for laser-driven ion sources, possible future perspectives are:

- Perform both experimental and simulation campaigns to investigate the behavior of the realized SL and DLTs, also aiming at improving their properties.
- Assess the versatility of the fishing procedure by further enlarging the obtainable thickness range and test other materials, either ductile like tin (Sn) and more fragile like titanium (Ti).
- Further investigation of foam deposition to get more insights on the mutual compatibility between free-standing films and foams.
- Find a semi-empirical correlation between the film/substrate adhesion strength and the required amount of soap for the spin-coating solution.
- Proceed with the data analysis of the ABC experimental campaign and perform modeling activities to assess improved parameters
- Verify the possibility of producing carbon foam targets for ICF with greater thicknesses or optimized parameters, also in light of the experimental and future theoretical results.

Bibliography

[1] Orazio Svelto. *Principles of Lasers*. Springer Science+Business Media, New York, 1998.

[2] Davide Orecchia. Femtosecond pulsed laser deposition of carbon nanofoams for laser-driven ion acceleration. Master's thesis, Politecnico di Milano, 2019.

[3] R. Linggamm, M. M. Quazi, M. Nasir Bashir, M. H. Aiman, Abdullah Qaban, Foram Dave, and M. M. Ali. A review on the formation of colors on ss304 stainless steel induced by laser color marking technique. *Journal of Advances in Technology and Engineering Research*, 7(2):01–26, 2021.

[4] M. Zavelani-Rossi and F. Vismarra. *High Intensity Lasers for Nuclear and Physical Applications*. Esculapio, 2021.

[5] G. Strickland, S.and Mourou. Compression of amplified chirped optical pulses. *Optics Communications*, 56(3):219–221, 1985.

[6] I. V. Yakovlev. Stretchers and compressors for ultra-high power laser systems. *Quantum Electronics*, 44(4):393, 2014.

[7] Paul Gibbon. *Short Pulse Laser Interactions with Matter*. Imperial College Press, September 2005.

[8] William L. Kruer. *The Physics of Laser Plasma Interactions*. Addison-Wesley Publishing Co., Reading, MA (US), 1988.

[9] Jeffrey P. Freidberg. *Plasma Physics and Fusion Energy*. Cambridge University Press, 2007.

[10] Gianluca Pucella and Sergio Segre. *Fisica dei plasmi*. Zanichelli, 2014.

[11] Donald Umstadter. Relativistic laser–plasma interactions. *Journal of Physics D: Applied Physics*, 36(8):R151, apr 2003.

[12] A. I. Akhiezer and R. V. Polovin. Theory of wave motion of an electron plasma. *Soviet Physics JETP*, Vol 3, 1956.

[13] Stefano Atzeni and Jürgen Meyer-ter Vehn. *The Physics of Inertial Fusion: Beam-Plasma Interaction, Hydrodynamics, Hot Dense Matter*. Clarendon Press-Oxford, 2004.

[14] M. Lafon, R. Betti, K. S. Anderson, T. J. B. Collins, R. Epstein, P. W. McKenty, J. F. Myatt, A. Shvydky, and S. Skupsky. Direct-drive-ignition designs with mid-z ablators. *Physics of Plasmas*, 22(3):032703, 2015.

[15] Andrea Macchi, Marco Borghesi, and Matteo Passoni. Ion acceleration by superintense laser-plasma interaction. *Rev. Mod. Phys.*, 85:751–793, May 2013.

[16] T. Tajima and J. M. Dawson. Laser electron accelerator. *Phys. Rev. Lett.*, 43:267–270, Jul 1979.

[17] E. Esarey, C. B. Schroeder, and W. P. Leemans. Physics of laser-driven plasma-based electron accelerators. *Rev. Mod. Phys.*, 81:1229–1285, Aug 2009.

[18] M Passoni, F M Arioli, L Cialfi, D Dellasega, L Fedeli, A Formenti, A C Giovannelli, A Maffini, F Mirani, A Pazzaglia, A Tentori, D Vavassori, M Zavelani-Rossi, and V Russo. Advanced laser-driven ion sources and their applications in materials and nuclear science. *Plasma Physics and Controlled Fusion*, 62(1):014022, dec 2019.

[19] E. Lefebvre, N. Cochet, S. Fritzler, V. Malka, M.-M. Aléonard, J.-F. Chemin, S. Darbon, L. Disdier, J. Faure, A. Fedotoff, O. Landoas, G. Malka, V. Méot, P. Morel, M. Rabec Le Gloahec, A. Rouyer, Ch. Rubbelynck, V. Tikhonchuk, R. Wrobel, P. Audebert, and C. Rousseaux. Electron and photon production from relativistic laser–plasma interactions. *Nuclear Fusion*, 43(7):629, jul 2003.

[20] Christopher P. Jones, Ceri M. Brenner, Camilla A. Stitt, Chris Armstrong, Dean R. Rusby, Seyed R. Mirfayzi, Lucy A. Wilson, Aarón Alejo, Hamad Ahmed, Ric Allott, Nicholas M.H. Butler, Robert J. Clarke, David Haddock, Cristina Hernandez-Gomez, Adam Higginson, Christopher Murphy, Margaret Notley, Charilaos Paraskevoulakos, John Jowsey, Paul McKenna, David Neely, Satya Kar, and Thomas B. Scott. Evaluating laser-driven bremsstrahlung radiation sources for imaging and analysis of nuclear waste packages. *Journal of Hazardous Materials*, 318:694–701, 2016.

[21] A Formenti, M Galbiati, and M Passoni. Modeling and simulations of ultra-intense laser-driven bremsstrahlung with double-layer targets. *Plasma Physics and Controlled Fusion*, 64(4):044009, feb 2022.

[22] Irene Prencipe, Josefine Metzkes-Ng, Andrea Pazzaglia, Constantin Bernert, David

Dellasega, Luca Fedeli, Arianna Formenti, Marco Garten, Thomas Kluge, Stephan Kraft, Alejandro Laso Garcia, Alessandro Maffini, Lieselotte Obst-Huebl, Martin Rehwald, Manfred Sobiella, Karl Zeil, Ulrich Schramm, Thomas E. Cowan, and Matteo Passoni. Efficient laser-driven proton and bremsstrahlung generation from cluster-assembled foam targets. *New Journal of Physics*, 23(9), sep 2021.

[23] Hiroyuki Daido, Mamiko Nishiuchi, and Alexander S Pirozhkov. Review of laser-driven ion sources and their applications. *Reports on Progress in Physics*, 75(5):056401, apr 2012.

[24] Luís O. Silva, Michael Marti, Jonathan R. Davies, Ricardo A. Fonseca, Chuang Ren, Frank S. Tsung, and Warren B. Mori. Proton shock acceleration in laser-plasma interactions. *Phys. Rev. Lett.*, 92:015002, Jan 2004.

[25] Francesco Mirani. Ion beam analysis with laser-driven proton beams. Master's thesis, Politecnico di Milano, 2017.

[26] Andrea Maffini, Francesco Mirani, Marta Galbiati, et al. Towards compact laser-driven accelerators: exploring the potential of advanced double-layer targets. *EPJ Techn Instrum*, 10(15):1–15, 2023.

[27] U. Linz and J. Alonso. Phys. rev. st accel. beams. 10(9):094801, 2007.

[28] F. Mirani, A. Maffini, and M. Passoni. Laser-driven neutron generation with near-critical targets and application to materials characterization. *Phys. Rev. Appl.*, 19:044020, Apr 2023.

[29] Francesco Mirani, Daniele Calzolari, Andrea Formenti, et al. Superintense laser-driven photon activation analysis. *Commun Phys*, 4(185):1–11, 2021.

[30] Jef Ongena and Yuichi Ogawa. Nuclear fusion: Status report and future prospects. *Energy Policy*, 96:770–778, 2016.

[31] R. S. Craxton, K. S. Anderson, T. R. Boehly, V. N. Goncharov, D. R. Harding, J. P. Knauer, R. L. McCrory, P. W. McKenty, D. D. Meyerhofer, J. F. Myatt, A. J. Schmitt, J. D. Sethian, R. W. Short, S. Skupsky, W. Theobald, W. L. Kruer, K. Tanaka, R. Betti, T. J. B. Collins, J. A. Delettrez, S. X. Hu, J. A. Marozas, A. V. Maximov, D. T. Michel, P. B. Radha, S. P. Regan, T. C. Sangster, W. Seka, A. A. Solodov, J. M. Soures, C. Stoeckl, and J. D. Zuegel. Direct-drive inertial confinement fusion: A review. *Physics of Plasmas*, 22(11):110501, 2015.

[32] M Passoni, A Zani, A Sgattoni, D Dellasega, A Macchi, I Prencipe, V Floquet, P Martin, T V Liseykina, and T Ceccotti. Energetic ions at moderate laser intensi-

ties using foam-based multi-layered targets. *Plasma Physics and Controlled Fusion*, 56(4):045001, mar 2014.

[33] A. J. Mackinnon, Y. Sentoku, P. K. Patel, D. W. Price, S. Hatchett, M. H. Key, C. Andersen, R. Snavely, and R. R. Freeman. Enhancement of proton acceleration by hot-electron recirculation in thin foils irradiated by ultraintense laser pulses. *Physical Review Letters*, 88(21):215006, 2002.

[34] M. Cerchez, M. Swantusch, M. Toncian, X. M. Zhu, R. Prasad, T. Toncian, Ch. Rödel, O. Jäckel, G. G. Paulus, A. A. Andreev, and O. Willi. Enhanced energy absorption of high intensity laser pulses by targets of modulated surface. *Applied Physics Letters*, 112(22), 05 2018. 221103.

[35] T. Ceccotti, V. Floquet, A. Sgattoni, A. Bigongiari, O. Klimo, M. Raynaud, C. Riconda, A. Heron, F. Baffigi, L. Labate, L. A. Gizzi, L. Vassura, J. Fuchs, M. Passoni, M. Kve ton, F. Novotny, M. Possolt, J. Proku pek, J. Pros ka, J. Ps ikal, L. S tolcova, A. Velyhan, M. Bougeard, P. D'Oliveira, O. Tcherbakoff, F. Re au, P. Martin, and A. Macchi. Evidence of resonant surface-wave excitation in the relativistic regime through measurements of proton acceleration from grating targets. *Physical Review Letters*, 111(18):185001, 2013.

[36] K. Zeil, J. Metzkes, T. Kluge, M. Bussmann, T.E. Cowan, S.D. Kraft, R. Sauerbrey, B. Schmidt, M. Zier, and U. Schramm. Robust energy enhancement of ultrashort pulse laser accelerated protons from reduced mass targets. *Plasma Physics and Controlled Fusion*, 56(8):084004, 2014.

[37] D. Margarone, O. Klimo, I. J. Kim, J. Prokůpek, J. Limpouch, T. M. Jeong, T. Mocek, J. Pšikal, H. T. Kim, J. Proška, K. H Nam, L. Štolcová, I. W. Choi, S. K. Lee, J. H. Sung, T. J. Yu, and G. Korn. Laser-driven proton acceleration enhancement by nanostructured foils. *Phys. Rev. Lett.*, 109:234801, Dec 2012.

[38] J. H. Bin, W. J. Ma, H. Y. Wang, M. J. V. Streeter, C. Kreuzer, D. Kiefer, M. Yeung, S. Cousens, P. S. Foster, B. Dromey, X. Q. Yan, R. Ramis, J. Meyer-ter Vehn, M. Zepf, and J. Schreiber. Ion acceleration using relativistic pulse shaping in near-critical-density plasmas. *Phys. Rev. Lett.*, 115:064801, Aug 2015.

[39] M. Passoni, A. Sgattoni, I. Prencipe, L. Fedeli, D. Dellasega, L. Cialfi, Il Woo Choi, I Jong Kim, K. A. Janulewicz, Hwang Woon Lee, Jae Hee Sung, Seong Ku Lee, and Chang Hee Nam. Toward high-energy laser-driven ion beams: Nanostructured double-layer targets. *Phys. Rev. Accel. Beams*, 19:061301, Jun 2016.

[40] I Prencipe, A Sgattoni, D Dellasega, L Fedeli, L Cialfi, Il Woo Choi, I Jong

Kim, K A Janulewicz, K F Kakolee, Hwang Woon Lee, Jae Hee Sung, Seong Ku Lee, Chang Hee Nam, and M Passoni. Development of foam-based layered targets for laser-driven ion beam production. *Plasma Physics and Controlled Fusion*, 58(3):034019, feb 2016.

[41] A. Zani, D. Dellasega, V. Russo, and M. Passoni. Ultra-low density carbon foams produced by pulsed laser deposition. *Carbon*, 56:358–365, 2013.

[42] A. Maffini, A. Pazzaglia, D. Dellasega, V. Russo, and M. Passoni. Growth dynamics of pulsed laser deposited nanofoams. *Phys. Rev. Mater.*, 3:083404, Aug 2019.

[43] A. Maffini, D. Orecchia, A. Pazzaglia, M. Zavelani-Rossi, and M. Passoni. Pulsed laser deposition of carbon nanofoam. *Applied Surface Science*, 599:153859, 2022.

[44] M Passoni, A Zani, A Sgattoni, D Dellasega, A Macchi, I Prencipe, V Floquet, P Martin, T V Liseykina, and T Ceccotti. Energetic ions at moderate laser intensities using foam-based multi-layered targets. *Plasma Physics and Controlled Fusion*, 56(4):045001, mar 2014.

[45] Luca Fedeli, Arianna Formenti, Lorenzo Cialfi, Andrea Pazzaglia, and Matteo Passoni. Ultra-intense laser interaction with nanostructured near-critical plasmas. *Scientific Reports*, 8(1):3834, 03 2018.

[46] Andrea Pazzaglia, Luca Fedeli, Arianna Formenti, Alessandro Maffini, and Matteo Passoni. A theoretical model of laser-driven ion acceleration from near-critical double-layer targets. *Communications Physics*, 3(1):133, 08 2020.

[47] R. Betti and O. Hurricane. Inertial-confinement fusion with lasers. *Nature Phys*, 12:435–448, 2016.

[48] R. K. Follett, J. A. Delettrez, D. H. Edgell, V. N. Goncharov, R. J. Henchen, J. Katz, D. T. Michel, J. F. Myatt, J. Shaw, A. A. Solodov, C. Stoeckl, B. Yaakobi, and D. H. Froula. Two-plasmon decay mitigation in direct-drive inertial-confinement-fusion experiments using multilayer targets. *Physical Review Letters*, 116(15):155002, 2016.

[49] R. De Angelis, F. Consoli, S. Yu. Gus'kov, A. A. Rupasov, P. Andreoli, G. Cristofari, and G. Di Giorgio. Laser-ablated loading of solid target through foams of overcritical density. *Physics of Plasmas*, 22(7):072701, 2015.

[50] M. Cipriani, S. Yu. Gus'kov, R. De Angelis, F. Consoli, A. A. Rupasov, P. Andreoli, G. Cristofari, and G. Di Giorgio. Laser-driven hydrothermal wave speed in low-z foam of overcritical density. *Physics of Plasmas*, 25(9):092704, 2018.

[51] M. Cipriani, S. Yu. Gus'kov, F. Consoli, R. De Angelis, A. A. Rupasov, P. Andreoli, G. Cristofari, G. Di Giorgio, and M. Salvadori. Time-dependent measurement of high-power laser light reflection by low-z foam plasma. *High Power Laser Science and Engineering*, 9:e40, 2021.

[52] Martina Salvadori, Pier Luigi Andreoli, Mattia Cipriani, Fabrizio Consoli, Giuseppe Cristofari, Riccardo De Angelis, Giorgio di Giorgio, Danilo Giulietti, Francesco Ingenito, Sergey Yu. Gus'kov, and Alexander A. Rupasov. Laser irradiated foam targets: Absorption and radiative properties. *EPJ Web of Conferences*, 167:05003, 2018. PPLA 2017.

[53] V. Tikhonchuk, Y. J. Gu, O. Klimo, J. Limpouch, and S. Weber. Studies of laser-plasma interaction physics with low-density targets for direct-drive inertial confinement schemes. *Matter and Radiation at Extremes*, 4(4):045402, 2019.

[54] Ph. Nicolaï, M. Olazabal-Loumé, S. Fujioka, A. Sunahara, N. Borisenko, S. Gus'kov, A. Orekov, M. Grech, G. Riazuelo, C. Labaune, J. Velechowski, and V. Tikhonchuk. Experimental evidence of foam homogenization. *Physics of Plasmas*, 19(11):113105, 2012.

[55] A. A. Solodov, M. J. Rosenberg, W. Seka, J. F. Myatt, M. Hohenberger, R. Epstein, C. Stoeckl, R. W. Short, S. P. Regan, P. Michel, T. Chapman, R. K. Follett, J. P. Palastro, D. H. Froula, P. B. Radha, J. D. Moody, and V. N. Goncharov. Hot-electron generation at direct-drive ignition-relevant plasma conditions at the national ignition facility. *Physics of Plasmas*, 27(5):052706, 2020.

[56] A. B. Zylstra, O. A. Hurricane, D. A. Callahan, and et al. Burning plasma achieved in inertial fusion. *Nature*, 601:542–548, 2022.

[57] Shinsuke Fujioka, Atsushi Sunahara, Naofumi Ohnishi, and et al. Suppression of rayleigh–taylor instability due to radiative ablation in brominated plastic targets. *Physics of Plasmas*, 11(6):2814–2822, 2004.

[58] S. X. Hu, G. Fiksel, V. N. Goncharov, S. Skupsky, D. D. Meyerhofer, and V. A. Smalyuk. Mitigating laser imprint in direct-drive inertial confinement fusion implosions with high-z dopants. *Phys. Rev. Lett.*, 108:195003, May 2012.

[59] S. X. Hu, R. Epstein, W. Theobald, H. Xu, H. Huang, V. N. Goncharov, S. P. Regan, P. W. McKenty, R. Betti, E. M. Campbell, and D. S. Montgomery. Direct-drive double-shell implosion: A platform for burning-plasma physics studies. *Physical Review E*, 100(6):063204, 2019.

[60] John L. Kline, Sunghwan Yi, Andrei Nikolaevich Simakov, Douglas Carl Wilson, George Amine Kyrala, Steven H. Batha, Theodore Sonne Perry, Alex Zylstra, Richard Edward Olson, E. L. Dewald, R. Tommasini, J. E. Ralph, D. J. Strozzi, M. B. Schneider, A. G. MacPhee, D. A. Callahan, D. E. Hinkel, O. A. Hurricane, J. L. Milovich, J. R. Rygg, S. Khan, and et al. First beryllium capsule implosions on the national ignition facility. *Physics of Plasmas*, 2015.

[61] Sergey Yu. Gus'kov. Nonequilibrium laser-produced plasma of volume-structured media and inertial-confinement-fusion applications. *Journal of Russian Laser Research*, 31(6), 2010.

[62] R. Dezulian, F. Canova, S. Barbanotti, F. Orsenigo, R. Redaelli, T. Vinci, G. Lucchini, D. Batani, B. Rus, J. Polan, M. Kozlová, M. Stupka, A. R. Praeg, P. Homer, T. Havlicek, M. Soukup, E. Krousky, J. Skala, R. Dudzak, M. Pfeifer, H. Nishimura, K. Nagai, F. Ito, T. Norimatsu, A. Kilpio, E. Shashkov, I. Stuchebrukhov, V. Vovchenko, V. Chernomyrdin, and I. Krasuyk. Hugoniot data of plastic foams obtained from laser-driven shocks. *Phys. Rev. E*, 73:047401, Apr 2006.

[63] Davide Vavassori. Production of optimized targets for enhanced laser-driven ion acceleration. Master's thesis, Politecnico di Milano, 2019.

[64] Francesco Gatti. Development of non-conventional targets for laser-driven particle sources. Master's thesis, Politecnico di Milano, 2021.

[65] F. Mirani et al. Experimental demonstration of laser-driven differential particle induced x-ray emission and proton activation analysis. In *ELIMAIA satellite meeting – Application workshop "Multidisciplinary Applications of Laser-driven Ions"*, Prague, Czech Republic, November 2022.

[66] Yu Miyamoto, Yuma Fujii, Masafumi Yamano, Toru Harigai, Yoshiyuki Suda, Hirofumi Takikawa, Takeshi Kawano, Mamiko Nishiuchi, Hironao Sakaki, and Kiminori Kondo. Preparation of self-supporting au thin films on perforated substrate by releasing from water-soluble sacrificial layer. *Japanese Journal of Applied Physics*, 55(7S2):07LE05, jun 2016.

[67] A. Maffini et al. Pulsed laser deposition of nanofoam targets for laser-driven inertial fusion experiments. In *36th European Conference on Laser Interaction with Matter (ECLIM)*, Frascati, Italy, September 2022. ENEA Centro Ricerche Frascati.

[68] V. Ciardiello. Theoretical study of high-power laser interaction with novel nanostructured foam materials for inertial confinement fusion research. Master's thesis, Politecnico di Milano, 2022.

[69] Daniel Lundin, Tiberiu Minea, and Jon Tomas Gudmundsson, editors. *High Power Impulse Magnetron Sputtering: Fundamentals, Technologies, Challenges and Applications*. Elsevier, 2020.

[70] J T Gudmundsson. Physics and technology of magnetron sputtering discharges. *Plasma Sources Science and Technology*, 29(11):113001, nov 2020.

[71] Irving P. Herman. Chapter 6 - optical emission spectroscopy. In Irving P. Herman, editor, *Optical Diagnostics for Thin Film Processing*, pages 157–213. Academic Press, San Diego, 1996.

[72] K. Sarakinos, J. Alami, and S. Konstantinidis. High power pulsed magnetron sputtering: A review on scientific and engineering state of the art. *Surface and Coatings Technology*, 204(11):1661–1684, 2010.

[73] D. Dellasega, F. Mirani, D. Vavassori, C. Conti, and M. Passoni. Role of energetic ions in the growth of fcc and ω crystalline phases in ti films deposited by hipims. *Applied Surface Science*, 556:149678, 2021.

[74] Mattias Samuelsson, Daniel Lundin, Jens Jensen, Michael A. Raadu, Jon Tomas Gudmundsson, and Ulf Helmersson. On the film density using high power impulse magnetron sputtering. *Surface and Coatings Technology*, 205(2):591–596, 2010.

[75] Baohua Wu, Ian Haehnlein, Ivan Shchelkanov, Jake McLain, Dhruval Patel, Jan Uhlig, Brian Jurczyk, Yongxiang Leng, and David N. Ruzic. Cu films prepared by bipolar pulsed high power impulse magnetron sputtering. *Vacuum*, 150:216–221, 2018.

[76] Rommel Paulo B. Viloan, Ulf Helmersson, and Daniel Lundin. Copper thin films deposited using different ion acceleration strategies in hipims. *Surface and Coatings Technology*, 422:127487, 2021.

[77] Jerrold A. Floro, Eric Chason, Robert C. Cammarata, and David J. Srolovitz. Physical origins of intrinsic stresses in volmer–weber thin films. *MRS Bulletin*, 27(1):19–25, 2002.

[78] P. B. Barna and M. Adamik. Fundamental structure forming phenomena of polycrystalline films and the structure zone models. *Thin Solid Films*, 317(1):27–33, 1998.

[79] Eric Chason and Pradeep R. Guduru. Tutorial: Understanding residual stress in polycrystalline thin films through real-time measurements and physical models. *Journal of Applied Physics*, 119(19):191101, 2016.

[80] André Anders. A structure zone diagram including plasma-based deposition and ion etching. *Thin Solid Films*, 518(15):4087–4090, 2010.

[81] Grégory Abadias, Eric Chason, Jozef Keckes, Marco Sebastiani, Gregory B. Thompson, Etienne Barthel, Gary L. Doll, Conal E. Murray, Chris H. Stoessel, and Ludvik Martinu. Review article: Stress in thin films and coatings: Current status, challenges, and prospects. *Journal of Vacuum Science & Technology A*, 36(2):020801, 2018.

[82] Angela De Bonis and Roberto Teghil. Ultra-short pulsed laser deposition of oxides, borides and carbides of transition elements. *Coatings*, 10(5), 2020.

[83] Michael NR Ashfold, Frederik Claeyssens, Gareth M Fuge, and Simon J Henley. Pulsed laser ablation and deposition of thin films. *Chemical Society Reviews*, 33(1):23–31, 2004.

[84] Baerbel Rethfeld, Dmitriy S Ivanov, Martin E Garcia, and Sergei I Anisimov. Modelling ultrafast laser ablation. *Journal of Physics D: Applied Physics*, 50(19):193001, apr 2017.

[85] Irene Prencipe, David Dellasega, Alessandro Zani, Daniele Rizzo, and Matteo Passoni. Energy dispersive x-ray spectroscopy for nanostructured thin film density evaluation. *Science and Technology of Advanced Materials*, 16(2):025007, 2015. PMID: 27877776.

[86] George Gerald Stoney. The tension of metallic films deposited by electrolysis. *Proceedings of the Royal Society of London. Series A, Containing Papers of a Mathematical and Physical Character*, 82(553):172–175, 1909.

[87] E. Besozzi, D. Dellasega, A. Pezzoli, A. Mantegazza, M. Passoni, and M.G. Beghi. Coefficient of thermal expansion of nanostructured tungsten based coatings assessed by substrate curvature method. *Materials & Design*, 137:192–203, 2018.

[88] André Anders, Joakim Andersson, and Arutiun Ehiasarian. High power impulse magnetron sputtering: Current-voltage-time characteristics indicate the onset of sustained self-sputtering. *Journal of Applied Physics*, 102(11), 12 2007. 113303.

[89] D V Sidelev, A V Yuryeva, V P Krivobokov, A S Shabunin, M S Syrtanov, and Z Koishybayeva. Aluminum films deposition by magnetron sputtering systems: Influence of target state and pulsing unit. *Journal of Physics: Conference Series*, 741(1):012193, aug 2016.

[90] National Institute of Standards and Technology. NIST Atomic Spectra Database. `https://physics.nist.gov/PhysRefData/ASD/lines_form.html`.

[91] J. Liu, B. Xu, H. Wang, X. Cui, L. Zhu, and G. Jin. Effects of film thickness and microstructures on residual stress. *Surface Engineering*, 32(3):178–184, 2016.

[92] A. A. Solovyev, V. O. Oskirko, V. A. Semenov, et al. Comparative study of cu films prepared by dc, high-power pulsed and burst magnetron sputtering. *Journal of Electronic Materials*, 45(9):4052–4060, 2016.

[93] N Brenning, J T Gudmundsson, M A Raadu, T J Petty, T Minea, and D Lundin. A unified treatment of self-sputtering, process gas recycling, and runaway for high power impulse sputtering magnetrons. *Plasma Sources Science and Technology*, 26(12):125003, nov 2017.

[94] Soo-Jung Hwang, Je-Hun Lee, Chang-Oh Jeong, and Young-Chang Joo. Effect of film thickness and annealing temperature on hillock distributions in pure al films. *Scripta Materialia*, 56(1):17–20, 2007.

[95] I. Petrov, P. B. Barna, L. Hultman, and J. E. Greene. Microstructural evolution during film growth. *Journal of Vacuum Science and Technology A*, 21(5):S117–S128, 09 2003.

[96] N Z Liu and Y Liu. Suppressing hillock formation in si-supported pure al films. *Materials Research Express*, 5(4):046403, apr 2018.

[97] Yi Xu, Guodong Li, Guang Li, Fangyuan Gao, and Yuan Xia. Effect of bias voltage on the growth of super-hard (alcrtivzr)n high-entropy alloy nitride films synthesized by high power impulse magnetron sputtering. *Applied Surface Science*, 564:150417, 2021.

[98] Wenjun Ma, V.Kh. Liechtenstein, J. Szerypo, D. Jung, P. Hilz, B.M. Hegelich, H.J. Maier, J. Schreiber, and D. Habs. Preparation of self-supporting diamond-like carbon nanofoils with thickness less than 5nm for laser-driven ion acceleration. *Nuclear Instruments and Methods in Physics Research Section A: Accelerators, Spectrometers, Detectors and Associated Equipment*, 655(1):53–56, 2011. Proceedings of the 25th World Conference of the International Nuclear Target Development Society.

[99] Birgit Kindler, Willi Hartmann, Annett Hübner, Bettina Lommel, and Jutta Steiner. Development of carbon foils with a thickness of up to $600 \mu g/cm^2$. *Nuclear Instruments and Methods in Physics Research Section A: Accelerators, Spec-*

trometers, Detectors and Associated Equipment, 613(3):425–428, 2010. Target and Stripper Foil Technologies for High Intensity Beams.

[100] B Lommel, W Hartmann, B Kindler, J Klemm, and J Steiner. Preparation of self-supporting carbon thin films. *Nuclear Instruments and Methods in Physics Research Section A: Accelerators, Spectrometers, Detectors and Associated Equipment*, 480(1):199–203, 2002. Targets for Particle Beams: Preparation and Use. Proceedings of t he 20th World Conference of the International Nuclear Target Development Society.

[101] Amit Banerjee and S S Banerjee. Growing gold fractal nano-structures and studying changes in their morphology as a function of film growth rate. *Materials Research Express*, 3(10):105016, oct 2016.

[102] ENEA-Frascati. Confinamento inerziale.

[103] Gary S Settles and Michael J Hargather. A review of recent developments in schlieren and shadowgraph techniques. *Measurement Science and Technology*, 28(4):042001, feb 2017.

[104] D. Batani, J. Santos, P. Forestier-Colleoni, D. Mancelli, M. Ehret, J. Trela, A. Morace, K. Jakubowska, L. Antonelli, D. del Sorbo, M. Manclossi, and M. Veltcheva. Optical time-resolved diagnostics of laser-produced plasmas. *Journal of Fusion Energy*, 38(3):299–314, August 2019.

[105] D. A. Russell and D. F. DuBois. $\frac{3}{2}\omega_0$ radiation from the laser-driven two-plasmon decay instability in an inhomogeneous plasma. *Phys. Rev. Lett.*, 86:428–431, Jan 2001.

List of Figures

List of Tables

List of Symbols

Variable	Description	SI System	CGS System
e	Fundamental Charge	$1.602176634\times10^{-19}$ C	4.8032047×10^{-10} sC
m_e	Electron Mass	$9.1093837015\times10^{-31}$ kg	$9.1093837015\times10^{-28}$ g
c	Light Velocity	2.99792458×10^{8} m/s	2.99792458×10^{10} cm/s